ELECTRICAL AND OPTICAL PROPERTIES OF NANOSTRUCTURED METAL-EMBEDDED ZnO FILMS FOR TRANSPARENT CONDUCTORS

by

Po-Shun Huang

B.S. in Chemical Engineering, Chung Yuan Christian University., Taiwan, 2004

M.S. in Chemical Engineering, National Taiwan University of Science and Technology, Taiwan, 2006

Submitted to the Graduate Faculty of

Swanson School of Engineering in partial fulfillment

of the requirements for the degree of

Doctor of Philosophy

University of Pittsburgh

2015

UNIVERSITY OF PITTSBURGH

SWANSON SCHOOL OF ENGINEERING

This dissertation was presented

by

Po-Shun Huang

It was defended on

July 10th, 2015

and approved by

Jung-Kun Lee, PhD, Associate Professor, Department of Mechanical Engineering and Materials Science

Paul W. Leu, PhD, Assistant Professor, Department of Industry Engineering

John A. Barnard, PhD, Professor, Department of Mechanical Engineering and Materials Science

Qing-Ming Wang, PhD, Professor, Department of Mechanical Engineering and Materials Science

Ian Nettleship, PhD, Associate Professor, Department of Mechanical Engineering and Materials Science

Dissertation Director: Jung-Kun Lee, PhD, Associate Professor,

Department of Mechanical Engineering and Materials Science

ELECTRICAL AND OPTICAL PROPERTIES OF NANOSTRUCTURED METAL-EMBEDDED ZnO FILMS FOR TRANSPARENT CONDUCTORS

Po-Shun Huang, PhD

University of Pittsburgh, 2015

The ability to enhance the carrier concentration without compromising the electron mobility is desired for ZnO-based transparent conducing oxide (TCO) materials, since the impurity doping for high carrier concentration increases the carrier scattering centers. Therefore, we demonstrated that ZnO-based films embedded with nanostructured metals can offer TCO composite films to possess a high carrier concentration without severely damaging the carrier mobility. Those unique properties of these nanocomposite films are attributed to the electron donation from nanostructured metal. Temperature-dependent Hall effect measurements reveal that electrons donated from metal nanoparticles could overcome the low Schottky barrier (or ohmic contact) at metal-ZnO interface and further transport in the ZnO matrix. Once electrons are transferred to the ZnO matrix, they can travel with less impurity-scattering. In addition, ZnO films embedded with a mixture of nanoparticles and nanowires have improved conductivity and optical transmission since electrons provided from nanoparticles or nanowires can transport in percolated conducting paths as long as the critical volume ratio of the metal constituent is achieved.

Furthermore, ZnO films embedded with earth-abundant Cu-Ni core-shell NPs exhibited conductivity which is increased by up to two-orders of magnitude than that of unintentionally doped ZnO film. These Cu-Ni core-shell NPs showed much more thermal stability than

monometallic Cu NPs. It was reported that the conductivity of ZnO: Cu NP composite films degraded at 300 ^{o}C. In contrast, ZnO: Cu-Ni NP films maintained a good conductivity caused by the Cu-Ni core-shell NPs even after the heat treatment. This is due to the fact that the surface of Ni shell was oxidized preferentially and formed a uniform NiO_X thin layer passivating Cu cores. In the future, we expect to fabricate ZnO embedded Cu-Ni nanoparticles and nanowires annealed at a low temperature with a controlled volume ratio. Our goal is not only to improve the conductivity and transparency of such composite films but also provide an affordable choice of electrode materials for the application of solar cells.

TABLE OF CONTENTS

LIST OF TABLES

LIST OF FIGURES

PREFACE

During this PhD career in the University of Pittsburgh, I have been assisted by several people. I would like to announce my acknowledgement to those who have ever helped me go through this life-changing point of my career. First of all, I have to appreciate my advisor, Prof. Jung-Kun Lee for his wise guidance during my PhD study. His creative thinking and passion on the research has enlightened me significantly. Without his mentoring, I could not have aimed my focus on the correct direction, and therefore could have not finished each milestone of my PhD career in the allotted period of time. In addition, I also appreciate my other committee members, Prof. Paul W. Leu, Prof. John A. Barnard, Prof. Ian Nettleship, and Prof. Qing-Ming Wang. Their brilliant advice has broadened my horizons in the research, and their in-depth comments have made my PhD dissertation more flawless in the viewpoint of science.

I am glad that I worked with several great members in our group: Mengjin Yang, Bo Ding, Youngsoo Jung, Salim Caliskan, Ziye Xiong, Fan Qing, Fangda Yu, and Matthew Duff. They are very intelligent and industrious researchers. Mengjin and Bo Ding were in this research lab a few years earlier than me. They became my role models in terms of being a successful PhD researcher. Then, Youngsoo Jung, who joined the research lab with me in 2010, studied several classes in materials science together, and discussed the knowledge and some useful tips that lead to a successful research. Those are the moments that I could not possibly forgot. Salim Caliskan, Ziye

Xiong, Fan Qing, Fangda Yu, and Matthew Duff were my good juniors who provided enormous support to my PhD research.

Moreover, I need to announce my gratitude to my good friends in Pittsburgh: Jian Feng, Tong Chung Gao, Matthew Barry, Ziwei Yi, Cong Lu, Xiaozhou Fu, Chengyuan Zhou, You-Cyuan Jhang, Chung-Ying Tsai and many others. Those sincere friends of mine cheered me up while I was stranded badly in the bottleneck of my research, and they shared my happiness while I had breakthroughs. With their encouragement, my progress on my research became incredibly productive. Moreover, I would like to appreciate the staff in our department and the Nanoscale Fabrication and Characterization Facility: Albert Stewart, Cole Van Ormer, Shusheng Tan, and Matthew France. Without their great assistance, I could have not finished my thesis dissertation completely.

Finally, I want to express my best gratitude to my family members including my lovely parents, my older sister and my brother in-law, my uncles, aunts and cousins. They encouraged me to study aboard, and they helped me settle down in this exotic U.S. soil, which is several thousands of miles away from my country. They also assisted me to get accustomed to the life in the U.S., especially the language barrier in the first few years. They patiently listened to my happiness and sadness overseas by the telecommunication software even though we had at least 12 hours difference. Moreover, they all mentally supported me going through this PhD program unconditionally.

1.0 INTRODUCTION

Transparent conducting oxides (TCOs) fall into the category of wide-bandgap semiconductors featuring two physical properties that were considered to be mutually exclusive in general: (1) relatively high concentration of free carriers (>10^{19} cm^{-3}) with sufficient carrier mobility, and (2) extraordinary transparency due to near zero optical absorption in the visible wavelengths. Intrinsic oxides without intentional dopants are close to insulating materials. Doped with certain impurities that have an appropriate size, and a proper number of valence electrons, the carrier concentration can be much improved by several orders of magnitude, and the conductivity of these oxides can be only about two orders of magnitude lower than that of metals. This type of materials had received a great research attention for decades since this discover implied electrical and optical properties of TCOs can be tunable via adjusting the doping level of impurities.

In history, cadmium oxide (CdO) was the early n-type TCO material that was studied by Badeker in 1907 for the purpose of being a transparent conductor [1], which is an n-type semiconductor (carrier concentration in the range of 10^{18}-10^{20} cm^{-3}) that has bandgap of 2.18 eV at room temperature and holds a centrosymmetric structure of rocksalt, which is similar with the NaCl crystal. The interest of CdO had been dissipated since cadmium was considered as a lethal carcinogen that was responsible for lung cancer, and the usage of Cd-related compounds were strictly regulated. In addition, the optical absorption of CdO in the visible wavelength is inferior to other TCOs due to its relatively low bandgap. Therefore, researchers had to move their focus on

other nontoxic TCOs, such as tin oxide (SnO_2), indium oxide (In_2O_3), zinc oxide (ZnO) and the derivatives composed of these three with different ratios.

Among a variety of TCOs, tin-doped indium oxide (In_2O_3:SnO_2), which is customarily called indium tin oxide (ITO), was first discovered by Rupprecht in 1954, and was further developed by Boort and Groth in 1968 as the purpose of being a transparent conductor. ITO can be observed in many optoelectronic devices, notably serving as the transparent electrode for the replacement of opaque metal (Ag or Cu) electrodes, which significantly reduce the optical transmittance, and directly waste the electromagnetic radiation in those devices. Commercial ITO films still have the best TCO characteristics reported. In general, a 100 nm-thick ITO features a sheet resistance of 10 Ω/□, and its optical transmittance remains above 80 %. By means of its high electrical conductivity and optical transparency, ITO has not yet surpassed by other TCOs. However, there are some issues about ITO that have been reported: (1) indium is a rare metal that is extracted from zinc, copper, and lead ores. Heavy usage of ITO in the field of electronics such as display panels, light emitted diodes (LEDs), photovoltaics (PVs) and other commercial electronics, has caused a high demand for indium. For example, the world production of the indium mineral has risen from 300 to 700 tons per year over the past decade according to the statistics [2], the price of the indium has soared multifold in the same time span. Moreover, ITO is inherently too brittle to be applied onto flexible substrates such as plastics, which limits ITO in the field of flexible electronics. This problem has driven researchers to the question whether or not there is an alternative for the substitution of ITO that is rare-metal free and eco-friendly.

1.1 DEVELOPMENT OF ZINC-OXIDE-BASED TCOS

ZnO is one of TCO materials that can be usually found in the zincite ore ($Zn_XMn_{1-X}O$). It normally has the hexagonal wurtzite (WZ) structure where oxygen atoms fill a hexagonal closed-pack (HCP) lattice, and the zinc atoms fill half of tetrahedral sites with the lattice constants, a=0.325 nm, and c=0.521 nm **(Figure 1a)**. It was reported that the basic ZnO unit cell has a non-centrosymmetric crystal structure comprised of alternate layers of positive and negative ions, which refers to the zinc-terminated (0001) and oxygen-terminated ($000\bar{1}$) surfaces, leading to spontaneous polarization along the c-axis (**Figure 1b**)[3] [4]. Thus ZnO was initially applied to ultra-high frequency surface-acoustic wave (SAW) devices in the telecommunication industry in the 1960s due to its marvelous piezoelectric properties resulting from its alternating polar surfaces [5] to replace expensive quartz, which was the dominant SAW material.

More interestingly, ZnO was considered as excellent II-VI semiconductor that has direct bandgap (3.4 eV) and relatively large exciton-binding energy (60 meV) that is superior to other II-VI members such as ZnS and ZnSe. Based on such special characteristics, ZnO was a potentially attractive material for the light emitting diodes (LEDs) and UV-laser diode. Although reproducible p-type ZnO has not been confirmed due to its unstable thermodynamic state, which is discussed in the next subchapter, n-type ZnO and other p-type materials such as p-Si, GaN, $SrCu_2O_2$, ZnTe, Cu_2O, and NiO have been paired to form a p-n heterojunction for the application of such diode devices. The recent focus of ZnO has been to serve as the front transparent electrode in a variety of optoelectronics such as transparent thin-film transistors (tTFTs), thin-film photovoltaics and electrochemical solar cells, which are briefly introduced in the next few subchapter.

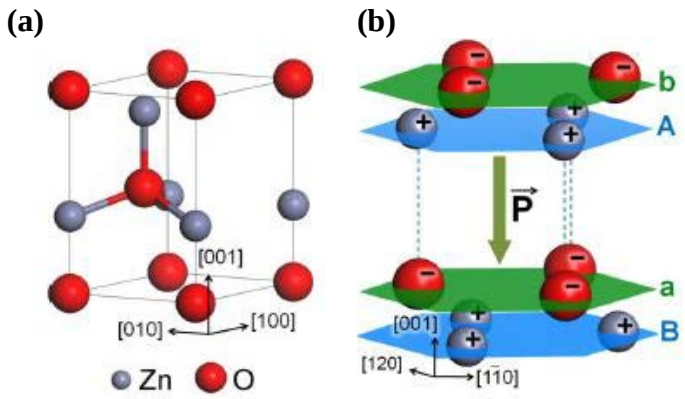

Figure 1 (a) Wurtzite structure of ZnO, and (b) the alternating polar layers of ZnO.

1.2 PROPERTIES OF ZINC OXIDE

1.2.1 Intrinsic Defects in ZnO

Intrinsic point defects in ZnO are caused by the displacement or removal of lattice atoms. Possible point defects are vacancies (missing atoms at regular lattice positions), interstitials (additional atoms occupying the interstitial sites of the lattice), and antisites (e.g. Zn atom occupies O site, and O atom occupies Zn site). The mechanisms of the Schocttky defect (a pair of cation and anion vacancies) and the Frenkel defect (a pair comprised of a cation vacancy and a cation interstitial) explain how those intrinsic point defects are formed in crystalline solids. In thermodynamics, the minimum defect concentration (N_d) is governed by the number of the available sites (N_0) in the lattice, the temperature (T), and the formation enthalpy per mole of defects (ΔH_d) (**Eq.1**). At the thermodynamic equilibrium, the change of Gibbs free energy of a crystal by defect formation (ΔG_d) has the minimum value, which is determined by the formation

enthalpy per mole of the donor defect (ΔH_d) and system entropy (S) associated with the distribution of defects on those available sites (**Eq.2)** [6].

$$N_d = N_0 exp(-\frac{\Delta H_d}{\mathrm{kT}}) \qquad \textbf{(Eq.1)}$$

$$\Delta G_d = \Delta H_d - \mathrm{T}\Delta\mathrm{S} \qquad \textbf{(Eq.2)}$$

It is convenient to link thermodynamics and the energy band structure with an example of n-type TCO since most TCOs are n-type semiconductor. That is, a donor defect can be neutrally or positively-charged depending on the position of donor level with respect to the Fermi level in the band structure (**Figure 2a**) [6]. For instance, when the Fermi level is above the donor level, the donor level tends to be fully occupied by electrons (neutral). On the other hand, the donor level will be unoccupied (positively-charged) and negatively-charged electrons will be present when the Fermi level is below its position. Thus, the difference (δ) between the donor level and the Fermi level is actually the criteria that determine the formation enthalpy related to the difficulty of the defect formation. Thus, the formation enthalpy of the donors is decreased by lowering the Fermi level (**Figure 2b**) [6].

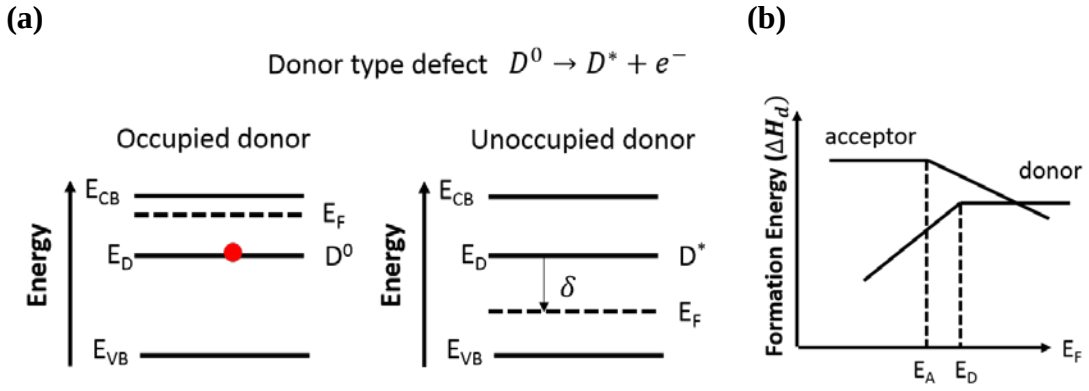

Figure 2. (a) The donor level is occupied by the electrons from the electron reservoir, and (b) The dependence of the defect formation enthalpy vs. the Fermi level position.

In the case of ZnO, possible intrinsic defects are zinc vacancies (V_{Zn}), oxygen vacancies (V_O), zinc interstitials (Zn_i), oxygen interstitials (O_i), zinc antisites (Zn_O) and oxygen antisites (O_{Zn}). Several experiments have suggests that undoped ZnO exhibits n-type conductivity due to oxygen vacancies (V_O) and zinc interstitials (Zn_i). Numerous experiments show that ZnO films made in an oxygen-deficient (zinc-rich) atmosphere exhibit higher electron concentration than that of the ZnO made in an oxygen-rich environment. Although this empirical result can be qualitatively explained by the fact that the enthalpy of formation for either V_O or Zn_i point defects in the zinc-rich condition is lower than that in the oxygen-rich condition (**Figure 3a-b**) [7], Some researchers such as Van de Walle et al. casted doubt on whether or not this effect is responsible for n-type conductivity in the ZnO material based on their theoretical calculations [7]. From their viewpoints, intrinsic defects of ZnO including V_O and Zn_i are not shallow donor impurities in n-type ZnO because the formation energy of those defects, even though in the condition of oxygen-deficient atmosphere, is still way too high [7]. Instead, those defects would act as deep donor impurities for p-type ZnO as undesired recombination centers. Alternatively, they suggest that extrinsic interstitial hydrogen incorporated in the ZnO lattice (either H_i or H_o) might serve as stable shallow donor impurities since the hydrogen atom is commonly present in the atmosphere. Those hydrogen-related impurities were the most-likely candidate that is responsible for the background n-type conductivity, which was erroneously attributed to oxygen vacancies and zinc interstitials in the past, in an unintentionally-doped ZnO material.

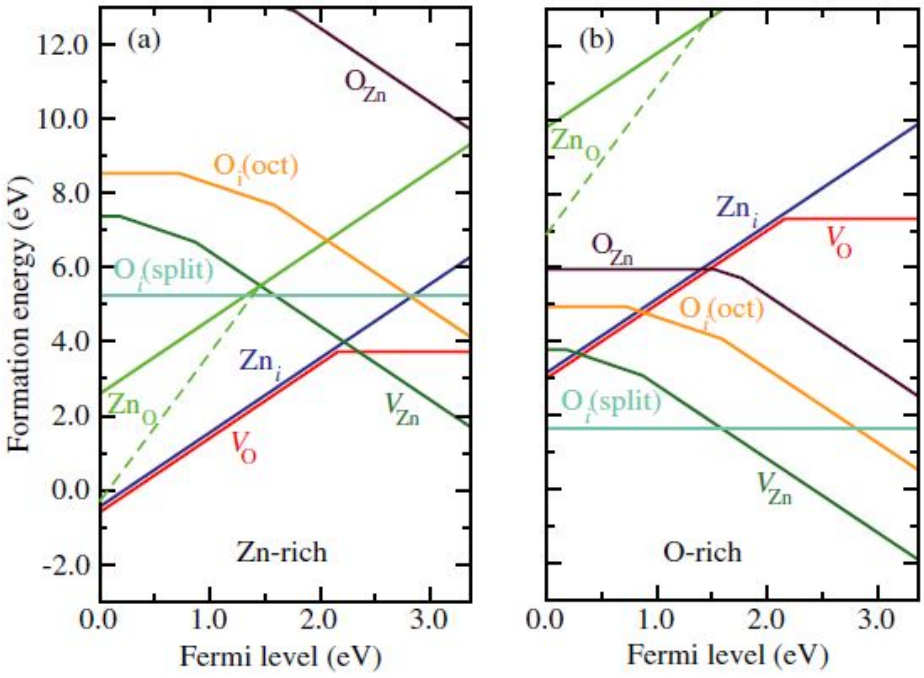

Figure 3. Formation energies of native point defects vs. the Fermi level position in the band structure of the n-type ZnO fabricated under (a) zinc-rich and (b) oxygen-rich conditions.

1.2.2 Common n-type impurities in ZnO

Electrical conductivity is governed by carrier concentration and carrier mobility (the carrier here refers to electrons in n-type semiconductors, and holes in p-type semiconductors), which is expressed in **Eq.3**:

$$\sigma = \frac{1}{\rho} = ne\mu \qquad \textbf{(Eq.3)}$$

where the σ represents electrical conductivity in units of S/cm or $\Omega^{-1}cm^{-1}$, and it is the reciprocal of the resistivity (ρ, Ω.cm) by definition. The n stands for the carrier concentration (cm^{-3}), and the μ is the carrier mobility ($cm^2/V.s$). The e is the elementary electric charge (1.602×10^{19} Coulomb per charge). Although an undoped ZnO material normally shows n-type conductivity, with carrier concentration (n) of $10^{17}cm^{-3}$, it does not fulfill the requirements to be a good electrical conductor.

To improve its electrical conductivity, extrinsic n-type impurity-doping is necessary. There two common n-type dopant categories: group III-A metals (B, Al, Ga, and In) substituting for Zn, and the group VIIA elements (F) substituting for O. For the case of III-A metals, the doping reaction is expressed in Kröger-Vink Notation as **Eq.4**:

$$M_2O_3 \overset{2ZnO}{\Longleftrightarrow} 2M_{Zn}^{\bullet} + 2O_o^X + \frac{1}{2}O_{2(g)} + 2e' \qquad (\textbf{Eq.4})$$

where M refers to the trivalent metal atom. The substitution of one mole of M_2O_3 in ZnO results in releasing two moles of conducting electrons, and a half mole of oxygen molecule into the atmosphere. At the same time, if the oxygen species do not diffuse quickly, they tend to be captured by native oxygen vacancies with conducting electrons, forming neutral oxygen lattices described in **Eq.5** [8]. Therefore, the electrical conductivity of the TCO film will be dramatically reduced, and the TCO film becomes insulating due to low carrier concentration.

$$\frac{1}{2}O_{2(g)} + V_O^{\bullet\bullet} + 2e' \Leftrightarrow O_o^X \qquad (\textbf{Eq.5})$$

The above chemical reaction also implies that the TCO films annealed in the reducing or low oxygen-deficient ambiences are preferred for the enhancement in conductivity. Furthermore, some transition metals such as Mo, Sc, Ti, Zr, V, Yi and Hf, etc. have also been incorporated as n-type dopants in ZnO films. Unlike the substitution with trivalent metals, they tend to capture oxygen atoms from the ZnO lattice, generating more oxygen vacancies and compensating electrons accordingly in order to obey the rule of the charge neutrality. Some experimental results of those common n-type impurities are listed in **Table 1** below **[9]**:

Table 1 The experimental results of ZnO films doped with a variety of n-type dopants

Dopant	Dopant Content (at. %)	Resistivity (10^{-4} Ω cm)	Carrier Concentration (10^{20} cm^{-3})
Al	1.6-3.2	1.3	15
Ga	1.7-6.1	1.2	14.5
B	4.6	2.0	5.4
Y	2.2	7.9	5.8
In	1.2	8.1	3.9
Sc	2.5	3.1	6.7
Si	8.0	4.8	8.8
Ge	1.6	7.4	8.8
Ti	2.0	5.6	6.2
Zr	5.4	5.2	5.5
Hf	4.1	5.5	3.5
F	0.5	4.0	5.0

1.2.3 P-type Impurities in ZnO

Although stable p-type TCOs are considered the key component toward invisible electronics comprised of p-n homojunctions, it is very difficult to fabricate p-type TCOs, and this is the reason why the choices of p-type semiconductors are very limited. To be more specific, The O_2p orbital of ZnO, which forms a hole transport path, is very localized (i.e., high hole effective mass), and the p-type doping impurities are compensated by many hole compensation centers that are inherently present in TCO since they are more thermodynamically favorable. These drawbacks lead to the low hole concentration and poor hole mobility. Despite of those reasons, there are still a few possible p-type dopants for ZnO such as monovalent metals (Li, Na, K, and Ag) [10, 11] for the substitution of zinc sites, and group V elements (N, P, As, and Sb) [5, 12] for substitution of oxygen sites. The monovalent metals can either substitute Zn sites as acceptors, or occupy interstitial sites as donors. However, it has been proven that the second route is thermodynamically favorable. An additional treatment is required to suppress the occurrence of the second route. The

nitrogen atom originating from NH_3 is considered the ideal p-type dopant because of its similar ionic radius with that of oxygen compared to ionic radii of other V-A elements (P, As ,Sb, and Bi) which are too large to occupy oxygen sites in the wurtzite structure [12, 13]. Since p-type dopants are not our concern in this study, we limit the discussion about p-type TCOs here. The audience can check other literature about this topic elsewhere if interested [5, 10, 14].

1.2.4 Carrier Transport Behavior in Conventional TCO Films

Electron mobility (μ) in semiconductors relies on the relaxation time (τ), electronic charge (e), and the effective carrier mass of the electron (m*) in the conduction band. The relations can be expressed in **Eq.6**

$$\mu = {e\tau}/{m^*} \qquad \textbf{(Eq.6)}$$

Therefore, to obtain high electron mobility, we should either decrease the effective mass (m^*) in the conduction band or increase the relaxation time (τ). The effective mass belongs to the material property and only small changes are possible. However, relaxation time associated with electron mobility is alterable by lowing defect density. Some electron scattering centers are listed below [15]:

Grain boundary scattering is caused by the discontinuity presented by grain boundaries (GBs), especially in polycrystalline films. Normally this is explained using the classic model originally issued by John Y. W. Seto [16]. Some electron trapping states (N_t) tend to capture conducting electrons from the conduction band. Thus, they become negatively-charged relatively in comparison to the interior of the grains. As a result, an energetic barrier of height (Φ) occurs, and a depletion zone is formed. Since then, electrons have to obtain sufficient thermal energy to overcome the barrier in order to transport across the grains, which is called thermionic emission.

As in **Figure 4a**, there are only a few electrons available in the conduction band, a few trapping states are charged, resulting the small Φ_1. In the **Figure 4b**, there are more electrons in the conduction band and trapping states might be almost fully-charged. As a result, the Φ_2 appears to be higher than Φ_1. This GB-limited carrier mobility can be expressed in **Eq.7** and **Eq.8**

$$\mu_{GB} = \mu_0 \, exp(-\frac{\Phi}{kT}) \qquad \textbf{(Eq.7)}$$

$$\mu_0 = \frac{eL}{\sqrt{2\pi m^* KT}} \qquad \textbf{(Eq.8)}$$

where Φ presents the energetic barrier, μ_0 is the prefactor related to the the grain size (L), m* is the effective mass of the electron in the conduction band, κ is the Boltzmann constant, and T is the temeprature. A plausible mechanism to explain this GB-limited model is shown in **Figure 4c** in which oxygen species in the air can be chemisorbed on the surface, and make the surface negatively-charged. This causes the energetic barrier across the grain boundaries in the surface, and reduces electron mobility and conductivity as well [17]. This explained why TCO specimens in relatively high humid surrounding exhibits poor conductivity.

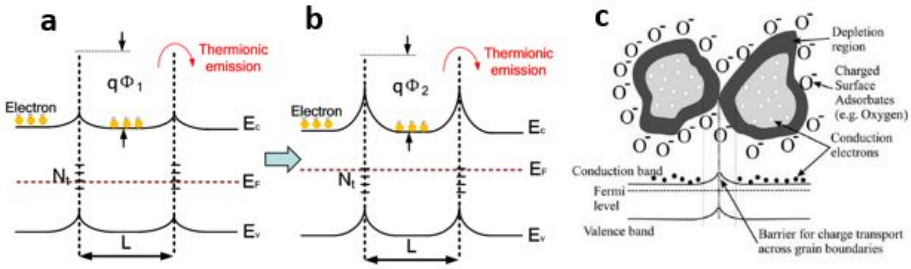

Figure 4. (a-b) Schematic mechanism of GB-limited carrier transport with different positions of Fermi level, and (c) schematic of the energetic barrier formed across GBs by chemisorbed oxygen species.

Ionized impurity scattering takes place when electrons are deflected by the long-range electrostatic force associated with charged impurities (**Figure 5a**) [18]. As the electron concentration is above 10^{20} cm^{-3} in the case of degenerate TCOs. The trapping states at GBs are

fully-charged, and the depletion width becomes narrower (**Figure 5b**). In this case, additional possibility for electron tunneling rises, and the energetic barrier is no longer effective due to this tunneling effect. As a result, the ionized impurity scattering becomes more significant, and electron mobility is now controlled by the electron-impurity interaction. The ionized impurity scattering in degenerate TCOs is described by the Conwell-Weissoft model (**Eq.9**) [19]

$$u_{ii} = \left(\frac{2}{m^*}\right)^{1/2} \left(\frac{\varepsilon^{1/2} {E_F}^{3/2}}{\pi e^3 N Z^2}\right) \left[\ln\left(1 + \frac{\varepsilon E_F}{Z^2 N^{1/3}}\right)\right]^{-2} \qquad \textbf{(Eq.9)}$$

where m* is the effective mass of the electrons, E_F is the Fermi level, ϵ is the static dielectric constant, Z is the valence charge of the impurities and N is the ionized impurity concentration. It is noteworthy that the ionized impurity scattering is independent of the temperature, which implies that the ionized impurity scattering has nothing to do with the thermionic emission in the case of degenerate TCOs (heavily-doped TCOs).

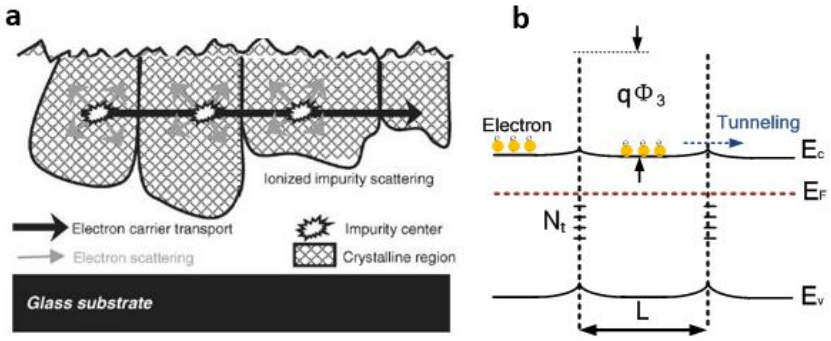

Figure 5. (a) The schematic diagram showing the transport path of electron impeded by the GB-scattering and ionized impurities. (b) The tunneling effect occurs in the case of degenerate TCO.

There are also minor scattering centers in the case of ZnO or other TCOs are discussed in addition to grain boundaries and ionized impurities. They have negligible influence on the carrier mobility but they could be important under certain circumstances. Those minor scattering centers are listed below:

Neutral impurity scattering is caused by non-ionized impurities.

Acoustic-phonon scattering is caused by an acoustic wave propagating through a crystal lattice. Accordingly lattice atoms oscillate from their equilibrium positions and interfere the electron transport.

Optical phonon scattering is due to lattice vibrations of bonds in a polar semiconductor (e.g. ZnO) which induce an electric field that impedes electron motion.

Piezoelectric scattering results from the local electric field induced by the distortion of the unit cell as strain is applied.

1.3 APPLICATIONS OF TCOS

1.3.1 Transparent Thin Film Transistors (t-TFTs)

Amorphous ZnO (a-ZnO) films containing post-transition metals referred to as transparent amorphous oxide semiconductors (TAOSs), have large Hall mobility (10-40 $cm^2/V.s$). The Hall mobility in TAOSs is usually compared to that of silicon-based semiconductors since the silicon is the semiconductor that has been studied for decades. Single crystalline Silicon (sc-Si) has very high carrier mobility (>200 $cm^2/V.s$ with the carrier concentration around 10^{19} cm^{-3}) whereas the mobility of the a-Si:H is very poor (1 $cm^2/V.s$). The poor mobility of a-Si:H is due to the fact that the carrier transport path in the a-Si:H consists of sp^3-bond orbitals with strong spatial directivity. Therefore, the structural randomness of chemical bonds (a-Si:H) definitely degrades the magnitude of sp^3-bond overlap. In the case of TAOSs, the conduction band minimum (CBM) is formed by vacant metal s-orbitals, which have an isotropic shape. Hence the s-orbital overlap with the

neighboring cations is less influenced by the distorted metal-oxide-metal chemical bonds. As a result, the Hall mobility is not degraded in TAOSs. The simulated hybridized chemical bonding in the sc-Si, a-Si, and TAOS materials are illustrated in **Figure 6** [20].

It is noted that the post-transition metals with the electron configuration of $(n-1)d^{10}ns^0$ where $n \geq 5$ are preferable because the degree of s-orbital overlap is determined by the principle quantum number (n) [21]. For example, In^{3+} or Sn^{4+} with an electronic configuration of $[Kr]4d^{10}5s^0$ are ideal metal choices for TAOSs. TAOSs are very suitable as a channel material in the field of flexible t-TFTs because it meets all the requirements: (1) transparency; (2) high carrier mobility; (3) low-temperature process; (4) high processability for large area coating. So far no other semiconductors have met these four requirements completely [22]. K. Nomura, A. Takagi et al. recently fabricated t-TFT device with a-IGZO channel layer exhibited high on/off current ratio ($\sim 10^6$) and great field-effect mobility (~ 10 $cm^2/V.s$) which are higher by one order of magnitude than those of a-Si:H or organic TFTs [23].

There are many deposition methods for TAOSs, including PLD, MOCVD, solution-based processes and so on. Among them, the solution-processed TAOSs are more favored because of equipment simplicity, inkjet printing availability in large coating area, low-temperature process and high throughput [21, 24, 25]. In general, TAOSs feature high optical transparency and relatively good electron mobility in contrast with the traditional a-Si:H and organic materials (exceeding a-Si by a factor of 10^1 and most organics by a factor of 10^2). It is noted that since TAOSs do not have grain boundaries, the GB-scattering mechanism that we observed in pc-TCOs is no longer applicable in the case of TAOSs [26].

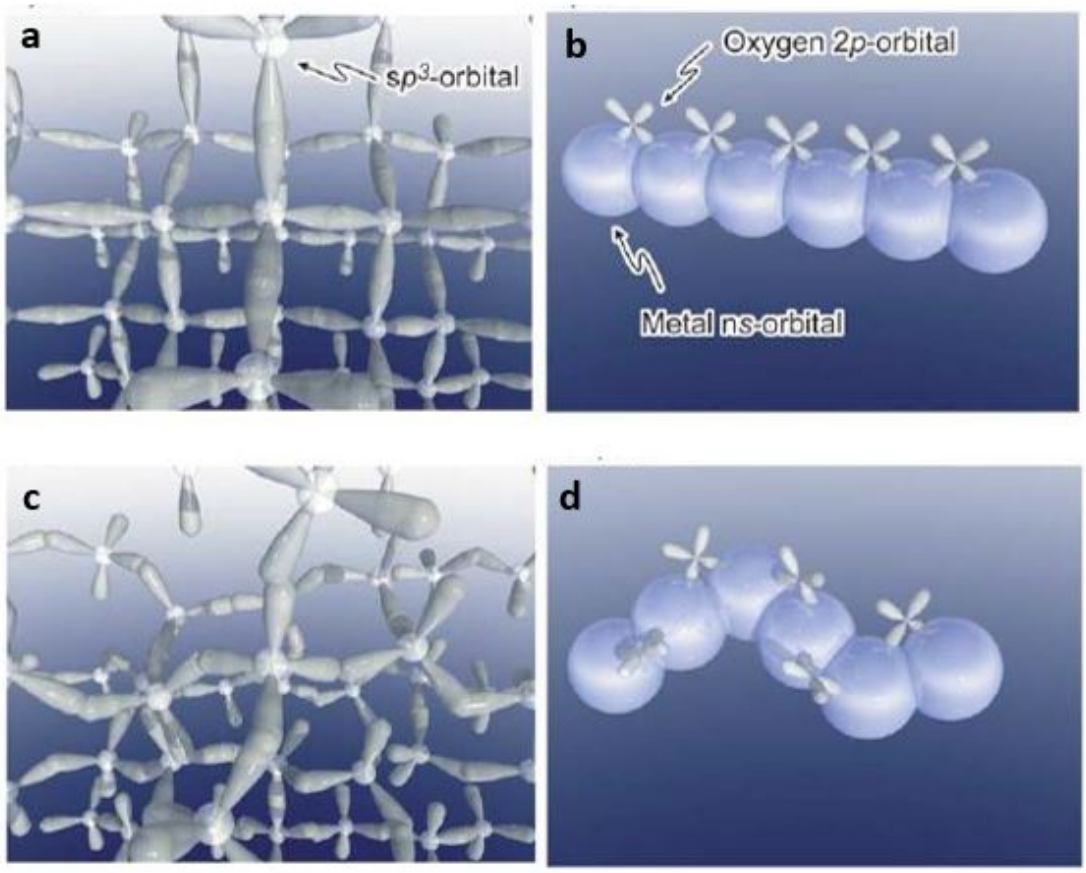

Figure 6. Schematic orbital drawings for the electron transport paths in (a) single crystalline silicon (b) single crystalline metal oxide, (c) amorphous silicon, and (d) amorphous metal oxide.

1.3.2 Dye-Sensitive Solar Cells

Dye-sensitive solar cells (DSSCs or DSCs) were developed by O'Regan and Grtäzel. The Kernel of a DSSC is a mesoporous semiconductor (e.g. TiO_2) layer deposited on a conducting transparent substrate. The dye molecules (polypyridinic Ru-complexes) are anchored onto this mesoporous semiconductor layer, and this mesoporous layer is filled with an electrolyte. The function of the dye molecule is to absorb solar radiations and generate photo-excited carriers. Electrons tend to transport from dye molecules to the conduction band of the semiconductor layer,

and are collected by the conducting electrode. The electrolyte in DSSCs have a redox couple donated as I^-/I_3^-. I^- is to oxidize dye molecules that lose electrons to the porous semiconductor layer and are recovered back from I_3^- to I^- at the counter electrode (**Figure 7**) [27].

Although anatase-TiO_2 was first used for the DSSC prototype, other oxide semiconductors such as ZnO, SnO_2, In_2O_3, Nb_2O_5, WO_3, Bi_2O_3 and $SrTiO_3$ have also been investigated for the replacement of the TiO_2 [28]. It was reported that nanostructured ZnO-based materials can be a promising substitute for the mesoporous TiO_2 layer, not only ZnO and TiO_2 have similar bandgap energies, work functions, but ZnO has a variety of nanostructured forms that can be produced by cost-effective procedure at low temperatures [29].

In addition, traditional thin TiO_2 or HfO_2 passivation layer on the dye-decorated TiO_2 is crucial in preventing the undesired recombination of electrons with the electrolyte [30]. This passivation layer can be also substituted with ZnO-based material as well since the carrier mobility of the wurzite-ZnO surpasses that of the anatase-TiO_2 [28]. This could significantly improve carrier transport of photoelectrons generated from the dye molecule toward the transparent conducting electrode, and sequentially improve the efficiency of DSSCs.

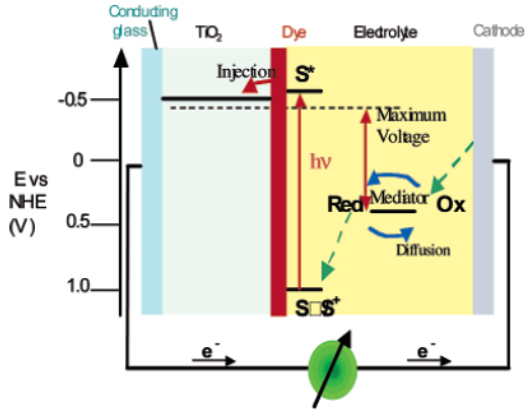

Figure 7. The Schematic of DSSC structure and its principle of operation of light conversion.

1.3.3 Perovskite Solar Cell

The efficiency of DSSCs is proven that several energy losses associated with metal-organic dyes limit the theoretical power conversion efficiency of DSSCs. One alternative is a hybrid inorganic-organic device that adopts the perovskite organic material. The structure is illustrated in **Figure 8** where cation A is the CH_3NH_3, the small cation B is the lead atom (Pb) surrounded by anion X, which is exchangeable with other halogens such as Br, Cl or I. This perovskite material is an advanced light-absorbing component instead of using Ru-based dyes that have short lifetime. Therefore, the perovskite solar cell is deemed as a modification of the DSSC in terms of the architectural structure. The progress in this field has been made rapidly since this structure was reported in the mid-2012. The energy conversion efficiencies of this perovskite solar cell already reached 16.2 % in the end of 2013. Moreover, a confirmed efficiency of 17.9 % was achieved in early 2014 followed by other claimed values as high as 19.3 % [31]. Numerous researchers have invested their efforts on this perovskite solar cell in the lab scale, and it is expected that the prototype of perovskite solar cells will soon surpass inorganic and organic photovoltaics.

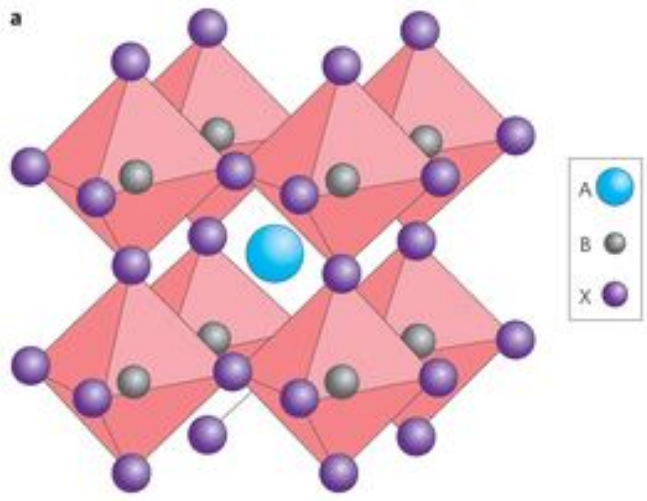

Figure 8. The schematic of a perovskite solar cell.

The prototype of a perovskite solar cell is comprised of a scaffold oxide semiconductor (TiO_2 or Al_2O_3) coated on a transparent conducting oxide substrate (ITO or FTO). The perovskite nanoparticles (methylammonium lead halide, $CH_3NH_3PbX_3$, X=halogens such as Br, Cl, and I) and a solid hole-transport layer (HTL, spiro-OMeTAD) are coated on this scaffold oxide semiconductor layer (**Figure 9a-d**) [32].

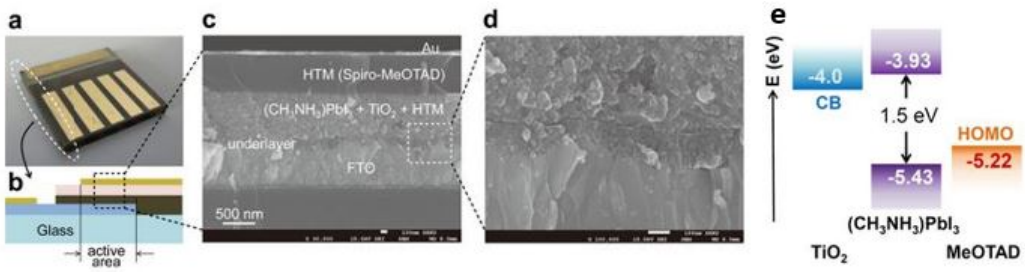

Figure 9. (a) The real perovskite solar cell device. (b) The schematic structure of the perovskite solar cell. (c-d) the cross-sectional SEM images. (d) The schematic energy level diagram.

The scaffold TiO_2 layer in the perovskite solar cell, Similar with that of DSSCs, can be substituted by a nanostructured ZnO layer that possesses relatively high carrier mobility. D. Liu, T. Kelly et al. fabricated a perovskite device with the architecture of ITO/ZnO nanocrystals /$CH_3NH_3PBI_3$/HTL/Ag (**Figure 10a-b**) by solution-processing techniques at room temperature [33]. This ZnO-halide heterojunction perovskite solar cell exhibited an open-circuit voltage (V_{oc}) of 1.01 V and a short-circuit current (J_{sc}) of 20.4 mA/cm^2 with the fill factor (FF) of 70 %. They also claimed the conversion efficiency up to 15.7 % under AM 1.5G simulated illumination.

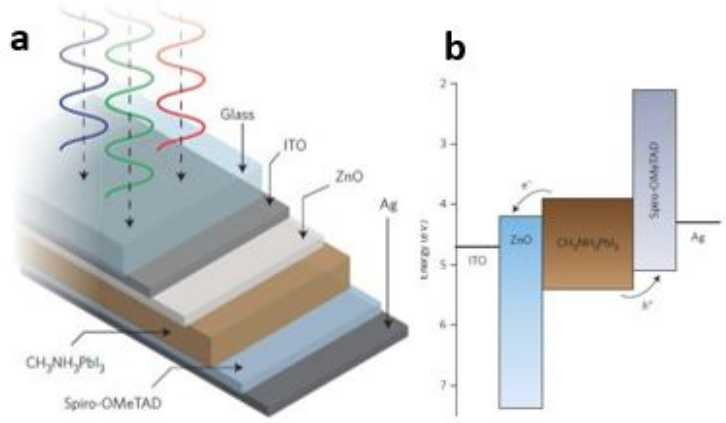

Figure 10. (a) The schematic architecture of the ZnO-halide planar heterojunction perovskite solar cell. (b) The schematic energy levels of this perovskite solar cell.

Moreover, D.-Y. Son, J.-H Im et al. tried to optimize their 1-D ZnO nanorods for TiO_2 substitution shown in **Figure 11a** [34]. This ZnO nanorods-based perovskite solar cell showed the V_{oc}= 0.991 V, J_{sc} =20.08 mA/cm^2 with the FF= 56 %. The conversion efficiency was measured up to 11.13 % under AM 1.5 G simulated illumination, and the external quantum efficiency (EQE) was above 80 % in almost the entire visible wavelength from 400-750 nm shown in **Figure 11b.**

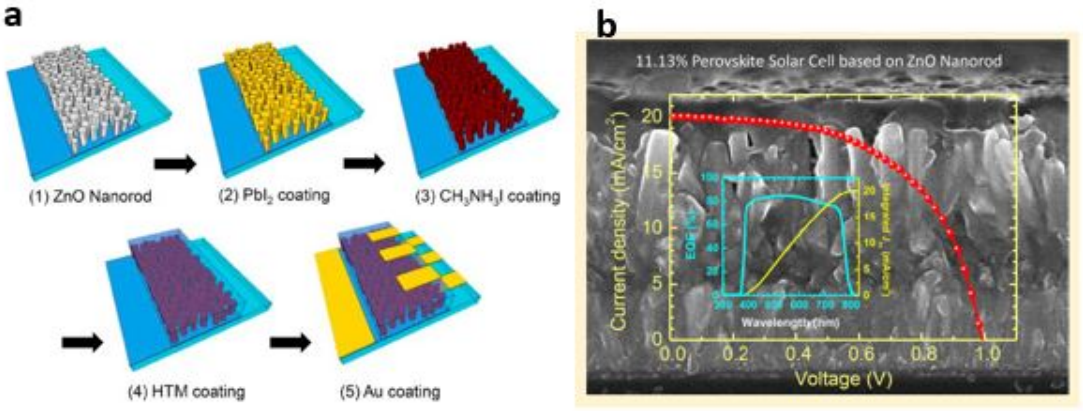

Figure 11. (a) Fabrication process of this ZnO nanorods-based perovskite solar cell. (b) The cross-sectional SEM image of this ZnO nanorods-based perovskite solar cell.

1.4 CURRENT ISSUES OF TCO ELECTRODES

1.4.1 Trade-off in carrier density and carrier mobility in TCO Films

The overall mobility can be simply expressed in **Eq.10** where μ_i is the mobility due to i-th scattering mechanism. The physical meaning of this equation is that the reciprocal of overall mobility is the summation of each resistance originated from corresponding scattering mechanism. This overall mobility, usually obtained via Hall-effect measurements, is expressed below:

$$1/\mu = \sum_{i=1}^{n} 1/\mu_i \qquad \textbf{(Eq.10)}$$

A high carrier mobility is very critical in terms of the performance of optoelectronic devices. T. Yamamoto, H. Song et al. studied on the carrier mobility of their polycrystalline Ga-doped ZnO (pc-GZO) films compared with the Hall mobility (μ_H) obtained from the Hall-effect measurements with the optical mobility (μ_{opt}) derived from the spectroscopic ellipsometry, which is associated with the scattering within grains or so-called ingrain scattering [35]. They found out that μ_H is dependent of film thickness. When the thickness (t) increases above the critical length (350 nm), the μ_H approach the μ_{opt} (**Figure 12a)**. This interesting result implies that the GB-scattering is initially dominant when the pc-GZO film thickness is less than 350 nm. However, the GB-scattering is attenuated as the film thickness reaches the 350 nm due to the great reduction of the GB density caused by the columnar grain growth along c-axis, or a narrow depletion region at GBs occurs in the case of heavily doped TCOs. In such conditions, ingrain scattering, which is caused by ionized impurities, becomes significant. That is, as the electron concentration is above 10^{20} cm^{-3}, the ionized impurity scattering is noticeable. This phenomenon can be clearly observed in the hall mobility vs. carrier concentration diagram shown in **Figure 12b [9]** based on empirical

reports and theoretical calculations. In degenerate TCOs, the electron motion is limited by its ionized impurities. As a result, a very important trade-off between the carrier concentration and the carrier mobility, which saturates the conductivity to a certain level and cannot be further improved.

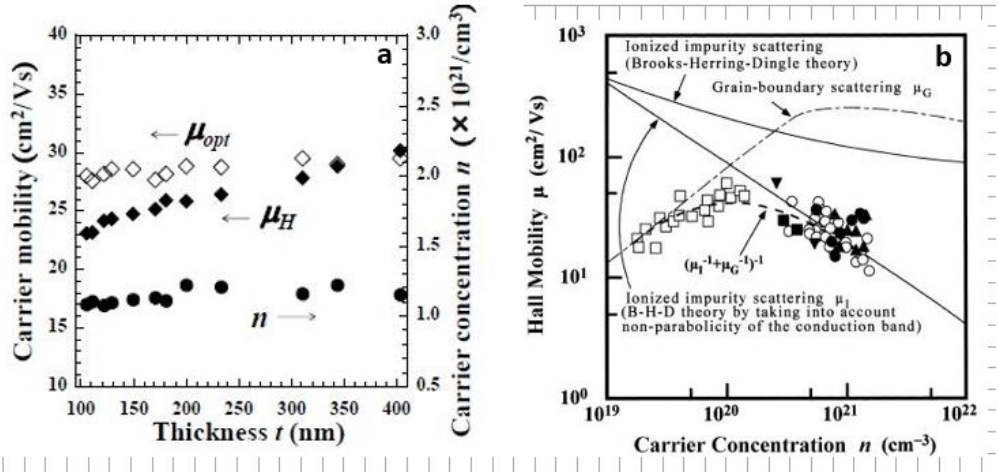

Figure 12. (a) The optical mobility (μ_{opt}), Hall mobility (μ_H), and the carrier concentration vs. pc-GZO film thickness (b) The Hall mobility as function of the carrier concentration in the impurity-doped ZnO film. Two solid lines are the simulated ionized impurity scattering predictions based on two theories.

1.4.2 Degraded optical transparency influenced by impurities.

The transparency window of TCO materials is defined by two distinct boundaries. One is normally near the ultraviolet (UV) region governed by the effective bandgap and it is involved in the direct transition of electrons from the valence band to the conduction band. The other is near the infrared (IR) region and it is governed by the plasma frequency (or plasma wavelength) of the conduction electrons (**Figure 13**) [36].

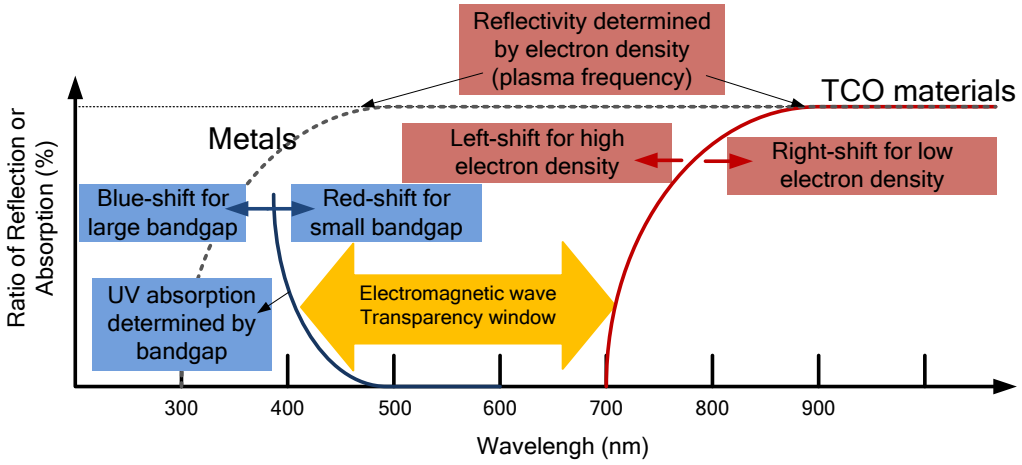

Figure 13. The schematic showing the electromagnetic transparency window is defined by the effective bandgap in the UV region (blue), and the plasma frequency of the materials in the IR region (red).

The bandgap determines whether electrons absorb the electromagnetic radiation at certain wavelength and are excited into a higher energy band. The plasma frequency (it can be converted to plasma wavelength) describes the frequency at which when the charged particles (e.g. electrons) begin to collectively respond to an electromagnetic field. When the incident radiation has the frequencies higher than the plasma frequency, the conduction electrons do not oscillate collectively. On the contrary, electrons interact with the incident radiation as the frequency of the incident radiations is equal or lower than the plasma frequency. In general, the plasma frequency increases in proportion to the square root of the carrier concentration. The resistivity and the correlated plasma wavelengths of TCOs are tabulated in the **Table 2** showing this strong correlation between the carrier concentration and the plasma frequency.

Table 2 The resistivity and the corresponding plasma wavelengths of materials

Material	Resistivity ($\mu\Omega$ cm)	Plasma Wavelength (μm)
Ag	1.6	0.4
TiN	20	0.7
In_2O_3:Sn	100	>1.0
Cd_2SnO_4	130	>1.3
ZnO:Al	150	>1.3
SnO_2:F	200	>1.6
ZnO: F	400	>2.0

Regarding the transparency window, the boundary blue-shifts in the UV region, known as the Burstein-Moss (BM) effect, which is attributed to excessive electrons occupying energy levels that are nearly higher than the conduction band minimum (CBM). Therefore the interband optical transition needs a higher photon energy to overcome the bandgap plus the Burstein-Moss shift (**Figure 14a**). The boundary shifts toward shorter wavelength in the IR region is due to the increased reflectance by the free electron motion of the material. Moreover, this shift in the IR region is more significant than the BM-shift in the UV region. Overall, the transmission window is narrower when the carrier concentration increases.

In the electronic structure of an ideal TCO material, the metal's empty p band (M_p) is above its hybridized band formed by the metal s-orbitals with neighboring oxygen 2p-orbitals (M_s+O_p). In order to keep the transparency window in the visible spectrum (λ=390-700 nm), two interband absorption energies (E_v and E_c) should be higher than 3.0 eV, and the intraband transition (E_i) associated with the plasma oscillation should be less than 1.8 eV (**Figure 14b**).

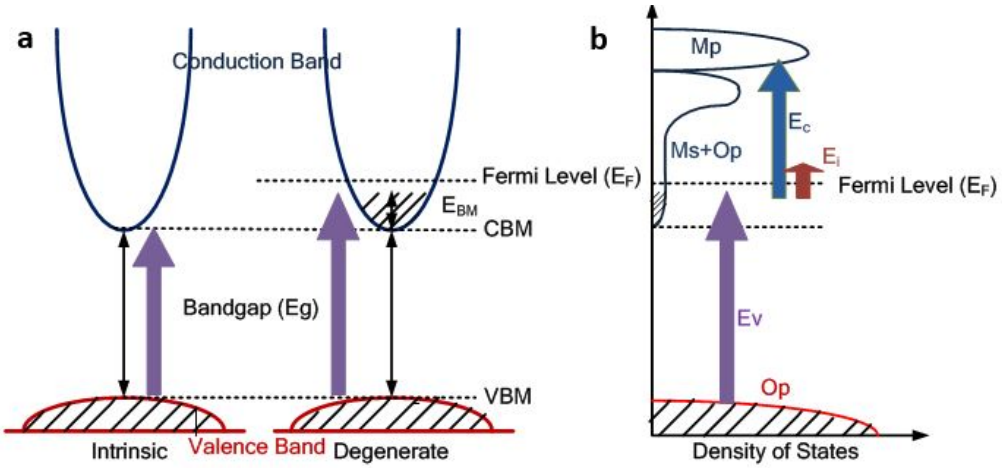

Figure 14. Schematic electronic band structures of (a) degenerate TCO, and (b) the interband and intraband absorptions in an ideal TCO material.

In reality, having good electrical and optical (E/O) properties seems contradictory. Although the BM effect broadens the transmission window slightly in the UV region, plasma oscillation causes the dramatic shrinkage of the transmission window in the IR region. The correlation of the transmission window affected by the effective bandgap and the plasma frequency of TCO materials as a function of the incident wavelength is shown in **Figure 15** [36]**.**

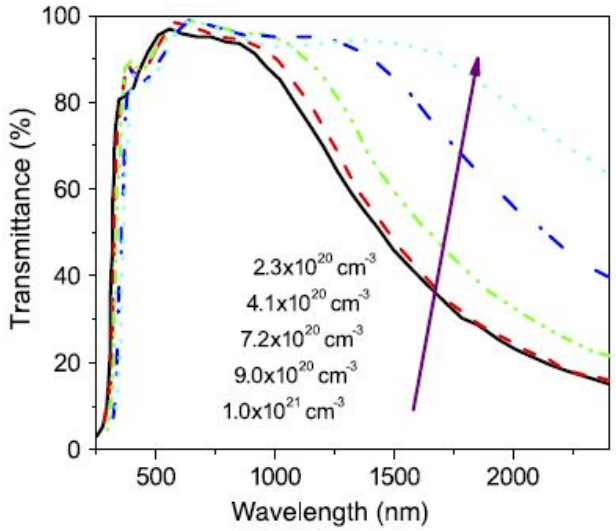

Figure 15. The width of the transmission window in TCOs is defined by the carrier concentration.

2.0 ENHANCED ELECTRICAL PROPERTIES BY METAL NANOPARTICLES

2.1 MOTIVATION

Saturated conductivity is caused by the severe trade-off between the carrier concentration and carrier mobility in heavily-doped TCOs. This suggests that an approach that increases the mobility rather than the carrier concentration by impurity doping is the solution to make TCO films with high figure of merit (FOM). In order words, this approach improves the conductivity of TCO films but the optical transparency is not degraded since the impurity level is low.

It was a proof-and-concept that conducting electrons can be separated spatially from their parent impurity atoms in order to circumvent the ionized impurity scattering. This concept is called modulation doping. To carry out this approach, several researchers prepared an undoped GaAs potential well bounded by doped AlGaAs layers for the application of high electron mobility transistors (HEMTs) [37]. Therefore, conducting electrons provided by doped AlGaAs drift into the undoped GaAs potential well. As a result, reduced impurity scattering can be expected.

Adopted from this modulation doping, the structure that consists of two semiconductor layers with alternating doping levels brought attention to people. Thus, electrons donated from the high-carrier layer, can be transported in the high-mobility layer with the minimal influence from the charged impurities. In order to achieve this model, electrons should be able to move into the high mobility material via a certain driving force such as a difference in work functions. Besides,

the thickness of the each layer should be in the range of nanometers, which is comparable to the Debye length, in order to achieve a successful transfer.

Cohen and Barnett conducted a simulated research on their ZnO/ZnMgO/ZnMgO:Al multilayer structure [38]. They essentially investigated how the film thickness, and the donor level can affect the conducting electrons transferred from the doping layer (ZnMgO:Al) to the transport layer (ZnO). Eventually they concluded that this system had a possible electron mobility up to 145 $cm^2/V.s$ at the average carrier concentration of 3.8×10^{18} cm^{-3}.

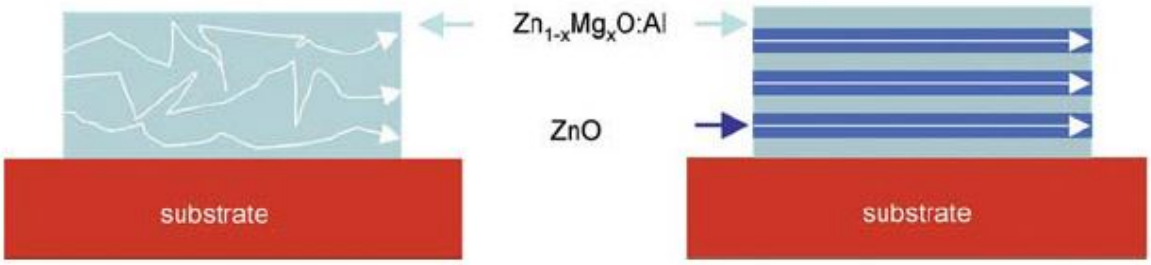

Figure 16. Conduction electrons transport in a homogenous $Zn_{1-x}Mg_xO$:Al film (left side), and a modulation-doped film composed of alternating doped $Zn_{1-x}Mg_xO$:Al and ZnO layers (right side).

Despite those appealing simulated results, the ZnO/AZO, ZnO/$Zn_{1-X}Mg_XO$:Al films on c-sapphire substrate fabricated by K. Ellmer et. al. showed high resistivity. This was later ascribed to the high oxidation of the films. [39]. Similarly, Rauf introduced a zone confining process for their ITO films in 1993, in which the temperature gradient was created by the heating coil [40]. This temperature gradient was served as the driving force that drove the impurities from the high temperature region into the low temperature region. The impurity movement was actually parallel to the temperature gradient and perpendicular to the film growth. This process was deemed as the most economical way to fabricate selective-doping ITO films. Using this method, the ITO film

exhibited high mobility. However, the transmittance of this film prepared by this zone-confining technique fell short on their expectation.

The approach of modulation doping was also applied to metal-oxide composite materials. Previous studies suggested that a metal nanolayer inserted in the ZnO films increased the carrier concentration as long as the metal layer thickness reached the threshold value [41, 42] . However, the electron mobility was confined within 10 $cm^2/V.s$, which was speculated that the metal donated electrons to ZnO matrix, but the surface of the metal constituent acted as a new scattering center.

Inspired by the results from TCO/metal/TCO multilayer films, we conducted the study on the TCO films containing trace amount of metal NPs as the electron ejectors. Due to lack of published studies on the carrier transport in such composite films, the temperature-dependent Hall-effect analysis was employed to investigate the electron injection and scattering in these composite films. Au NPs were tentatively chosen because they have an excellent thermal stability [43]. The measurements eventually provided an important clue as to the electron emission and transport mechanisms in these conductive Au NP embedded ZnO films.

2.2 EXPERIMENTAL DETAIL AND APPARATUS

2.2.1 Preparation of ZnO Sol-gel

The ZnO sol-gel precursor was composed of zinc acetate dihydrate [$Zn(O_2CCH_3)_2 \cdot 2H_2O$, 99.99 %] dissolved in 2-methoxyethanol [$CH_3O(CH_2)_2OH$, 99.8 %] with monoethanolamine [MEA, $NH_2(CH_2)_2OH$, 98%] serving as a sol stabilizer. The Zinc precursor was aged for one day before coating. The entire sol-gel mechanism is following:

Several nucleophilic species such amines (MEA), and acetates (CH_3COO^-) will compete to form complexes with the cation Zn^{2+}. The Zn-MEA or Zn-acetate complexes attacked by hydroxyl group (**Figure 17**) later develop into a network throughout the entire liquid medium, transforming into a viscous gel during the aging process**.** The stabilizer (MEA) plays a vital role in the initial stage by controlling the pH value of the sol, which balances the reaction rates of the hydrolysis and condensation reactions [44]. Without the assistance of MEA stabilizer, undesired white precipitate associated with $Zn(OH)_2$ is observed, and this white substance definitely harms the formation of ZnO films as well as the electrical conductivity.

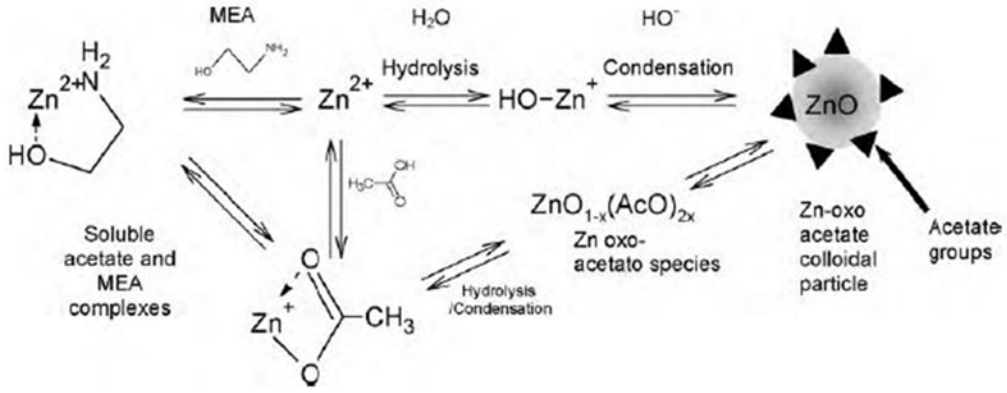

Figure 17. The mechanism of the ZnO formation via the sol-gel process

ZnO sol-gel precursor was spin-coated on surface-oxidized silicon (100) substrates at a rate of 3000 rpm, followed by baking on a hotplate in order to remove organic residues, and the heat treatment at 500 ℃ under N_2 atmosphere for high crystallinity. This is illustrated in **Figure 18**:

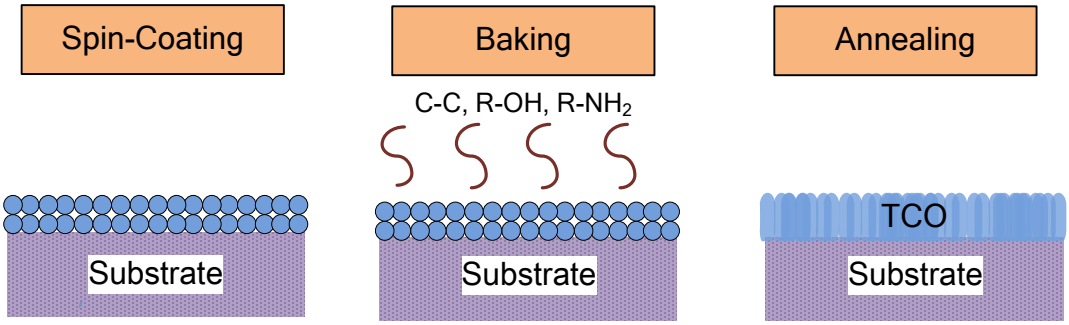

Figure 18. The spin-coating process for TCO thin film fabrication.

2.2.2 Fabrication of the ZnO/Au NPs/ZnO Composite Films

A gold (Au) mid-layer was initially deposited onto the bottom ZnO layer with varied Au thicknesses as 3.0, 5.0, 7.0 and 10 nm via the e-beam evaporation. The e-beam evaporation has the anode target material (Au) bombarded by a hot electron beam generated by a tungsten filament in the vacuum condition (~10^{-7} torr). Target molecules are gradually vaporized from the target, and deposited onto our substrates, which are mounted on the substrate dome. The deposition rate can be controlled at minimum of 0.1 nm/s, and the thickness of thin film can be measured by the change in frequency of a quartz crystal microbalance (QCM) near the substrate. The configuration of this e-beam evaporator is illustrated in **Figure 19** [45].

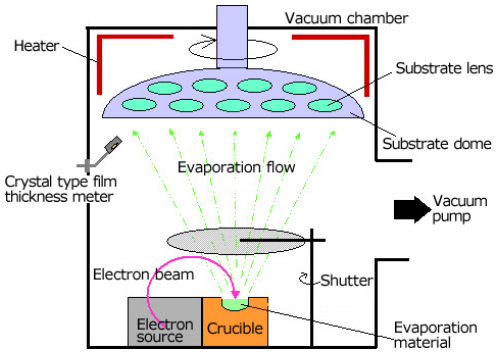

Figure 19. The schematic of e-beam evaporator.

The top spin-coated ZnO layer was deposited as a capping layer after the Au evaporation. All samples for our convenience were labeled as ZnO/ZnO (control sample without Au layer), ZnO/Au-3nm, ZnO/Au-5nm, ZnO/Au-7nm, and ZnO/Au-10nm hereafter. Those composite films were annealed in the tube furnace at 500 ℃ in N_2 atmosphere. It is noted that after annealing the Au nanolayer will eventually transform into Au nanoparticles schematically drawn in **Figure 20**.

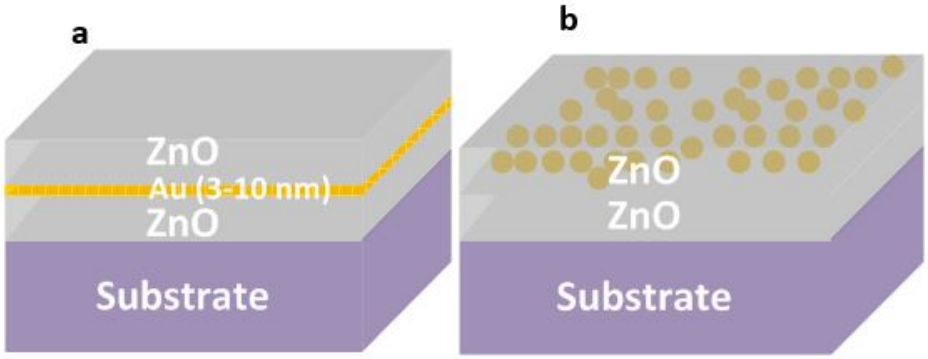

Figure 20. The schematic structure of ZnO/Au/ZnO (a) as-deposited, and (b) after annealing.

2.2.3 X-ray Diffraction

2.2.3.1 Conventional θ-2θ XRD

X-ray diffraction (XRD) is a non-destructive analytical technique that is primarily used for phase identification of a crystalline material. By heating a tungsten filament, a beam of electrons is emitted and accelerated by a high voltage toward the metal target (usually Cu, Co, Mo, or Fe). While the accelerated electron beam bombards the target material, electrons in the K shell (1s) of the metal target are knocked out, and the vacancies are filled by other electrons from L (2p) or M (3p) shell. Therefore, two main X-ray lines (K_α and K_β) with a small difference in wavelength are always present. By reducing the magnitude of the K_β line by an iron β-filter, a monochromic X-ray is generated. A crystalline sample has periodic order of atoms, which can be treated as a natural

diffraction grating in atomic scale. While the incident X-ray with this crystalline sample will have constructive interference when the conditions satisfy the Bragg's law ($2d\sin\theta=n\lambda$). By scanning a range of incident angles, diffracted X-ray beams corresponding to crystallographic planes of the sample which both satisfy the Bragg's law, and have less Thomson scattering (strong structure factor) are counted. Therefore, the crystallographic structure of the sample is revealed.

2.2.3.2 Glancing angle XRD

In the conventional X-ray diffraction with θ-2θ (or called Bragg-Brentano) geometry, the incident angle is equal to the angle of the diffracted beam regarding the inspected sample surface (**Figure 21a**). However, this configuration is not suitable for thin-film samples (~nm) since the penetration depth of the X-ray is proportional to $\alpha^{-1}Sin\theta$ (α is the absorption coefficient), and $\alpha^{-1}$is normally from 1~100 μm. Therefore, the total signal of θ-2θ diffraction is mainly collected from the substrate instead of the contribution from the thin film. Glancing angle X-ray diffraction (GAXRD) has been developed to overcome this limitation. The monochromic X-ray reaches the surface of the sample with a fixed, low glancing angle, the diffraction pattern is collected by moving the detector without rotating the sample (**Figure 21b**). The configuration of this GAXRD is shown in **Figure 21** [46]. As the result, the microstructure of the thin-film can be identified, and the noise from the substrate can be reduced significantly by this GAXRD technique.

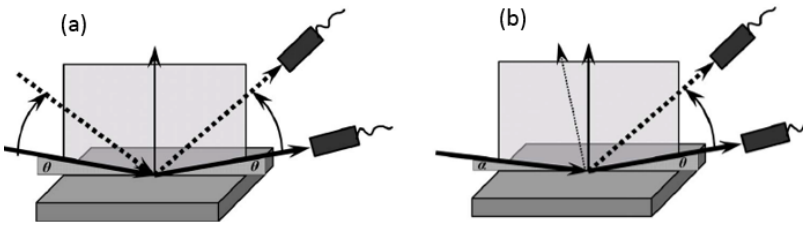

Figure 21. Schematics of (a) conventional θ-2θ XRD, and (b) GAXRD with low glancing angle.

2.2.4 Four-point Probe and Van der Pauw Method

The resistivity of a sample is commonly measured by four-point probe method (**Figure 22**). By applying a small amount of current (I) between two outer probes, the voltage within two inner probes is measured. Given the thickness (t) and the diameter (d), the resistivity can be expressed below on the condition that $t \ll d$:

$$\rho = \frac{1}{\sigma} = \frac{V}{I} \cdot \mathrm{CF} \qquad \textbf{(Eq.11)}$$

Where CF is called the correction factor depending on the t/s ratio of the sample (s is the distance of the probe).

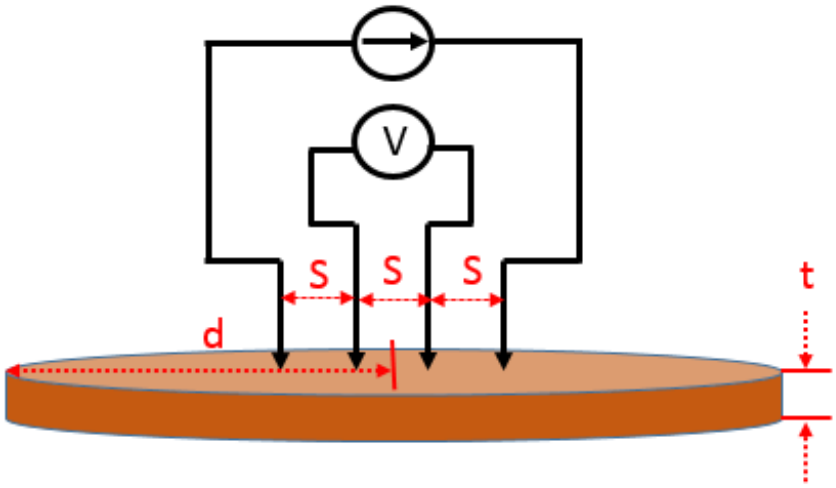

Figure 22. The schematic diagram of the four-point probe method.

The relation of t/s ratios and CFs values are tabulated in **Table 3.** For example, CF is 4.532 for the case of a thin-film sample since their thickness is always negligible as compared to its diameter.

Table 3. Correction factors (CFS) for different d/s ratios of samples

d/s	CF
10	4.1712
20	4.4364
30	4.4892
40	4.5080
50	4.5167
100	4.5284
200	4.5314
∞	4.5320

However, this traditional four-point probe is very geometry-sensitive. Therefore the resistivity based on **Eq.11** is far beyond the accuracy if the sample is not regular. Hence, Leo J. Van der Pauw proposed a technique in 1958 in order to resolve this common problem, and obtain more precise measurement in the resistivity (conductivity) in an irregulary sample as long as the sample is two-dimensional (t/d is close to zero) and the thickness is a constant. The Van der Pauw technique is illustrated in **Figure 23**. For example, A current flow is applied across point 3 and point 4, then a voltage is measured across point 1, and point 2. Hence the resistance (R) is calculated by V_{12} devided by I_{34}, which is denoted as $R_{34,12}$,based on simple ohmic law. Similarily we can obtain $R_{12,34}$, $R_{14,23}$, $R_{23,14}$ and another four measurements ($R_{43,21}$, $R_{21,43}$, $R_{41,32}$, $R_{32,41}$) by swiching directions of current flows.

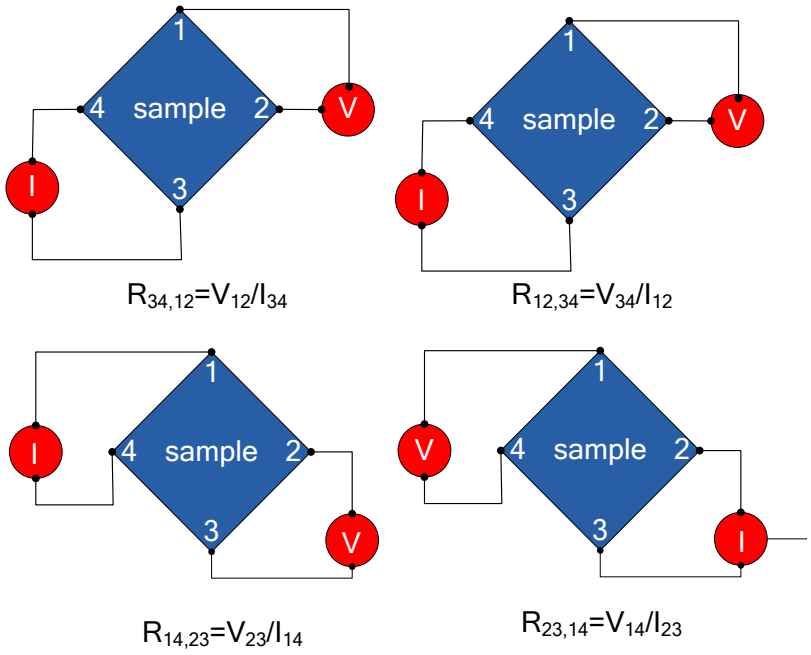

Figure 23. Van der Pauw configuration for the resistivity of an irregular sample.

By using this Van der Pauw method, the sheet resistance can be estimated by the van der pauw formula (**Eq.14**), which is considered as the modification for this traditional four-point probe method.

$$R_{Vertical} = \frac{R_{34,12} + R_{12,34} + R_{43,21} + R_{21,43}}{4} \quad \textbf{(Eq.12)}$$

$$R_{horizontal} = \frac{R_{14,23} + R_{23,14} + R_{41,32} + R_{32,41}}{4} \quad \textbf{(Eq.13)}$$

$$e^{\left(\frac{-\pi R_{vertical}}{R_S}\right)} + e^{\left(\frac{-\pi R_{herizontal}}{R_S}\right)} = 1 \quad \textbf{(Eq.14)}$$

If $R_{Vertical}$ and $R_{horizontal}$ are identical (R), the sheet resistance can be simplified as:

$$R_S = \frac{\pi R}{ln2} \quad \textbf{(Eq.15)}$$

2.2.5 The Principle of the Hall-effect Measurement

When an electric field (**E**) and a magnetic field (**B**) is applied to a positively charged carrier (holes) moving with a velocity (**v**) in a p-type bar (**Figure 24**), the Lorentz force is applied [37]:

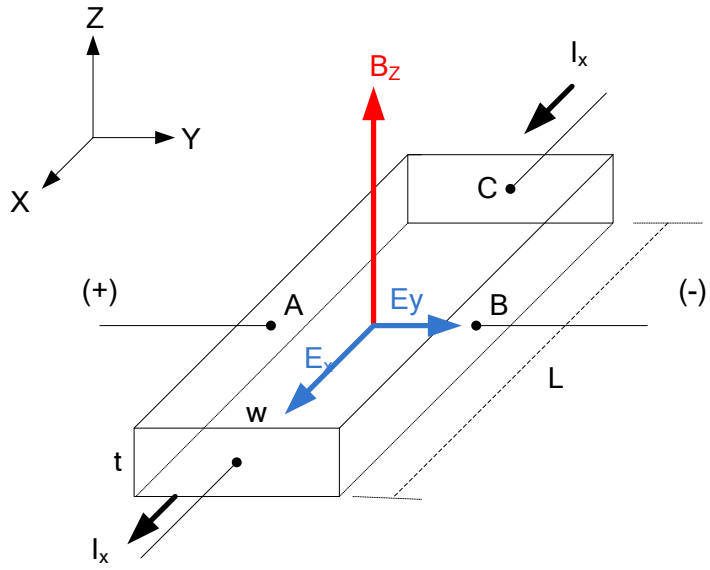

Figure 24. Hall-effect analysis on a bar-shaped p-type semiconductor.

$$\mathbf{F} = \mathrm{q}(\mathbf{E} + \mathbf{v} \times \mathbf{B}) \qquad \textbf{(Eq.16)}$$

the Lorentz force in y-direction is:

$$F_y = \mathrm{q}(E_y - v_x B_Z) \qquad \textbf{(Eq.17)}$$

since the net force should be balanced in y-direction,

$$E_y = v_x B_Z \qquad \textbf{(Eq.18)}$$

since the relation of current flux (J_x), the hole velocity (v_x), and the hole concentration (p_0) of this p-type bar can be described as:

$$J_x = v_x q p_0 \qquad \textbf{(Eq.19)}$$

the **Eq. 13** can be rearranged as:

$$E_y = \frac{J_x}{qp_0} B_Z = J_x R_H B_Z \,, \quad R_H \equiv \frac{1}{qp_0} \text{ (Hall coefficient)} \qquad \textbf{(Eq.20)}$$

linked the physical parameters with the dimension (L, w, and t) of this bar, the hole concentration (p_0) in this p-type bar can be expressed:

$$p_0 = \frac{1}{qR_H} = \frac{J_x B_Z}{qE_y} = \frac{(I_x/_{wt})B_Z}{q(V_{AB}/_w)} = \frac{I_x B_Z}{qtV_{AB}}, \quad (V_{AB} \text{ is the Hall voltage}) \qquad \textbf{(Eq.21)}$$

therefore, the hole concentration of this bar sample can be obtained since all parameters in the right hand side are measureable. The principle is also applicable for the n-type semiconductor. According to **Eq.3**, the Hall mobility can be calculated if the resistance of the sample is obtained by the Van der Pawl technique, which is specially modified for thin-film specimens based on the traditional four-point probe method.

2.3 ZINC OXIDE FILMS EMBEDDED GOLD NANOPARTICLES

The crystal structures of all Au NP-embedded ZnO films were characterized by GAXRD with Cu-Kα radiation of λ=0.154 nm. All samples exhibited random orientations of the hexagonal ZnO structure with the preferred Au (111) phase (**Figure 25a-b**). It is interesting that the ZnO (002) was more dominant when the intensity of Au (111) diffraction peak became stronger. This might be due to the small lattice mismatch between hexagonal ZnO (002) and cubic Au (111) phases [43]. It is noteworthy that a non-degenerate TCO film with the preferred orientation usually has higher Hall mobility due to the reduction of GB-scattering centers. Au NP crystallite sizes of our composite films are estimated around 18-20 nm based on the Scherrer's formula below:

$$D = \frac{K\lambda}{B \cdot cos\theta} \qquad \textbf{(Eq.22)}$$

where D is the crystallite size, K is the shape factor that is close to 0.90. B is the line broadening in radians at the Full-width-half-maximum denoted as $\Delta(2\theta)$. It is noted that B is usually calibrated by subtracting the instrumental line broadening in order to obtain the crystallite size accurately. Since the Au NP size do not varied significantly from sample to sample, we can assume that our embedded Au NP population density is proportional to the Au layer thickness.

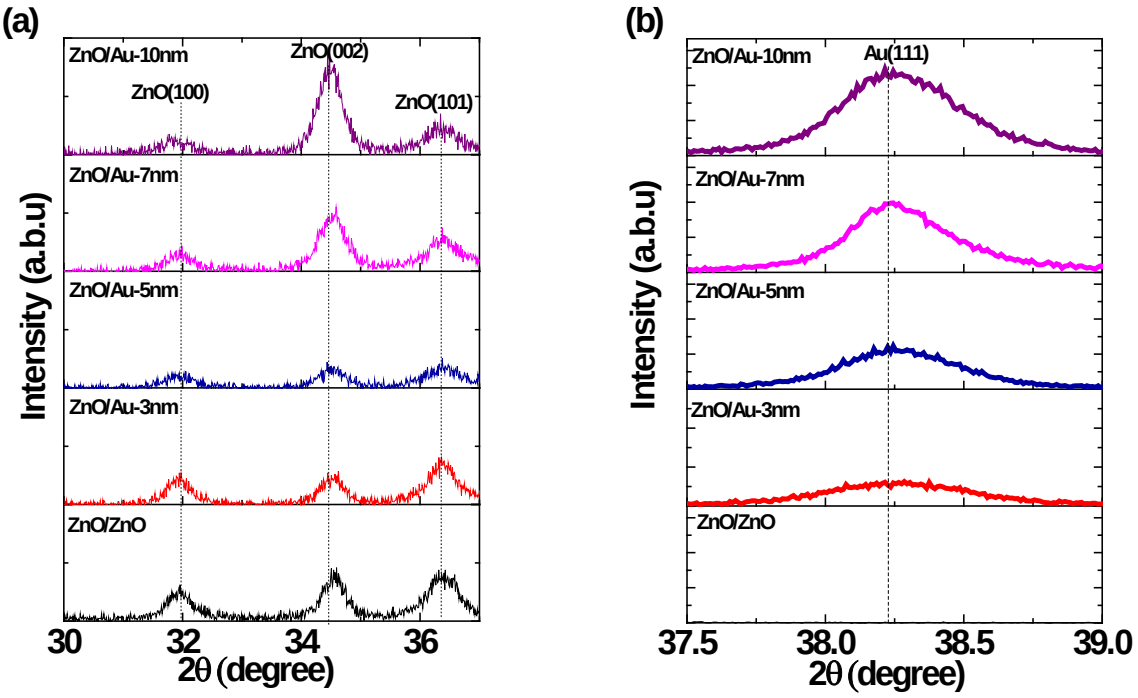

Figure 25. (a) GAXRD of Au NP-embedded ZnO films with different Au thicknesses, and (b) the intensity of preferred Au (111) diffraction peak.

The total thickness of the mixture film (ZnO/Au-5nm) was 80 nm determined by cross-sectional TEM image (**Figure 26a)**. Moreover, bright field images and backscattered electron images provided a clear evidence of the Au NPs ranging from 15 nm to 30 nm embedded in ZnO film (**Figure 26b**), which fairly agreed with the calculated size based on **Eq.22**. The elemental

distribution mapping performed by energy-dispersive spectroscopy (EDS) suggested that Au NPs were all embedded and distributed in the center of the ZnO: Au NP composite films (**Figure 26c**).

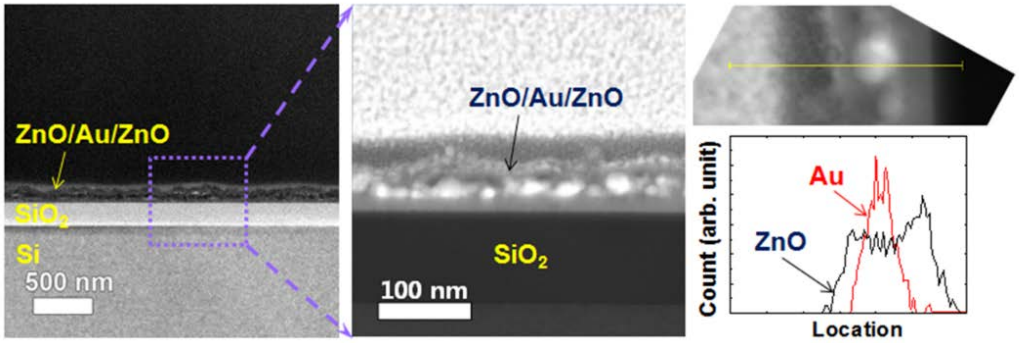

Figure 26. (a) TEM image of ZnO/Au-5nm, (b) the high-angle annular dark-field (HAADF) image of the same film showing the Au NP formation after annealing, and (c) the elemental distribution of the same film along with the yellow line measured from the EDS.

based on the information revealed by TEM images, the vol. % of Au content, and the interspace per each Au NP in each composite film were calculated and tabulated in **Table 4**. It is noted that the particle size we used in this conversion was 20 nm.

Table 4. Au content (vol. %), and the distance between Au NPs in each composite film.

Samples	Au content (vol. %)	Interspace (10^4 nm^3 per Au NP)	Center-to-Center distance (nm)
ZnO	--	--	--
ZnO/Au-3nm	3.75	11.2	48
ZnO/Au-5nm	6.25	6.70	40
ZnO/Au-7nm	8.75	4.78	36
ZnO/Au-10nm	12.5	3.35	32

2.4 ELECTRON TRANSPORT BEHAVIOR

More detailed information regarding electrical conductivity in our ZnO: AuNP mixture films was interpreted by Hall-effect measurements as function of temperature ranging from 200 K-340 K. Four representative square-shaped samples including ZnO and Au thin films as reference were mounted onto the sample holder in Van der Pawl configuration. In-Sn alloy round drops were soldered onto four corners of square sample as metallic electrodes in contact with four gold-coated probes of this measurements. A large decrease (increase) in resistivity (conductivity) of mixture films was observed (**Figure 27**). The best mixture sample in terms of electrical resistivity was down to 4×10^{-4} Ω.cm, which was about six orders of magnitude lower than the undoped ZnO control sample.

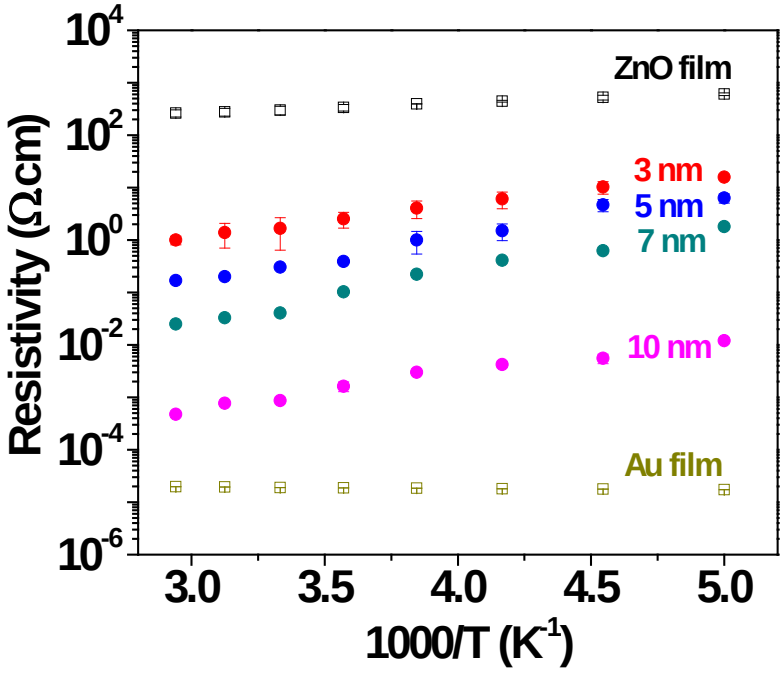

Figure 27. Temperature-dependent electrical resistivity of ZnO: Au NP mixture films.

The decrease in resistivity of our mixture films is attributed to the increase in electron concentration with the elevated temperature (**Figure 28**). By scrutinizing the Arrhenius correlation (the carrier concentration in logarithmic scale vs. 1000/T) of our mixture films compared to that of the reference samples, pure Au film and the ZnO film. There were Arrhenius slopes as function of temperature. We believe that the Schottky barrier at the Au-ZnO interface, which is determined by the work function difference between the Au and ZnO, was responsible for these Arrhenius slopes. Given that the work function of Au is 5.1 eV, slightly larger than the work function of undoped ZnO, which was reported as 4.6-4.9 eV. The Schottky barrier is possible formed at the Au-ZnO interface. Those linear relations of logarithmic carrier concentrations vs. 1000/T suggests that high electron concentrations of the Au NP-embedded ZnO films were attributed to the thermionic emission of electrons donated from Au NPs to the ZnO matrix. The magnitude of Arrhenius slopes, which stands for the Schottky barriers in those mixture films, were similar around 188 meV averagely. This observation is also consistent with the concept we hypothesized since the magnitude of Schottky barrier for electrons donated from the metal side is determined by the work function of metal and the affinity of semiconductor [37].

Given that the Au mid-layer thickness only influences the Au NP population densities instead of Au particle sizes, it also suggested that more electrons can overcome similar Schottky barriers of 188 meV at the Au-ZnO interface of mixture films, and result in a distinct increase in carrier concentration with the elevated initial thickness of Au mid-layer.

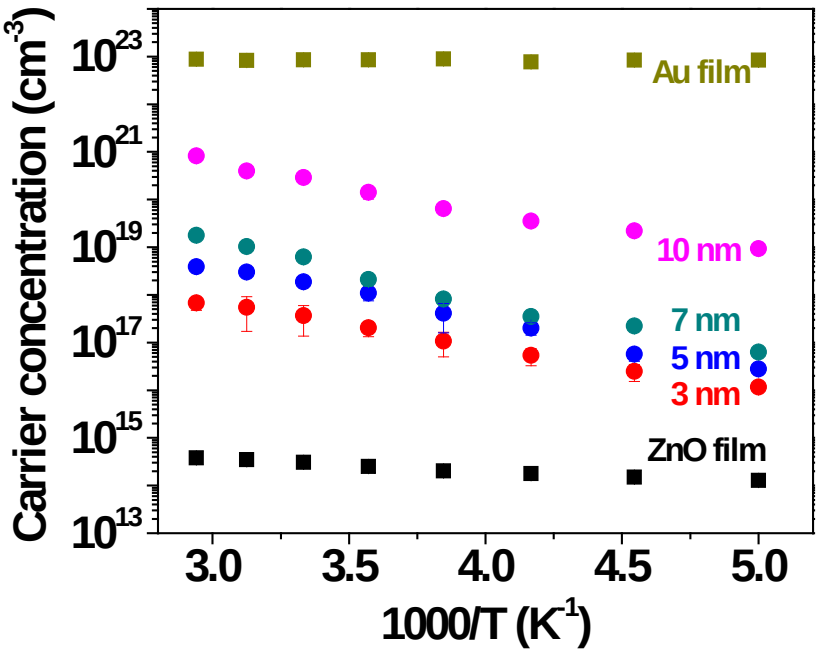

Figure 28. Temperature-dependent carrier concentration of ZnO: Au NP mixture films.

The temperature-dependent electron mobility of mixture films is shown in **Figure 29**. The mobility of ZnO/Au-10nm film is larger than that of ZnO/Au-3nm film due to the better textured structure (crystallinity) determined by the XRD. However, the slopes of mixture films were several times larger than that of the pure ZnO. Hence, it indicates the electron mobility of mixture films was significantly lower than that of the ZnO film, and their electron motion is apparently limited by another carrier scattering mechanism which has different activation energy from that of ZnO control sample. Au-ZnO interface might be responsible for the slope difference here since heterointerface could be scattering centers for composite materials reported elsewhere [47].

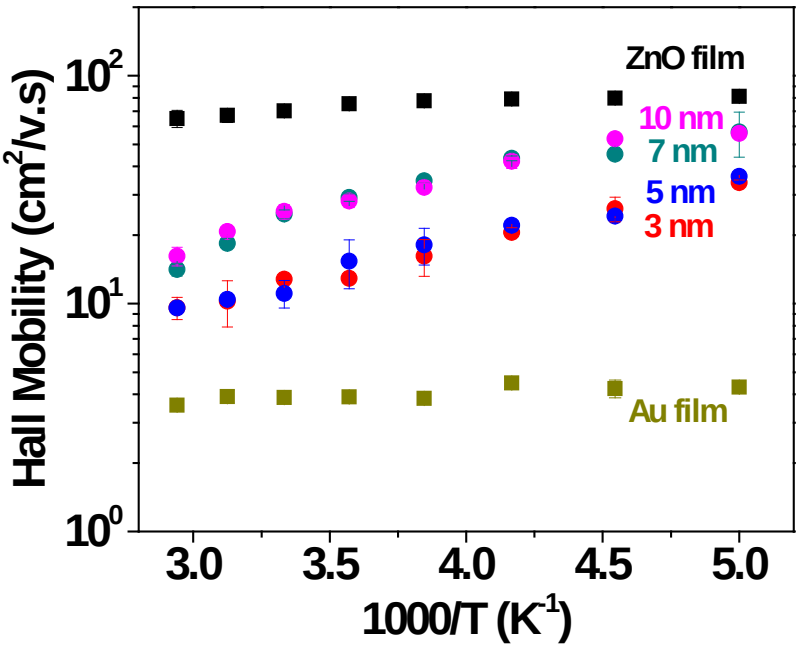

Figure 29. Temperature-dependent carrier mobility of ZnO: Au NP mixture films.

To examine the effect of Au-ZnO interface regarding this carrier scattering. The thickness of ZnO films were changed from 80 nm to 160 nm. In **Figure 30**, it showed the temperature dependence of the carrier concentration and carrier mobility of Au NP-embedded ZnO films with total thickness of 80 nm and 160 nm (denoted as ZnO-80nm and ZnO-160nm). The initial Au mid-layer thicknesses of those films were fixed to be 10 nm. It was observed that the electron mobility of the 160 nm thick film was less influenced by the temperature change in contrast with that of the 80 nm thick film. Apparently, the correlations with the temperature of these two Au NP embedded ZnO films demonstrated that the electron scattering centers were neither grain boundaries nor other intrinsic point defects originated from the ZnO lattice. Given the clue that an increase in the ZnO layer thickness (as well as the ZnO volume) actually reduces the Au-ZnO interface area per unit volume, **Figure 30** implies that the magnitude of electrons scattering in our Au NP embedded ZnO

films is relevant to the Au-ZnO interface. Overall the electron mobility of 160 nm thick ZnO/ Au-10nm film increased to 47 $cm^2/V{\cdot}s$ with a carrier concentration of 2.2×10^{20} cm^{-3} is obtained.

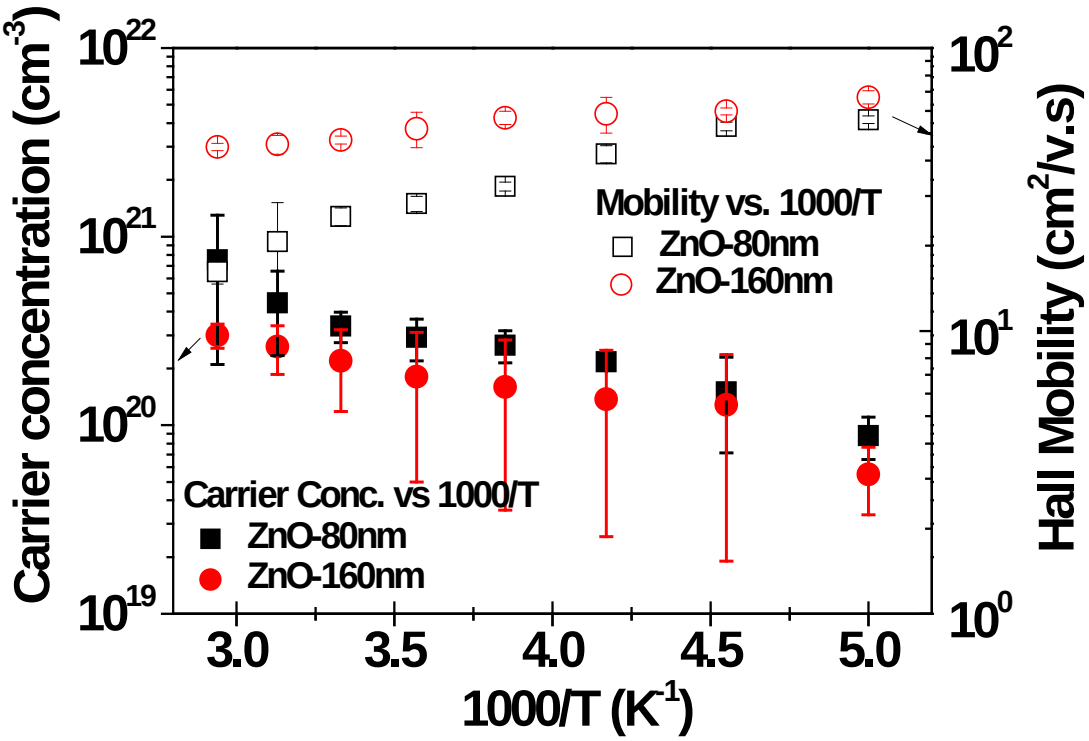

Figure 30. Temperature-dependent carrier concentration and carrier mobility of Au NP embedded ZnO films with varied ZnO layer thicknesses.

Compared to the ZnO control sample (n = 3.0×10^{14} cm^{-3}, μ= 70 $cm^2/V{\cdot}s$), the best carrier concentration of our Au NP embedded ZnO film had six orders of the magnitude larger than that of the ZnO film, but the carrier mobility of the same sample only decreased 23% from 70 $cm^2/V{\cdot}s$. The results in this study show that the carrier concentration and the mobility of such mixture films can be independently controlled without the hindrance of the ionized impurity scattering that inherently exists in highly doped ZnO films. The optical properties of our Au NP embedded ZnO film films were also measured (not shown). However, the transmittance of mixture films ranged

from 68 % to 85% in contrast of 93 % of transmittance of the ZnO control film in the visible wavelengths. We believe the low transmittance of this case was because the Au NPs embedded might have a narrow distance (~30 nm). This could lead to certain degree of coalescence between adjacent metal particles. Thus a wet chemical method was employed not only for better dispersion of metal NPs in the TCO matrix, but it offers a good controlling ability on the morphology of nanoparticle, which lead to an improved optical transparency of such mixture films. In the next chapter, we deposited our mixture films via all wet-chemistry methods including sol-gel and polyol processes, instead of the physical vapor deposition (e.g. e-beam deposition) which relies on ultrahigh vacuum apparatus, in order to develop affordable TCO mixture films by means of synthesizing uniform-sized metal nanostructures well-dispersed in the TCO matrix.

3.0 SOLUTION-PROCESSED COMPOSITE TCO FILMS

3.1 MOTIVATION

The conclusion from the previous study on those Au NP embedded ZnO films has provided the fundamental understanding that conducting electrons donated from the metal constituent exhibited thermionic emission across the Schottky barrier and transport in the ZnO matrix when the temperature is in the 200-340 K range. This caused the carrier concentration to increase with multiple times, without severely compromising the electron mobility. This enhancement is attributed to the synergy between the metal NPs (Au) and the undoped semiconductor matrix (ZnO). This hypothesis brought us another interesting topic: whether or not it is possible to reduce the Schottky barrier at the metal-semiconductor interface by choosing an appropriate metal with a work function lower than gold. This may facilitate the electron donation, which strongly relies on the Schottky barrier at the metal-ZnO interface. Given that the work function of gold (ϕ_{Au}) is 5.1 eV and ϕ_{ZnO} ranges from 4.6 to 4.9 eV. A Schottky barrier with the magnitude of 200-500 meV would be expected at the Au-ZnO interface. Since Au is considered a metal that has relatively high work function, we suspect that a reduced Schottky barrier, and an effective electron donation can be expected if an alternative metal with a lower work function (e.g., Ag and Cu) is chosen.

In addition to the work function difference, the research in this chapter shows results from the mixture films fabricated via solution method. The solution method has strengths of large-area

coatings and low maintenance. On top of that, several monometallic or alloy nanoparticles with different sizes and shapes controlled via the solution-based method have been extensively studied. In the present study, the particle size and shape are well-controlled in the solution method. Hence, the ZnO-based films (AZO and ZnO) mixed with Ag NPs derived by wet chemistry are discussed, and their electrical and optical properties are investigated.

3.2 EXPERIMENTAL AND APPARATUS

3.2.1 Synthesis of Ag Nanoparticles

The silver nitrate ($AgNO_3$, 99.9999 %) was dissolved in the deionized water with a resistance of 18.3 MΩ. Since Ag NPs were easily agglomerated, researchers commonly added a long-chain surfactant such as PVP or PVA to inhabit undesired Ag agglomeration [48]. Instead, cellulose fibers serving as solid templates were introduced to mediate the chemical reduction of Ag ions on the template surface. The surface of cellulose fibers contains plenty of hydroxyl groups (-OH) that are likely anchor metal species. As a result, the tendency of the agglomeration was effectively inhibited [49-52]. In addition, preparing Ag NPs by this method does not require washing away the surfactants attached on the metal surface, and the consistency of the Ag NP content could remain since the cleaning procedure causes a reduction of yield.

This unique Ag NP synthesis follows: A piece of cellulose fiber with a certain size soaked in this $AgNO_3$ aqueous solution for 10 min. This fabric piece was later gently soaked in the dilute sodium borohydride aqueous solution ($NaBH_4$, 98 %), which served as a reducing agent. The color of this Ag colloid immediately turned to citrus orange. By repeating this soaking process several

times, several Ag colloidal solutions with varied Ag molar concentration were obtained (**Figure 31)**. Then Ag NPs were centrifuged at 12,000 rpm for 20 min, and re-dispersed in a small amount of ethanol.

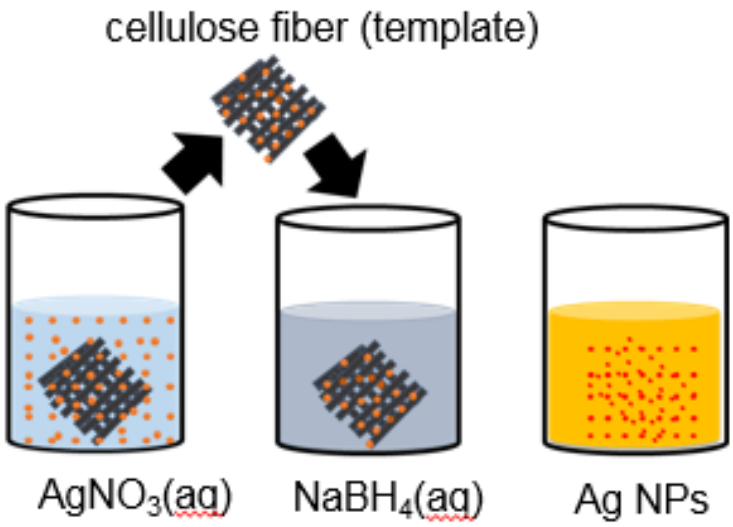

Figure 31. Illustration of the Ag NP synthesis with assistance of cellulose fibers.

TEM characterization (2000-CX, JEOL) was applied to investigate the morphology of the synthesized Ag NPs. The TEM image confirmed the presence of Ag NPs, and the Ag NP size was estimated around 21 ± 8.0 nm based on the TEM image analysis (**Figure 32a-b**). In addition, the size distributions of colloids with varied Ag contents measured by DLS (LB550, Horiba) indicated the Ag NPs ranged from 5-30 nm with a center of 15 nm (**Figure 32c**), regardless of Ag contents. More importantly, the size distributions interpreted by DLS is in good agreement with the particle size estimated from the TEM image.

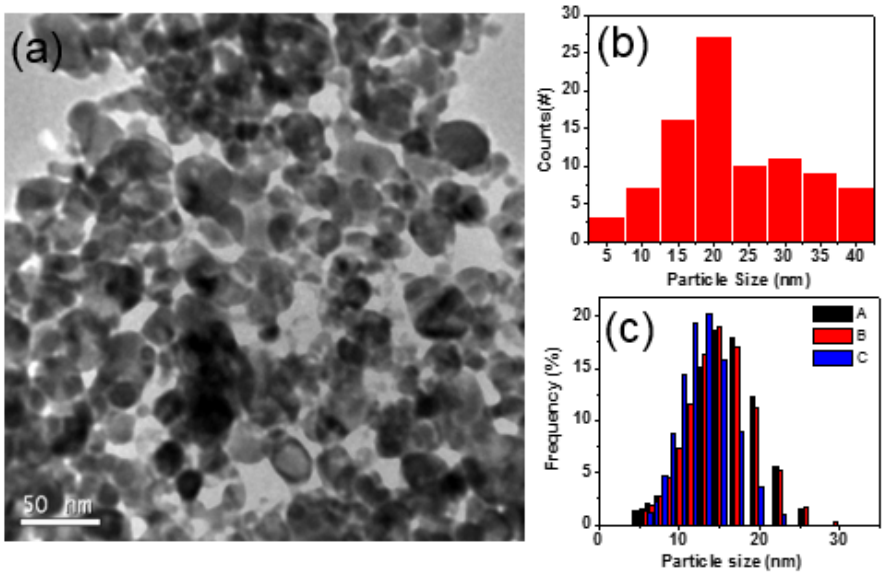

Figure 32. (a) TEM image of synthesized Ag NPs, and (b) Size distribution of the Ag NPs based on the TEM image. (c) Size distributions of colloidal solutions with varied Ag contents via DLS.

Those re-dispersed Ag NP alcoholic colloids mixed with the AZO (Al dopant at 1.0 at. %) or ZnO sol-gel resulted in several mixture solutions with varied Ag contents. The choice of AZO here is because the carrier concentration (resistivity) of AZO can be consistently controlled by the Al doping level in contrast with that of ZnO film, which is more susceptible to the environment. Mixture solutions were spin-coated at a rate of 3000 rpm on glass substrates repeatedly until the desired thickness was achieved. The thickness is approximately 200 nm (**Figure 33**) observed in cross-section SEM (FEI XL-30, Philips) and confirmed by fitting the simulated model with optical parameters obtained from the spectroscopic ellipsometry (Unisel Ellipsometer, Horiba). The film thickness is strongly dependent on the spin-coating parameters such as the viscosity of the solution, the mechanical force derived from the spinner, and the spinning time. As such, the film thickness should not show noticeable discrepancy among our samples as long as parameters mentioned above were not altered much. All of our glass substrates were sonicated in acetone/ethanol for 10 minutes, and were air-dried in the fume hood prior to the spin-coating procedure.

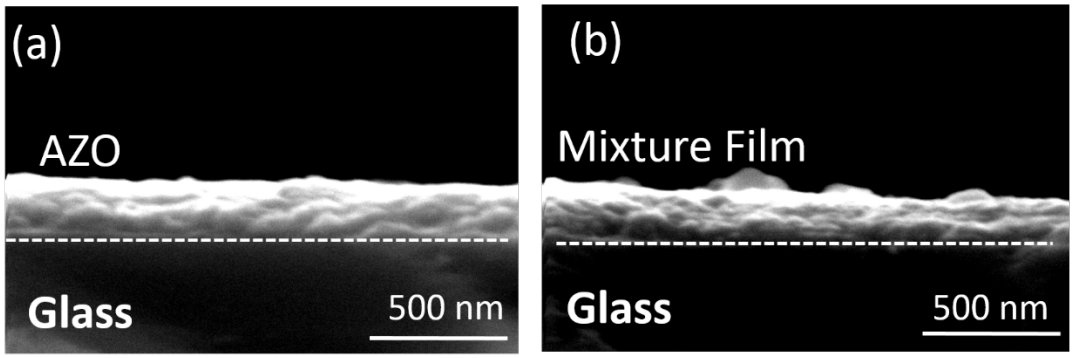

Figure 33. The thicknesses of (a) AZO film and (b) AZO: Ag NP mixture film obtained from the cross-sectional SEM images. The thicknesses were about 200 nm.

3.2.2 X-ray Photoelectron Spectroscopy

X-ray photoelectron spectroscopy (XPS) is one of the surface spectroscopic techniques. The XPS analysis can provide both qualitative and quantitative information on all elements presented in the periodic table (except hydrogen and helium). Thus XPS is also called Electron spectroscopy for chemical analysis (ESCA). The physics of XPS analysis is based on the photoemission. When X-ray irradiation strikes the specimen in ultra-high vacuum environments, the irradiated photons promote core-level electrons to overcome the binding energy (B.E.) and escape from the surface into the vacuum level (**Figure 34**) [53].

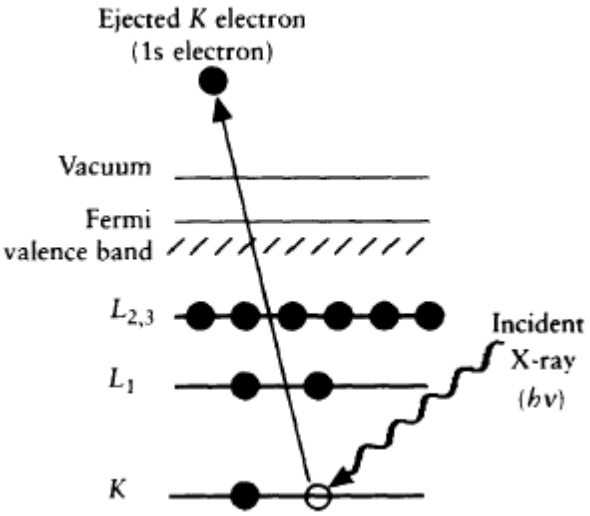

Figure 34. Schematic of the photoemission process.

The binding energy of those photoelectrons is associated to the atoms where they are originated. The relation is described via the Einstein equation (**Eq.23**).

$$B.E. = h\nu - KE \qquad \textbf{(Eq.23)}$$

where B.E. stands for the binding energy of the electron in the atom, which is considered as a fingerprint for a specific atom. hν is the energy of X-ray source (Al Kα=1486.6 eV), and KE is the kinetic energy of the emitted photoelectrons that is measured by an energy analyzer installed in the XPS instrument. Since hν is known, and KE is measured, E_B, the quantity normally expressed in electron volt (eV), which stands for the identity of the photoemitting atom, can be easily obtained. It is noted that the inelastic mean free path (IMFP, λ_e) of photoelectrons is only 0.2-3.0 nm, depending on their kinetic energy. About 95 % of XPS signals are contributed from the depth of $3\lambda_e$. That is, although x-ray can penetrate a depth of 1 μm, photoelectrons can only penetrate about a maximum of 10 nm. Thus XPS analysis is considered a very surface-sensitive instrument.

The chemical shift (ΔE_B) is an important feature of XPS analysis. All elements in the periodic table have a chemical shift depending on their chemical states. For example, C-O bonding

exhibits a chemical shift of 1.4 eV but C=O or O-C-O has a chemical shift of 2.9 eV in the C 1s spectrum [53]. Therefore chemical shifts can provide strong information showing the emitting atom is in the reduced state or its oxidized states. By fitting those XPS peaks correctly, the amount of atoms and their chemical states can be quantitatively estimated due to the fact that the number of those photoelectrons is strongly related to the concentration of the emitting atom in the sample.

3.2.3 Conductive Atomic Force Microscopy

Conductive AFM (c-AFM) is a derivative of traditional atomic force microscopy (AFM). By applying a DC bias between the conductive tip and the sample while the tip is scanned in contact with sample surface (contact mode), raw current signals can be collected and analyzed by a signal-to-current convertor in the electric circuit. As a result, a topographic image and its corresponding current image can be generated simultaneously for the same area (**Figure 35**). By comparing two images, local conductive domains at nanoscale can be visually observed by the c-AFM technique even though those conductive domains have the same heights from the sea level which cannot observe the difference in the regular AFM images. For instance, c-AFM measurements on polycrystalline thin films have been applied to distinguish the difference in terms of conductivity between grain boundaries and the interior of the grains [54]. The AFM images are all graphically processed in Gwyddion [55], which is a professional graphic software designed for interpreting AFM images including values of root mean squares (RMS) in heights, which represent the levels of surface roughness of the coatings.

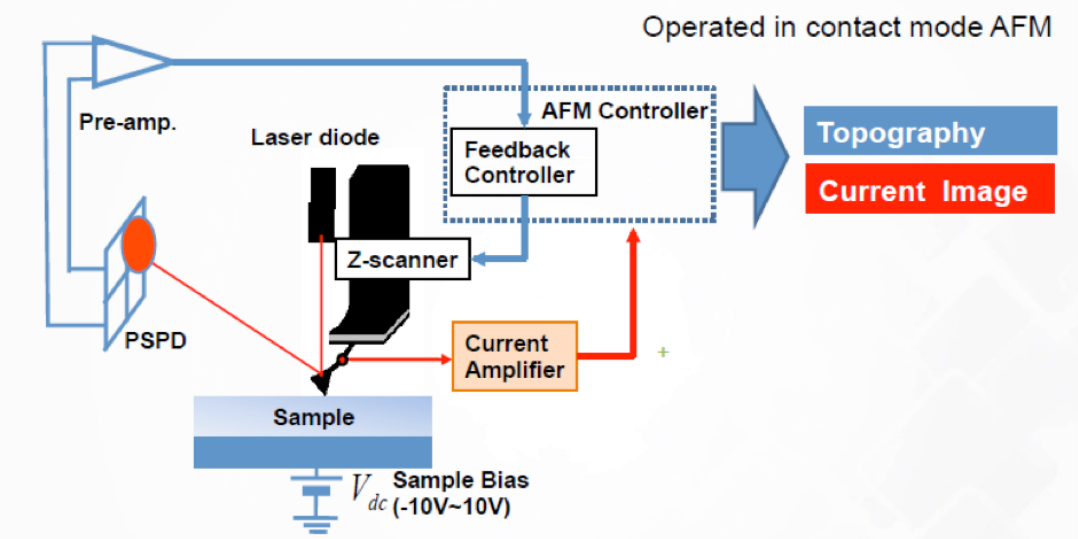

Figure 35. Schematic diagram showing the configuration of Conductive AFM.

3.2.4 Spectroscopic Ellipsometry

Spectroscopic ellipsometry (SE) is a non-destructive and surface-sensitive instrument that is used to obtain the refractive index (n, k) and determine the film thickness (d). In ellipsometry, an un-polarized radiation with a specific wavelength (λ) is polarized by a polarizer into s-polarized and p-polarized beams. Those polarized beams hit the sample that consists of a thin film of interest (refractive index=n_1) and a substrate (refractive index=n_2) at a defined angle, which is customarily set in the vicinity of the Brewster angle because ellipsometry has the best sensitivity to film parameters at this angle. While two polarized lights travel in two media (n_1 and n_2) at varied incident angles, the amplitudes of reflected s- and p-polarizations ($\boldsymbol{r_s}, \boldsymbol{r_p}$) are subject to have changes accompanying with phase shifts in both polarizations (δ_s, δ_p) accordingly. Measurement results are expressed in terms of the ellipsometry parameters:

$$\frac{\boldsymbol{r_p}}{\boldsymbol{r_s}} = tan\varphi e^{i\Delta} \qquad \textbf{(Eq.24)}$$

where $\boldsymbol{r_s}$ and $\boldsymbol{r_p}$ are the complex reflection coefficients for the s-polarized and p-polarized lights, $tan\varphi$ is the ratio of magnitudes of two reflected polarized lights, and Δ is the difference between two phase changes (δ_p-δ_s). Since $tan\varphi$ and Δ are two important parameters that are measureable, and are functions of d (unknown), n_1, n_2, θ and λ based on Fresnel equations, the film thickness (d) can be determined by a series of model-fittings.

3.2.5 Dynamic Light Scattering

The dynamic light scattering (DLS) shinning a monochromatic laser beam onto a solution with spherical particles. Then DLS detects the random thermal motion of particles in the solution known as the Brownian motion, which is a strong function of the particle size, the viscosity of the medium, and the temperature. To be more specific, the correlation associated with the speed of motion of the nanoparticles (or diffusivity) and the nanoparticle size are described via Stokes-Einstein relation.

$$D_h = \frac{kT}{6\pi D\eta} \tag{25}$$

where D is the diffusion coefficient strongly associated with the velocity of Brownian motion, k is the Boltzmann constant, T is the temperature, η is the viscosity of the solution, and D_h is the called hydrodynamic radius of the particle. It is noted that the DLS measures the hydrodynamic radius, and it is possible to compute the diameter of spherical particles and their size distribution which theoretically diffuse in the same way as real particles do in the same viscous media in this investigation., the motion of particles is definitely affected Once a dipole layer or long-chain stabilizers bound to the surface of particles [56]. As a result, the hydrodynamic radius measured from DLS tends to be exaggerated than the primary particle size visually observed in SEM or TEM

(**Figure 36**). Despite that, there are some advantages to using the DLS method, which are: (1) non-destructive measurement (2) short experimental duration (3) a small quantity of samples required (4) good technique that detects trace amount of aggregates.

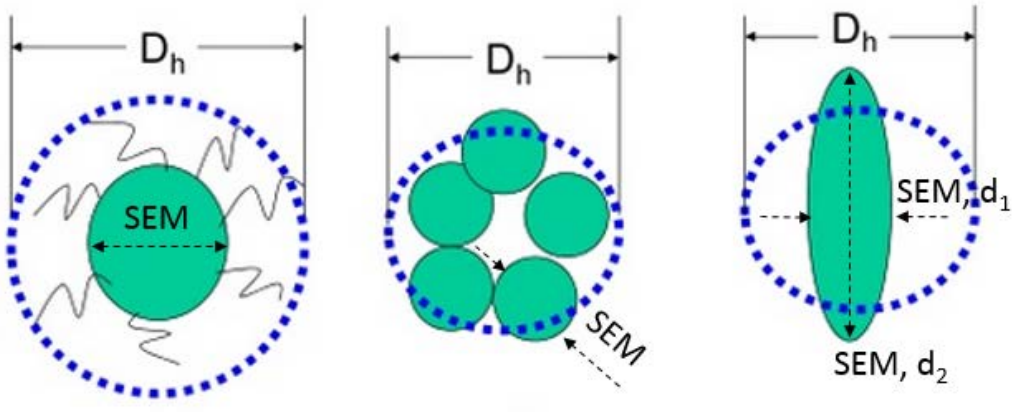

Figure 36. Explanation of hydrodynamic particle size measured by DLS and the real particle size determined by the SEM.

3.3 AZO: SILVER NANOPARTICLE MIXTURE FILMS

The electronic states of Ag NPs embedded in the AZO matrix were examined by the XPS (ESCALAB 250Xi, Thermo Scientific) shown in **Figure 37a-b**. An Argon-sputtering with a voltage of 1000 eV was applied for 10 sec in order to remove undesired native oxide or humidity attached on the sample surface. Given that the standard binding energy (B.E.) of Ag^0 $3d_{5/2}$ centered at 368.2 eV, and that of AgO $3d_{5/2}$ centered at 367.6 eV, the B.E. of the Ag $3d_{5/2}$ photoemission peaks in AZO: Ag NP mixture films are all centered at 368.04 eV corrected by the C 1s at 284.6 eV as the internal reference. The value of this B.E. can be referred to the metallic state of Ag,

which indicates that embedded Ag NPs were well-protected by the oxide matrix, and there were no noticeable B.E. shifts, which are associated with Ag-O bonding after the annealing treatment.

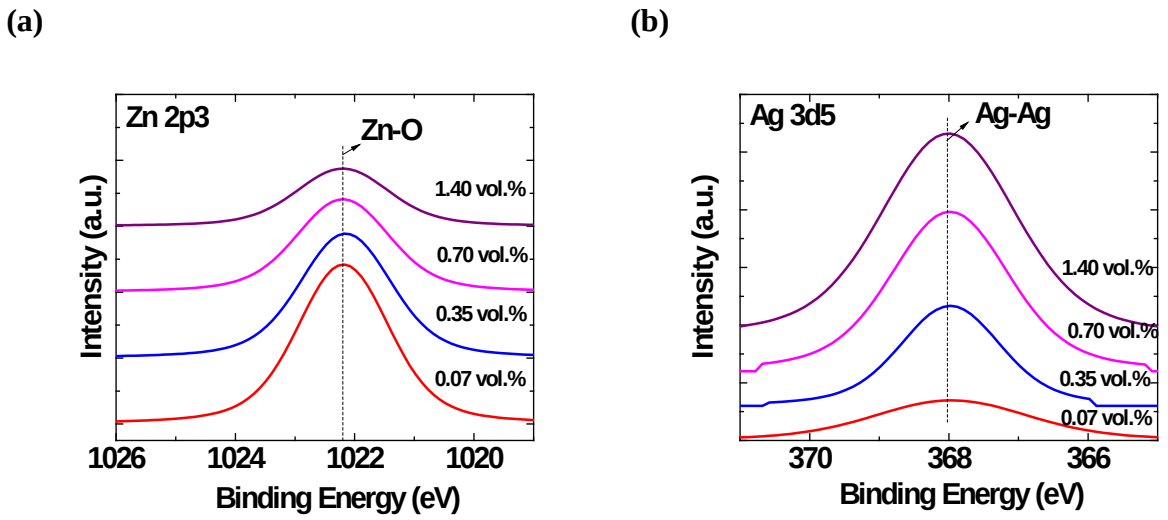

Figure 37. XPS analysis for (a) Zn $2p_{3/2}$, and (b) Ag $3d_{5/2}$ of the AZO: Ag NP mixture films.

In addition, quantitative analysis by the electron probe micro-analyzer (EPMA) for the Ag contents (Ag to Zn atomic ratios) in the mixture films showed a fair consistency with the chemical composition analysis achieved by XPS, which are all tabulated in **Table 5**. The small discrepancy in the interpretation about Ag to Zn ratios between two analytical instruments is owing to the fact that photoelectrons collected by XPS are from very shallow surface (~10 nm), but the EPMA collects signals from the entire films. This fair consistency via both instruments regarding Ag contents implies that the Ag NPs were well-dispersed in the AZO matrix. Atomic ratios (at. %) directly obtained from XPS and EPMA were all converted into the volume ratios (vol. %) for our convenience since the vol. % of the minor phase with respect to the major phase is more commonly used in composite materials.

Table 5. Quantitative analysis by EPMA and XPS for the for Ag contents in mixture films.

Samples	Ag/Zn by EPMA (at. %)	Ag/Zn by XPS (at. %)	Converted Vol.% (EPMA/XPS)
#1 (AZO)	--	--	--
#2	0.1	0.14	0.07/0.10
#3	0.5	0.37	0.35/0.26
#4	1.2	0.68	0.70/0.48
#5	2.2	1.46	1.40/1.03

The morphologies of the mixture films obtained by the AFM (Dimension 3100, Vecco) are shown in **Figure 38**. The surface roughness of the mixture films observed did not show significant difference from that of AZO control sample. The average root mean square (RMS) of the vertical heights in the mixture films was only about 5.6 ±2.1 nm. This indicates the addition of tiny amounts of 15-20 nm Ag NPs did not destroy the surface flatness of the mixture films significantly, which is positive for obtaining a good optical transparency (less diffuse scattering) for each sample.

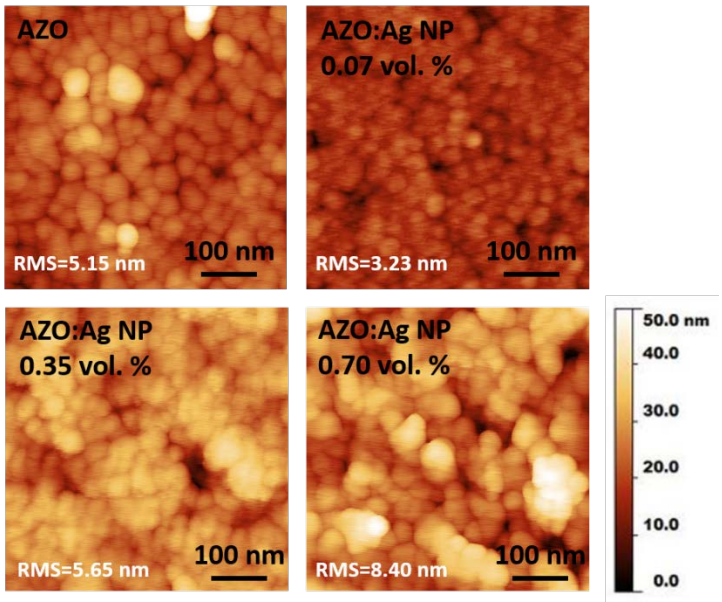

Figure 38. The AFM images reveal the surface morphologies of AZO: Ag NP mixture films.

The crystal structures of AZO: Ag NP mixture films were characterized in XRD θ-2θ scan (X'Pert, PaNalytical) with Co-Kα radiation of λ=0.179 nm in the 2θ range from 30° to 70°. All samples exhibited wurtzite hexagonal structure (JCPDS 36-1451) with a preferred ZnO (002) orientation, shown in **Figure 39**. Ag diffraction peaks at 2θ=44.57° and 51.90° corresponding to face-centered cubic (FCC) Ag (111) and (200) were barely observed due to the inherent limitation of θ-2θ scan for such small amounts of Ag constituents embedded. In addition, similar intensities or full-width half maximums (FWHMs) of ZnO (002) peaks in all mixture films indicate that the crystallinity of the AZO matrix, invariant to the amount of Ag NPs embedded, remain as the same as that of the AZO control sample.

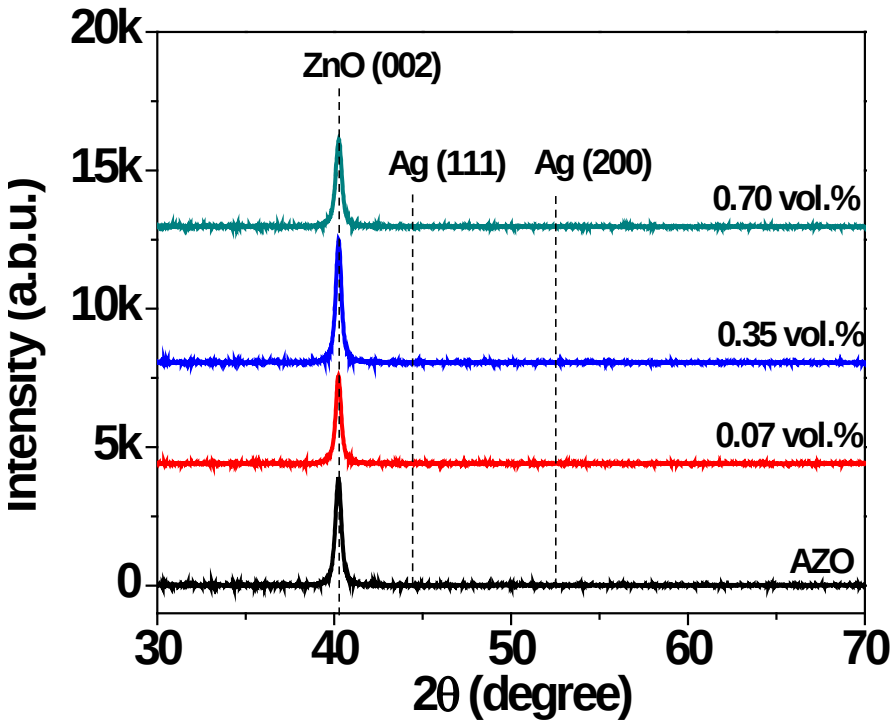

Figure 39. Crystal structures of the AZO: Ag NP mixture films characterized by θ-2θ scan XRD.

3.4 ELECTRON DONATING BY A LOW WORK-FUNCTION METAL

Electrical properties in details were obtained by the temperature-dependent Hall-effect measurements. The temperature was elevated from 200 K to 340 K (-73 ℃ to 68 ℃) with an interval of 10 K. It is noted that an Ag film (20 nm) was included in order to compare physics of the mixture films to the metal film. In **Figure 40 ,** the carrier concentration of the Ag film is independent of the temperature as is expected since its valance band and conduction band are overlapped. In comparison, the carrier concentration of AZO film exhibited a linear correlation with an activation energy of 20 meV in response to the temperature change, which indicates those electrons in AZO film is due to a thermal excitation from donor states to the conduction band of AZO. It is consensual that Al-substitutes (Al_{Zn} /Al_{Zn}^{+}) are responsible for the conducting carriers in the AZO case. In addition, the Al_{Zn}^{+} has the lowest donor energy level of 13 meV below the conduction band of AZO reported [57], which is conceptually consistent with our observation.

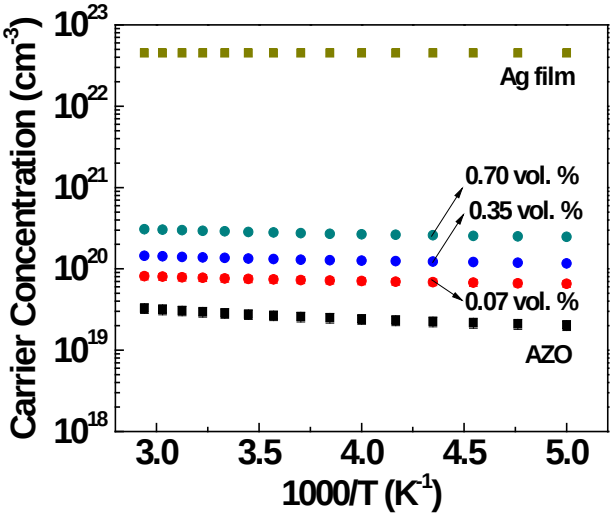

Figure 40. Temperature-dependent carrier concentrations of AZO: Ag NP films.

In contrast, the carrier concentrations of the AZO: Ag NP mixture films exhibited some temperature dependency. The degree of this dependency is between that of Ag and AZO films. The Arrhenius correlation indicates that the activation energies of the mixture films were around 10 meV. To recall the results of the previous research [58], the activation energy of the carrier concentration can be attributed to the Schottky barrier at metal-oxide interface. The magnitude of this Schottky barrier on the metal side is governed by the difference of metal work function ($\emptyset_m$) and the affinity of oxide semiconductor (χ). The band structure of this Schottky barrier formed at the metal-oxide interface is illustrated in **Figure 41**.

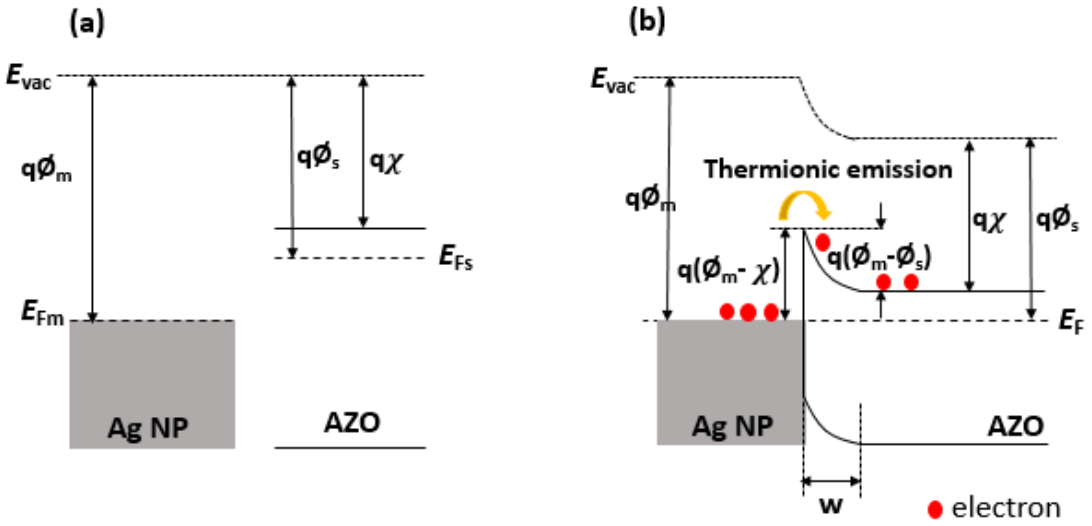

Figure 41. (a) Ag NP and AZO band diagrams before contact, and (b) the equilibrium band diagram and the Schottky barrier formed at the junction after Ag NP and AZO are brought in contact.

Given that the reported work function of AZO films ranges from 3.7 to 4.6 eV, and the work function of Ag NPs is 4.54 to 4.59 eV (corrected by **Eq.26** since bulk $\emptyset_{Ag}$=4.50 eV), the magnitude of the Schottky barrier that is governed by $\emptyset_{Ag}$ and χ on the Ag side can be effectively minimized, and this is interpreted by the negligible temperature dependence, which is 10 meV. Additionally, the slight increments in the carrier concentration of the mixture films with elevated

Ag contents accordingly, in the entire temperature range can be attributed to the enlargement of total Ag-AZO interface area.

The hypothesis that electrons donated from Ag NPs to the AZO matrix mainly transport in the AZO matrix is supported by the carrier (electron) mobility as function of temperature shown in **Figure 42**. All samples exhibited electron mobility around 10 to 20 $cm^2/V.s$. More importantly, the Arrhenius correlation (the logarithmic Hall mobility vs. 1000/T) of AZO: Ag NP mixture films have a linear relation in this temperature region (200 K to 340 K), and have similar Arrhenius slopes with that of AZO sample. Therefore, the evidence indicates that the transport manner of those electrons donated from Ag NPs are limited by the ZnO GB-scattering, which is described in **Eq.7** for polycrystalline TCO films.

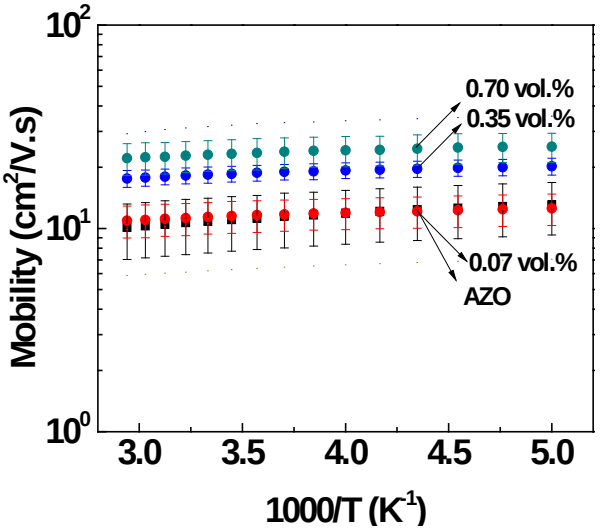

Figure 42. Temperature-dependent Hall mobilities of AZO: Ag NP films.

Overall, the current results regarding the carrier concentration, and the Hall mobility as a function of temperature in AZO: Ag NP mixture films indicate that the carrier concentration and the carrier mobility in the mixture films can be enhanced by Ag NPs in the AZO matrix. Electrons

can be donated from Ag NP and further transport in the AZO matrix. The lowest resistivity obtained was 9.5×10^{-4} Ω.cm at room temperature, more than one order of magnitude lower than that of 2×10^{-2} Ω.cm in the AZO sample when the 0.7 vol. % of the Ag content was embedded **(Figure 43**).

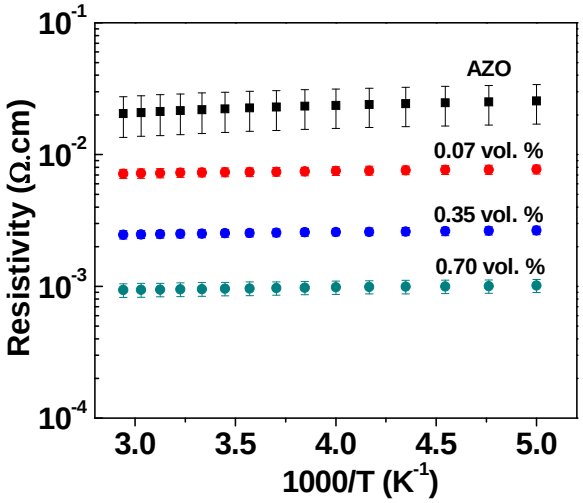

Figure 43. Temperature-dependent Hall resistivity of AZO: Ag NP films.

This Hall-effect resistivity is consistent with the resistivity measured by the traditional four point probe method tabulated in **Table 6**, given the thicknesses of mixture films are all 200 nm.

Table 6. Resistivity of AZO: Ag NP mixture films.

Samples (vol. %)	Sheet Resistance (10^2 Ω/□)	Resistivity (Ω.cm)
AZO	9.32	1.85×10^{-2}
0.07	4.31	8.62×10^{-3}
0.35	1.36	2.72×10^{-3}
0.70	0.48	9.60×10^{-4}
1.40	0.30	6.00×10^{-4}

The optical transmittance spectra as a function of wavelengths for the AZO: Ag NP mixture films are shown in **Figure 44a**. Each mixture film exhibited optical transmittance nearly 80 % in the entire visible wavelengths, and 87 % or above at the wavelength of 550 nm. As the Ag content was tentatively added to 1.40 vol. % (not shown), the optical transmittance decreased down to 78 % at the wavelength of 550 nm despite that the resistivity (sheet resistance) decreased down to 6×10^{-4} Ω.cm (~30 Ω/□).

Since the electrical conductivity and optical transparency of transparent conductors (TCs) are mutually exclusive, researchers often compare those TC films by using figures of merit (FOM) to represent the criteria for the quality of TCs. Since numerical FOMs can be represented in several ways based on different physical assumptions [59], it is more straightforward to plot the sheet resistance (R_{sh}) and the transmittance at λ=550 nm (T_{550}) as the x-axis and y-axis respectively. It is noted that any coordinates (R_{sh} , T_{550}) that are located in the upper-left corner of **Figure 44b**, represents highly qualified TCOs as they possesses the low resistance and the high transmittance. The R_{sh} and T_{550} of AZO: Ag NP mixture films, along with reported references of Ag NWs, CNTs and graphene [60], are shown in **Figure 44**, It seems the mixture films in this investigation had a tendency to lie in the upper-left corner. However, the optical transmittance had a sharp drop when Ag content was above 0.70 vol. %.

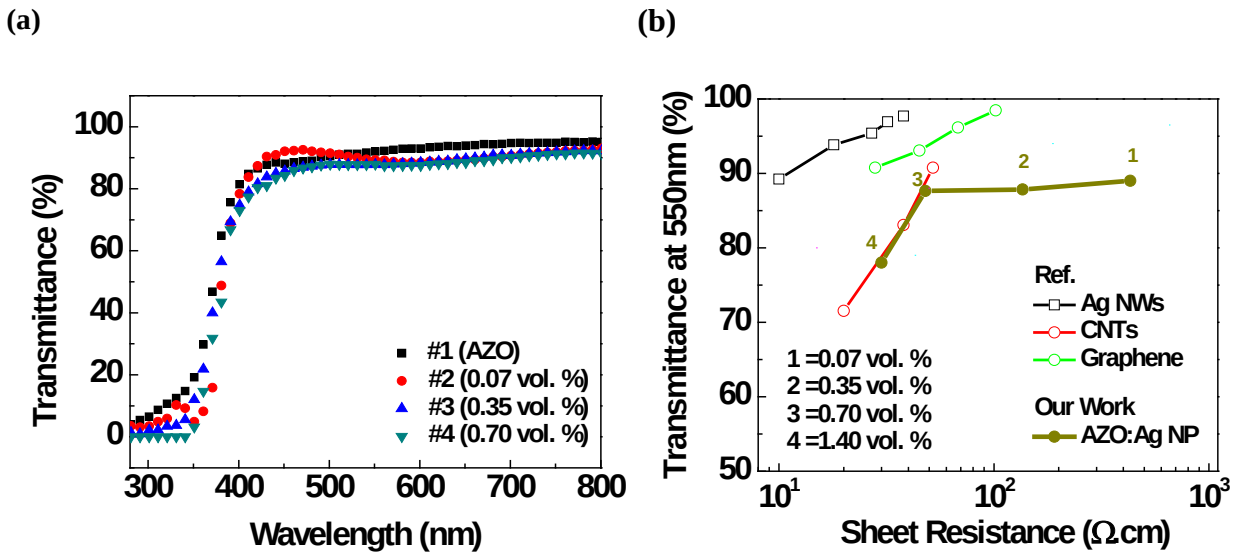

Figure 44. (a) Transmittance of AZO: Ag NP mixture films, and (b) the T_{550} vs. R_{sh} diagram.

To visually investigate the presence of Ag NPs embedded in this AZO matrix, c-AFM (Multiview 1000^{TM}, Nanonics) equipped with Au-coated conductive AFM probe was employed. Owing to the fact that the c-AFM technique simultaneously collects topographic and local current profiles at the same area while a DC bias is applied, it offers a good ability to distinguish different conducting domains in the sample with a resolution of nanometers.

In **Figure 45**, no significant local current was collected in the AZO film regardless of the magnitude of the DC bias. In contrast, the sample with 0.35 vol. % of Ag NPs exhibited different conducting domains represented as the color variation while a DC bias of 2.0 V was applied. It is believed that small dots represented in the white color refers to the most conductive domain where those Ag NPs are embedded, and the electrons on the metal surface are directly collected by the conductive AFM probe. The highest local currents (white dots) originated by the electrons donated from Ag NPs range from 40 to 50 pA in comparison to the background current, which is less than 10 pA generated by the Al_{Zn}/Al_{Zn}^{+} doping reaction in the AZO film. In addition, the percolation

threshold that attributes the percolated conductivity, was not achieved in this sample since this image was clearly observed discrete conductive paths within 500 nm × 500 nm scanning area.

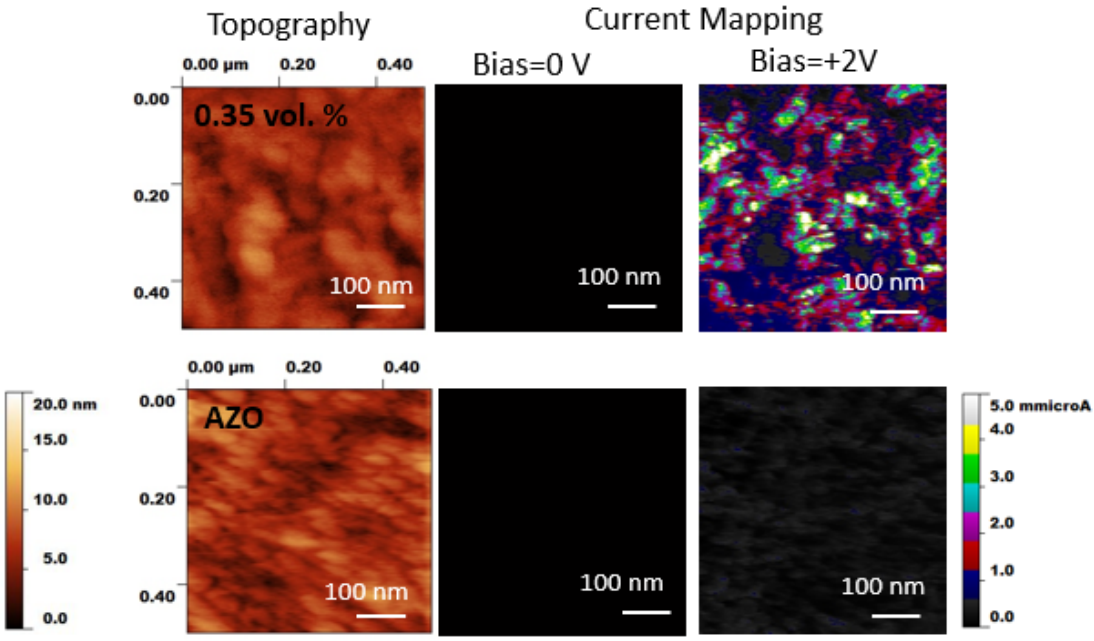

Figure 45. Topographic images and current mappings of the AZO: Ag NP mixture films.

3.5 LOW WORK FUNCTION METAL-OXIDE COMPOSITE FILMS

3.5.1 Carrier Transport in Ag NP Embedded ZnO and AZO Films.

In order to scrutinize how electrical properties of ZnO-based TCO films are enhanced by Ag NPs in details, the same amounts (vol. %) of Ag NP embedded in an unintentionally-doped ZnO matrix are also prepared for this detailed investigation. The reciprocal of total mobility (μ_T) in the mixture films can be expressed as the summation of each resistance originated from the respective scattering factor (**Eq.10**). For ZnO: Ag NP films, it is understandable that total mobility

should be correlated with ZnO grain boundaries (GBs), unintentionally impurities (e.g. $H_i^{\bullet}$ from N_2/H_2 ambience), and the ZnO-Ag interface. The correlation can be described as below:

$$\frac{1}{\mu_T} = \frac{1}{\mu_{GB}} + \frac{1}{\mu_{\mathrm{Hi}}} \qquad \textbf{(Eq.27)}$$

unlike the previous case of Au-ZnO composite systems, the Ag-ZnO interface scattering should not be significant since the energetic barrier is negligible. The scattering effect by charged impurities ($1/\mu_{\mathrm{Hi}}$) was deduced by subtracting the effect of ZnO GB-scattering ($1/\mu_{GB}$) from the reciprocal of the total mobility ($1/\mu_T$).

Similarly, scattering centers in each Ag-AZO film could be attributed to ZnO GBs, charged impurities ($Al_{Zn}^{\bullet}$) as well (**Eq.28**). This μ_{AlZn} assoication with charged particles can be deduced since the total mobility is measurable from the Hall-effect as well as the effect of GB-scattering from the ZnO film.

$$\frac{1}{\mu_T} = \frac{1}{\mu_{GB}} + \frac{1}{\mu_{AlZn}} \qquad \textbf{(Eq.28)}$$

Since the mobility associated with ionized impurity scattering is proportional to $T^{3/2}$ in the case of a non-degenerate TCO film [19], a tentative plot of the μ_{Hi} and μ_{AlZn} as a function of $T^{3/2}$ shown in shown in **Figure 46a-b.** The component mobility (μ_{AlZn}) in AZO: Ag NP mixture films increased with the elevated Ag content (**Figure 46a)**. The reason behind this phenomena is because electrons donated from Ag NPs in the sample with high Ag content (0.70 vol. %) could coordinate those Al_{Zn}^{+} impurities contained in the AZO matrix. As a result, the charged impurity scattering driven by the electrostatic force was nullified. However, the sample with low Ag content (0.07 vol. %) was another scenario. It exhibited the lowest μ_{AlZn} compared to other mixture films. This suggests that donated electrons were not sufficient to nullify the electrostatic force generated by all Al_{Zn}^{+} impurities.

The component mobility (μ_{Hi}) associated with $H_i^{\bullet}$ in ZnO: Ag NP mixture films are shown in **Figure 46b**. The sample with highest Ag content (0.70 vol. %), however, exhibited the lowest mobility. To explain this behavior, excessive electrons donated from Ag NPs might immobilize the charged particles ($H_i^{\bullet}$). As a consequence, this leads to a substantial overlapping of electrostatic fields generated by those stationary $H_i^{\bullet}$. On the other hand, the sample with lowest Ag content (0.07 vol. %) did not have sufficient electrons to cage those highly mobile $H_i^{\bullet}$. As a result, the electron motion of this sample was less affected by $H_i^{\bullet}$ since they cannot provide a consistent overlapping of the electrostatic field that deflects conducting electrons.

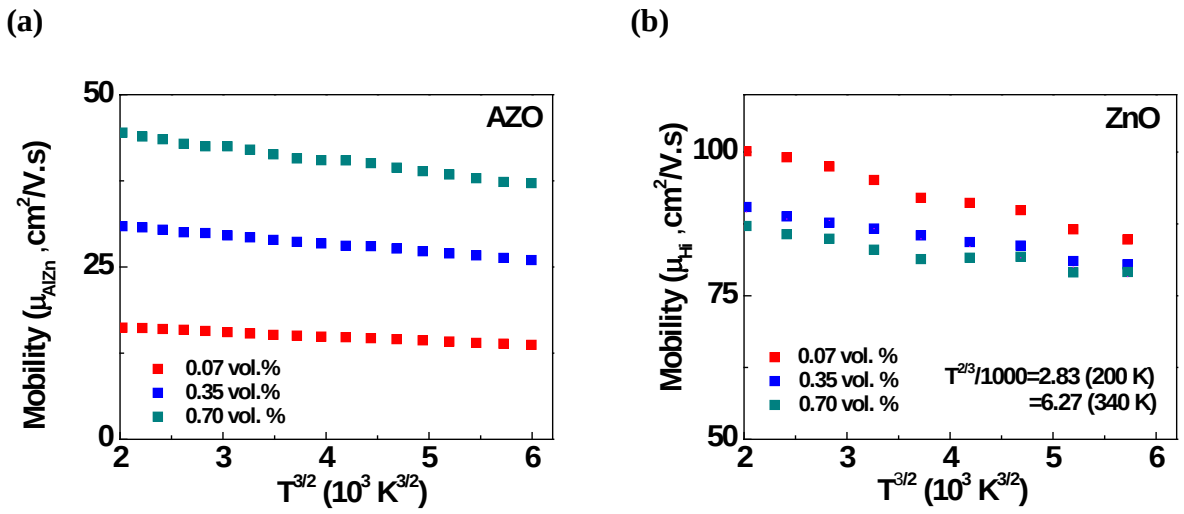

Figure 46. (a) The component mobility (μ_{AlZn}) as function of $T^{3/2}$ in the case of AZO: Ag NP films, and (b) the component mobility (μ_{Hi}) as function of $T^{3/2}$ in the case of ZnO: Ag NP films.

Although AZO: Ag NP mixture films provided better conductivity as compared to that of ZnO: Ag NP ones, mixture films with ZnO as the matrix exhibited more dramatic enhancement in conductivity. In **Figure 47a**, it showed that the conductivity of ZnO: Ag NP films was enhanced dramatically when small amounts of Ag NPs were introduced, and it approached to that of AZO: Ag NP films as the Ag content was above 0.70 vol. %. Ag NP embedded in either ZnO or AZO

matrix, exhibited a dramatic degradation in optical transmittance when Ag content was from 0.70 vol. % to 1.40 vol. %. This phenemena are clearly observed and illustrated shown in **Figure 47b.**

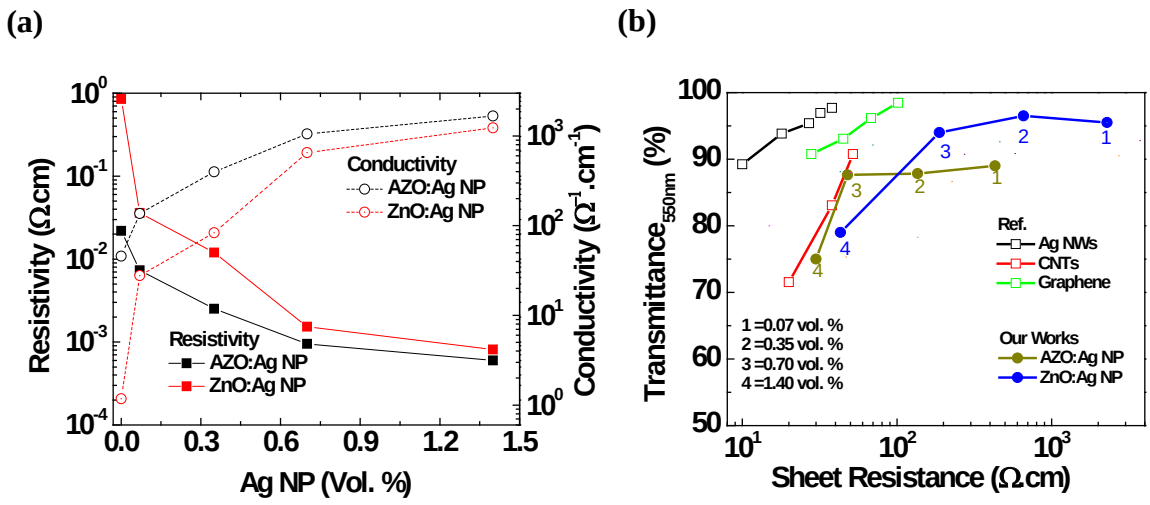

Figure 47. (a) Resistivity vs. Ag content (vol. %), and (b) T_{550nm} vs. R_{sh} diagram of Ag NP embedded in AZO and ZnO matrix.

It is believed those above-mentioned discrepancies in electrical and optical properties of Ag embedded AZO or ZnO films are due to the ohmic contact formed at the interface in which the work function of Ag is smaller than that of ZnO (**Figure 48a**). Therefore, it may explain the reason why ZnO: Ag NP mixture films had dramatic improvement in conductivity as compared to AZO: Ag NP films. Moreover, some donated electrons (red) could be accumulated at the Ag-ZnO interface, shown in **Figure 48b.** This additional charged areas could explain some irregular phenomena in terms of conductivity and optical transparency of these ZnO: Ag NP films especially when Ag content is above 0.70 vol. %.

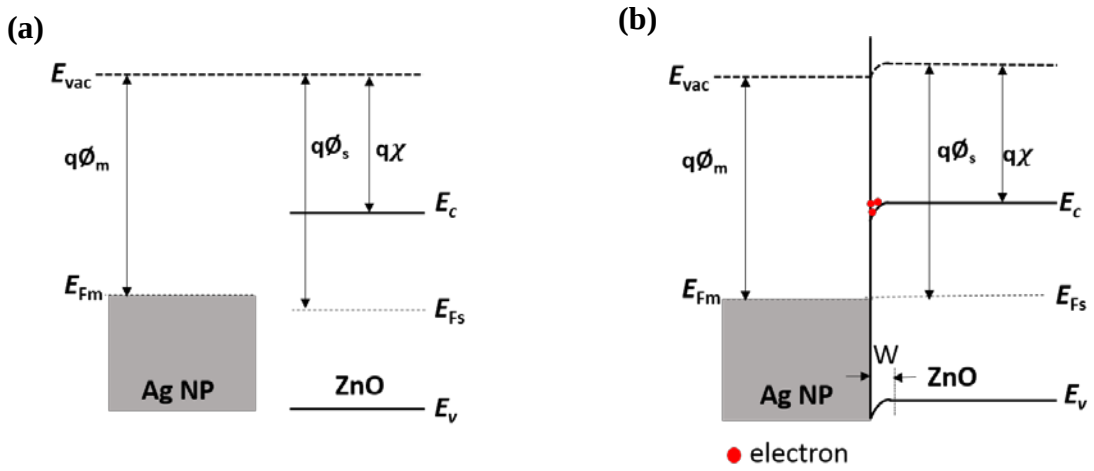

Figure 48. (a) Ag NP and ZnO band diagrams before contact, and (b) the ohmic contact formed at the Ag-ZnO interface.

Given that the width of this accumulated area (W) is in the scale of several tenth nanometers, and the center-to-center distances of Ag NPs are estimated about 100 nm. This additional volume accumulated with electrons lead to an expansion of electron conducting path from an Ag NP toward its adjacent ones (**Figure 49**). This might result in the further enhancement in conductivity. On the other hand, it definitely causes an optical degradation since the effective diameter of each Ag NP is considered having an enlargement from its actual diameter of 30 nm.

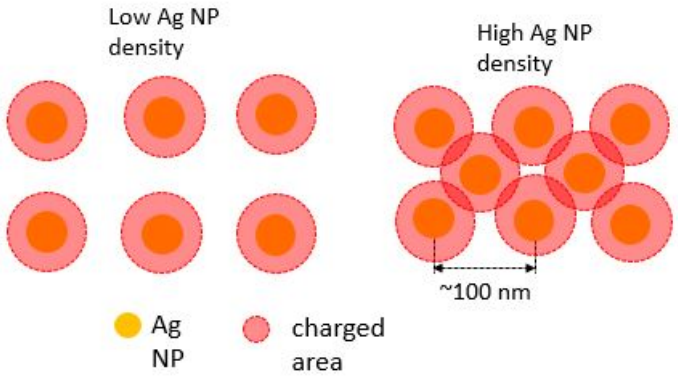

Figure 49. Schematic of Ag NPs and their electron-accumulated areas in the samples with low and high Ag NP density.

3.5.2 Electrical Properties of ZnO: Ag NP/NW Films

3.5.2.1 Background

It was widely reported that the Ag NW-based electrode exhibited excellent conductivity and optical transparency. Ag NW-based electrodes having a sheet resistance of 10 Ω/□ and the optical transmittance of 90 % in the visible wavelengths are promising [60-62], which is very comparable to the commercial ITO electrode (13 Ω/□ at T=96 %). Apart from the high material cost for noble metals (Au and Ag) which limits further use, there are still several technical issues that need to be solved in such one-dimensional metal electrodes prior to being applicable in future optoelectronics: (1) a coarse or rough surface of Ag NWs causes a high haze value, which is defined as the ratio of transmitted radiation diffused to the total transmitted radiation, and the low transmittance (2) bad contacts at wire-wire junctions that increase the electrical resistivity, and (3) a poor adhesion to the substrate associated with a bad mechanical durability as the consequence.

In recent years, it has been suggested that hybrid TCO films that consist of metal nanowires and a TCO coating will improve the surface roughness, the junction resistance, and adhesiveness to the substrate by filling the voids between metal nanowires [63, 64]. In addition, electrons originally transported through TCO grain boundaries have a new conducting pathway as long as metal nanowires are added across grain boundaries. That is, the metal nanowires can serve as excellent electron collectors that gather electrons from either TCO or metals. For example, A. Kim, Y. Won et. al. had their Ag NWs coated with AZO layer. Then they applied this composite electrode (11.3 Ω/□, T=93.4 % at λ=550 nm) for their CIGS solar cells, and concluded that Ag NWs could effectively provide a long term pathway for those photoelectrons [64].

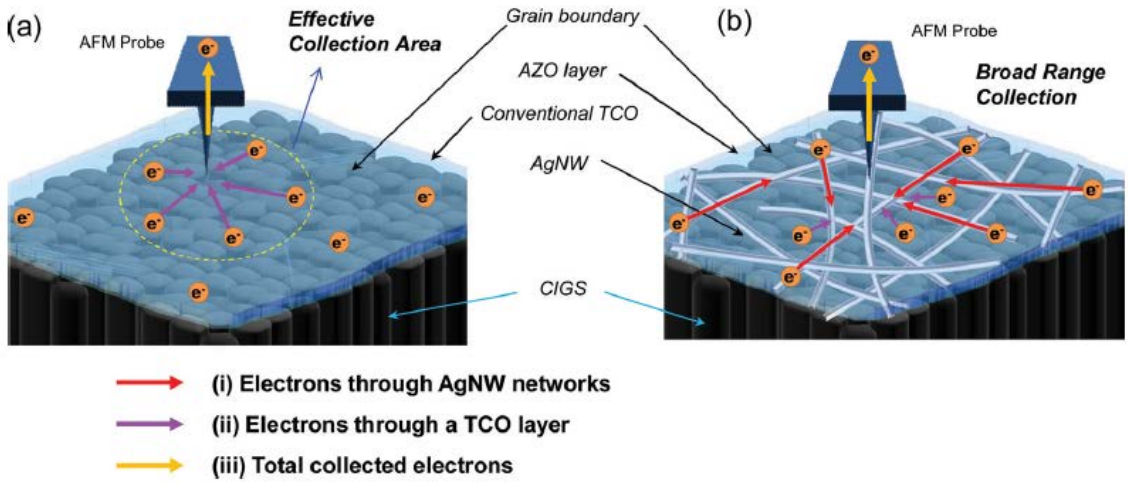

Figure 50. Schematic of two electron collection paths provided by AZO and Ag NWs.

Despite a high amount of Ag NWs can collect electrons more effectively, it would decrease the optical transmittance (or increase haze due to the surface roughness) significantly once the amount of Ag NWs exceeds a certain percolation threshold. Based on the percolation theory, the percolation threshold (f_c, vol. %) is the key factor that defines the boundary where a distinct change occurs in a physical property (e.g., electrical conductivity, dielectric constant, refractive indices, thermal conductivity and so on) of a composite material. This f_c is dependent of microstructural geometry of the composite sample. Assumed that the a binary composite material that is composed of major phase with a particle size of R_1, and the minor phase with a particle size of R_2, it was theoretically calculated that the fc is about 0.16 vol. % as R_1/R_2 is close to 1.0 [65].

The critical condition to obtain the lowest sheet resistance with a good transmittance in those Ag NWs embedded TCO matrix films should be close to this percolation threshold. This critical condition based on the percolation theory was studied in the case of Ag NW films [66]. Instead of using vol. % for their composite system, they correlated the critical density (N_c, cm^{-2}) of Ag NWs (**Eq.29**) with sheet resistance of their composite films. They discovered those samples

in the critical condition exhibited a sharpest change in sheet resistance but did not compromise the optical transmittance. Also, the critical density is inversely proportional to the wire length:

$$l\sqrt{\pi N_c} = 4.326 \qquad \textbf{(Eq.29)}$$

Where l is the wire length (μm), and N_c is the critical density (μm^{-2}) which is synonymous with the percolation threshold (f_c) that promises the lowest sheet resistance obtained without hurting the transmittance significantly as long as the density of Ag NWs is slightly lower or equal to N_c.

It is noted that the longer Ag NWs are, the lower N_c of the AgNWs can be. This implies the Ag nanorods or other nanostructures which have low aspect ratio need to be incorporated much more (square root relation) in these composite films for the percolated conductivity, but cause low optical transmittance (high haze). In the case of their study, N_c was reported as 0.06 μm^{-2}, which was equivalent to 0.75 vol. % with respect to the TCO matrix with a total thickness of 200 nm, assumed the length of Ag NWs is about 10 μm, the width and the thickness are both 40 nm. This value was also supported by another group [67].

Their result provided us a good entrance point to begin with. In this section, their results were adapted to the AZO: Ag NW embedded system. Initially the Ag concentrations in the Ag NP colloidal solutions with a standard specimen were verified based on the Beer-lambert law (**Eq.30**) assumed that all Ag NPs are spherical and the sizes are identical:

$$A=log_{10}(\frac{I_0}{I})=\varepsilon lc \qquad \textbf{(Eq.30)}$$

where A is the absorbance, I and I_0 represented as the transmitted light, and the incident light respectively, epsilon (ε) represents the molar absorptivity (M^{-1}cm^{-1}) or molar absorption coefficient, l is the solution length (cm) defined by the dimension of the quartz cuvette, and c is the molar concentration (M) of particles in the colloidal solution. This equation indicates that the absorbance measured by UV-vis spectrum is linearly proportional to the molar concentration if the

molar absorptivity, which is related to the particle size and the shape, remains constant. Therefore the Ag concentration in each colloidal solution is determined, and results are shown in **Figure 51**.

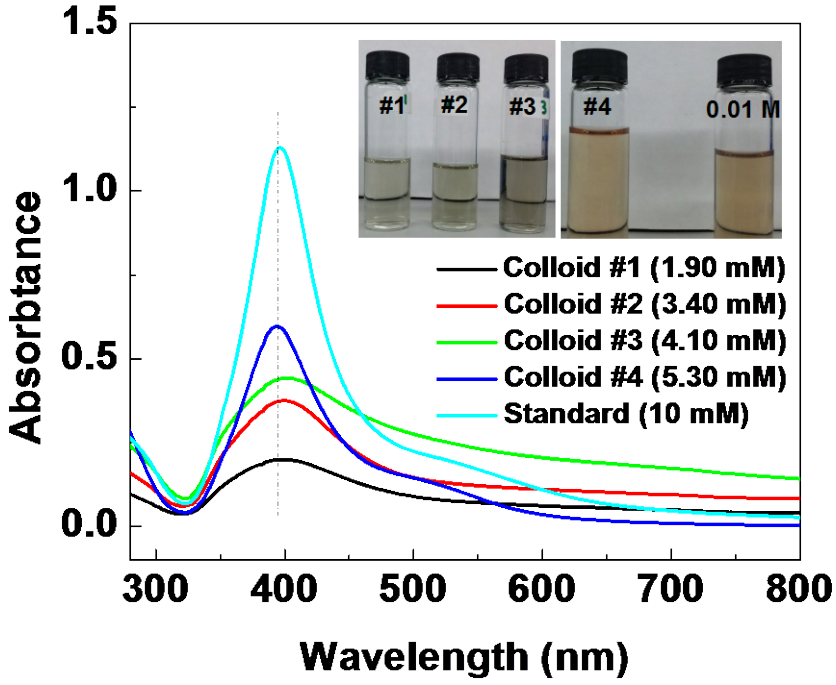

Figure 51. Ag concentrations of colloids determined by the plasmonic absorption.

Afterwards, Ag NPs and Ag NWs were mixed with an atomic ratio of 1:1 but the total Ag content (both Ag NPs and Ag NWs) was controlled in each mixture film. The purpose of this research is to investigate the optimal condition for these Ag NP/NW embedded ZnO films. The optimal condition (vol. %) is expected to be close to the percolation threshold where the percolated conducting path is fully developed. The combination of Ag NP/NW mixture films under such an optimal condition can provide a good figure of merit, but the amount of Ag NWs can be reduced for a good transparency since it is consensual that excessive Ag NWs lead to a poor haze (low transmittance) due to high surface roughness of Ag NWs, which is a common issue for Ag NW-based TCs according to several research reports [60, 66, 68].

3.5.2.2 Experimental

Ag NWs are synthesized via the polyol method which is a self-seeding process without the assistance of exotic seeds (e.g., platinum or gold nanoparticles). Solution A was first prepared by dissolving 0.083g of Polyvinylpyrrolidone (PVP, M.W. ~ 55,000) into propylene glycol (PG). The PVP is not only a protecting agent but a structure-directing agent (**Figure 52**). It was reported that PVP molecules selectively attach on {100}-facets of Ag which results in an anisotropic growth along different crystal axes [69]. Due to the mediocre solubility of PVP molecules in PG, a sonication for 10 min followed by a vigorous stirring prior to next steps is suggested. Once the PVP was totally dissolved, solution A was set aside for future use.

The solution B was prepared by dissolving 2.62 g of 1-Butyl 3-methylimidazolium chloride (BMIM-Cl, $C_8H_{15}ClN_2$) in PG. BMIM-Cl molecule plays a role of controlling the reduction rate of Ag in order to avoid rapid agglomeration of Ag. Once extracting 0.02g of the solution B into A and heating this A+B solution at 90 ℃ for 5 min under nitrogen bubbling was completed, Solution C was slowly injected into this A+B solution, followed by heating this A+B+C solution at 90 ℃ for 24 hours. The color of A+B+C solution initially turned from transparent to brown and eventually turquoise within 24 hours. It is noteworthy that using a plastic container for A+B+C solution is suggested because the Ag NWs tend to stick on the inner wall of silica vials, and this will definitely affect the production yield. Sufficient ethyl acetate was poured into this turquoise A+B+C solution in order to aggregate Ag NWs. Sequentially the precipitate in the bottom could be observed. The solvent was removed carefully. In the end, the brown precipitate of PVP-protected Ag NW aggregates was obtained.

Figure 52. The synthesis of Ag NWs via a self-seeding polyol method.

The brown precipitate (PVP-protected Ag NWs) was carefully washed several times by acetone/ethanol in order to remove PVP molecules and other organic residues that were attached on the surface of Ag NWs. In the end, the weight of those Ag NWs was measured, and were redispersed in an appropriate amount of propanol. We made 1.0 wt. % of Ag NW dispersion each time for the future convenience while mixing with our Ag NPs dispersed in propanol. The synthesis method of our Ag NPs is described elsewhere in the section **3.2.1**. The SEM image (**Figure 53**) shows our Ag NWs have uniform dimensions, which are 15±3.2 μm long and 60±24 nm wide. The aspect ratio (length to width ratio) of the Ag NWs was estimated about 250.

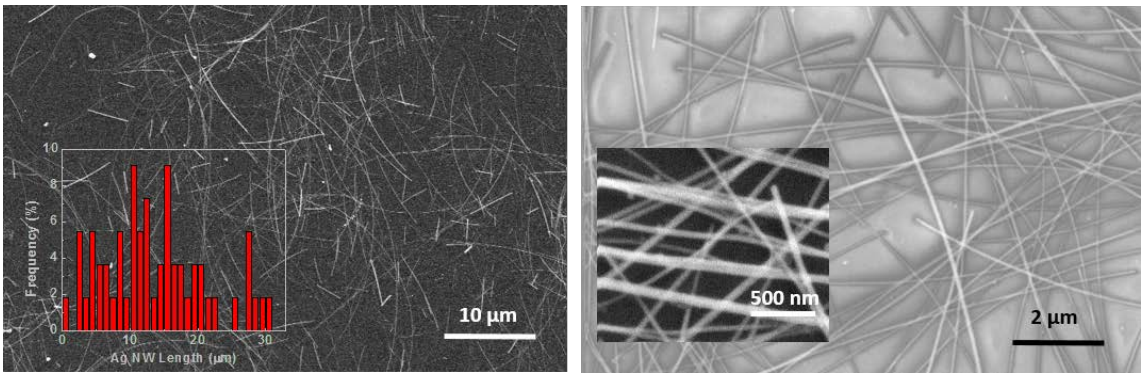

Figure 53. SEM image of Ag NWs. The insets in the left and right are the length distribution and the enlargement showing the width of Ag NWs.

3.5.2.3 Characterization of ZnO: Ag NP/NW Films

The electronic states of Ag NPs/NWs embedded in the ZnO matrix were examined by the XPS shown in **Figure 54**. An Argon-sputtering with a voltage of 3000 eV was applied for 10 seconds in order to remove undesired substances such as H_2O attached to the sample surface. Given that the standard binding energy (B.E.) of Ag^0 $3d_{5/2}$ located at 368.2 eV, and that of AgO $3d_{5/2}$ is located at 367.6 eV, the B.E. of our Ag $3d_{5/2}$ photoemission peaks in our ZnO: Ag NP/NW mixture films are around 368.0-367.8 eV corrected by the C 1s at 284.6 eV as the internal reference. This range of B.E. can be still referred to the pristine Ag state, and only slight Ag-O bonding (B.E. shift) was observed in ZnO: Ag NP/NW films with low Ag contents after annealing in the sequential N_2 and N_2/H_2 mixture atmosphere.

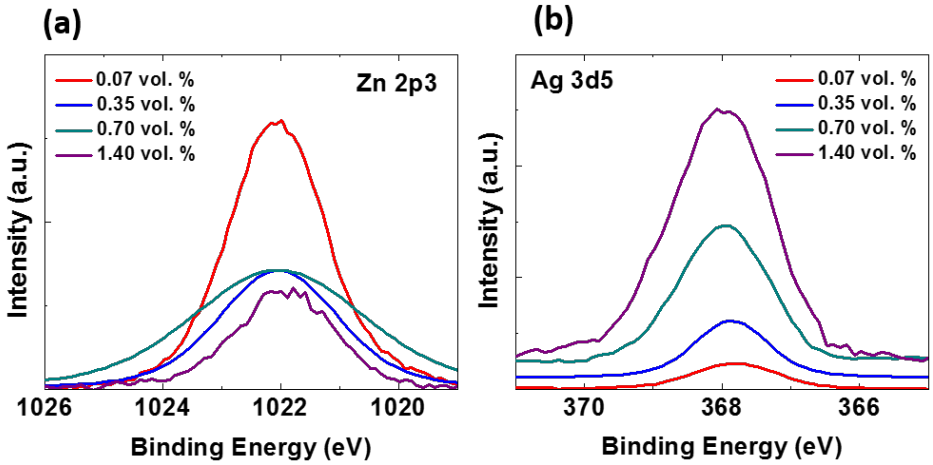

Figure 54. XPS analysis for (a) Zn $2p_{3/2}$, and (b) Ag $3d_{5/2}$ of the ZnO: Ag NP/NW mixture films.

The chemical composition analysis was also revealed by XPS (**Table 7**). Since the Ag content determined by XPS in each sample did not show significant difference as compared to the ideal Ag contents that we originally targeted at, it is not necessary to re-name those samples in order to have a comparison with other TCO composite films systematically.

Table 7. XPS quantitative analysis for Ag contents in ZnO: Ag NP/NW mixture films.

Samples (Targeted vol. %)	Atomic ratio of [Ag]/[Zn]	Converted Vol.% based on XPS
0.07	0.14	0.10
0.35	0.61	0.43
0.70	1.19	0.84
1.40	1.88	1.33

Sheet resistances of those ZnO: Ag NP/NW films were measured by the four-point probe method (**Eq.11**), which was tabulated in **Table 8** along with the resistivity we later converted by the factor of the thickness. It is noted that the silver content in each sample was determined by XPS shown in the ( ) in the first column. The sheet resistance of the sample with 1.40 vol. % of Ag NP/NW mixture was reduced by three orders of magnitude from that of ZnO control sample.

Table 8. Sheet resistance (resistivity) of ZnO: Ag NP/NW films.

Samples (vol. %)	Sheet Resistance (10^2 Ω/□)	Resistivity (Ω.cm)
ZnO	426	8.52×10^{-1}
0.07 (0.10)	22.8	4.56×10^{-2}
0.35 (0.43)	4.62	9.24×10^{-3}
0.70 (0.84)	0.70	1.40×10^{-3}
1.40 (1.33)	0.43	8.60×10^{-4}

Furthermore, the optical transmittance of the ZnO: Ag NP/NW films (**Figure 55a)** all exhibited above 80 % in visible wavelengths except the sample with 1.4 vol. % of Ag content slightly fell short on this criteria around λ=382 nm, which is might due to the plasmonic absorption of Ag NPs. To compare the (a) ZnO: Ag NP/NW films to (b) ZnO: Ag NP films and (c) ZnO: Ag NW films at equivalent amounts of Ag, The relation of optical transmittance at λ=550 nm and the sheet resistance of our mixture films were presented in **Figure 55b**. The FOM of (a) is much superior to that of (c). In addition, (b) exhibited a certain degradation in optical transmittance when

Ag contents were above 0.70 vol. %. This is because the percolated conductivity has been fully achieved, and further increasing the Ag content only has limited improvement in conductivity but causes a great optical degradation. It is believed the percolation initially formed when Ag content was 0.35 vol. %, and fully developed when Ag content reaches 0.70 vol. % in the cases of (a) and (b). More importantly, our critical condition (0.35 vol. % to 0.70 vol. %) for the percolated conductivity in ZnO Ag NP/NW mixture films is less than the critical value (0.75 vol. %) of Ag NW TCs reported by another group [66, 67]. It is believed this earlier formation for percolated conductivity is because Ag NPs can bridge bad wire-wire contacts. Last but not least, the ZnO: Ag NP/NW films also exhibited greater improvement in several aspects summarized below: (1) decreasing sheet resistance by three orders of magnitude before the optical degradation. Conducting electrons are provided from NPs or NWs, and effectively collected by Ag NWs, and (2) the optical degradation is moderate compared to that of ZnO: Ag NW films. This is due to a half amount of Ag NWs was spatially replaced by Ag NPs.

Moreover, the FOM in **Figure 55b** of Ag NP/NW films with Ag content greater than 0.70 vol. % are approaching the FOMs of graphene-based TCs. We believe that if we can increase the length of the wire rather than its width, we have a chance to delay the degradation of optical transmittance of our ZnO: Ag NP/NW mixture films.

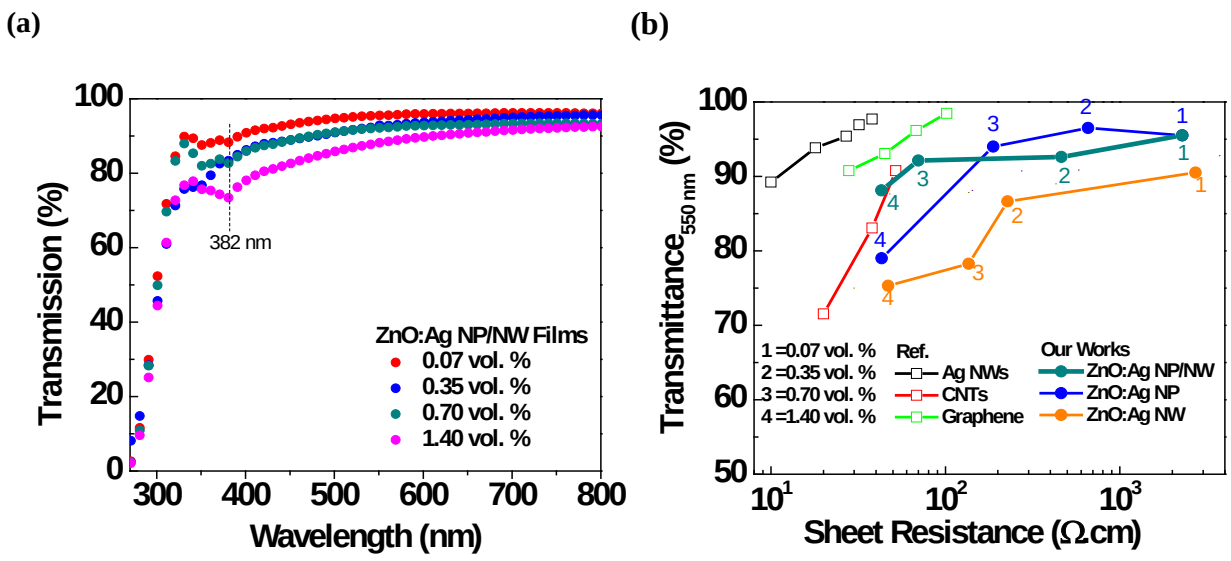

Figure 55. (a) Transmittance of ZnO: Ag NP/NW films as function of wavelengths, and (b) the T_{550} vs. sheet resistance diagram of our mixture films compared to other reference TCs.

4.0 EARTH-ABUNDANT COMPOSITE TCO FILMS

4.1 MOTIVATION

From the viewpoint of sustainability, Cu is an ideal alternative because it is very conductive among metallic elements in the periodic table, and it is 1000 times more abundant, and at least 100 times less expensive than those noble metals such as Au, Ag, Pt, and Pd. However, the formation of a surface oxide layer on Cu nanostructures is commonly observed once they are exposed to the air since its oxidized states (CuO and Cu_2O) are thermodynamically more stable, and it is even more challenging to keep Cu NPs remaining its metallic state in the air atmosphere at room temperature since Cu at nanoscale can be more chemically active than that of bulk Cu.

To solve this problem, a passivation layer coated on Cu surfaces in an inert atmosphere is needed. There are many choices of this passivation layer ranging from carbon-based materials (graphene), organic (polymers) [70, 71], oxide semiconductors [64, 72], and metals (Au, Ag, Ni) [73, 74]. Those reports claimed their Cu-based composite TCs can withstand several oxidation tests or mechanically bending tests since their passivation layer not only altered the chemical stability but also mechanical durability. Despite those appealing results, the solvent-based synthesis for Cu NPs at low temperature is usually involved with the usage of hydrazine (N_2H_2) [74, 75], which is a strong reducing agent, but extremely explosive and toxic. Thus the usage of

hydrazine is strictly regulated, and the storage for this chemical should require extra caution and consideration.

In recent years, P. Hsu, H. Wu et al. successfully fabricated AZO mixed with Cu nanofibers in order to improve the chemical stability of Cu nanofibers under the protection of the AZO coating since it is consensual that the organic compound, poly-(3,4-ethylenedioxythiophene):poly-styrenesulfonate (PEDOT:PSS), is considered as a Lewis acid, and it is commonly used as the hole conductor in organic photovoltaics (OPVs). After their corrosion and oxidation tests, the AZO-Cu nanofibers only show a 10 % increase in resistivity after thermal oxidation at 160 ℃ in dry air and 80 ℃ in humid air (80% relative humidity) in contrast to pure Cu nanofibers that immediately turned into insulators under the same condition [72].

In line with the previous study [58], it is foreseen that those Cu-Ni NPs can provide a great possibility for additional electrons into the ZnO matrix, and this ZnO matrix can prevent those embedded Cu-Ni NPs to be directly exposed in air. This research topic has full motivation since this ZnO: Cu-Ni NP composite system has not been addressed to be an alternative composite TCO for optoelectronics. Therefore the goal is to successfully synthesize Cu-Ni bimetallic NPs via a polyol method in which the reduction occurs in a polyalcohol solution (**Figure 56**)[76].

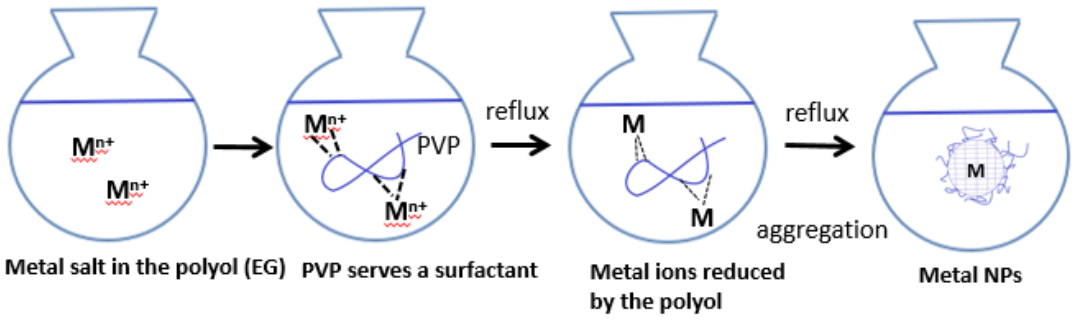

Figure 56. Schematic of the reduction process of metal salts via a typical polyol method.

This polyalcohol, which is the EG in this case, serves not only a polar solvent but a mild reducing agent. The chemical reaction for a metal salt reduced by the polyol can be described in **Eq.31a-b** below [77]:

$$2HOCH_2CH_2OH \rightarrow 2CH_3CHO + 2H_2O \quad (\textbf{Eq.31a})$$

$$2Ag^+ + 2CH_3CHO \rightarrow CH_3CO\text{-}OCCH_3 + 2Ag + 2H^+ \quad (\textbf{Eq.32b})$$

Thus, the strictly-regulated reducing agent such as H_2N_2 can be avoided. Eventually ZnO films embedded Cu-Ni bimetallic NPs were successfully prepared. It is expected that they not only provide a high electrical conductivity with an acceptable transmittance but have a high resistance against oxidation.

4.2 EXPERIMENTAL AND APPARATUS

4.2.1 Synthesis of Cu NPs, Ni NPs and Cu-Ni Bimetallic NPs

The Cu, Ni and their Cu-Ni bimetallic NPs were synthesized by using the polyol method illustrated in **Figure 57**. First of all, an appropriate amount of PVP (M.W is 55,000) was added slowly in 30 ml of ethylene glycol under vigorous stirring and sonication. After the PVP was completely dissolved in EG, this EG/PVP mixture was transferred into a three-necked flask. Secondly, 0.46 g of copper (II) formate tetrahydrate [$Cu(HCO_2)_2 \cdot 4H_2O$] was dissolved in ethylene glycol (EG) with an addition of PVP in three-necked flasks. The PVP molecule played a role of a protecting agent in this polyol method. The reagent Cu solution was particularly treated with argon-bubbling at room temperature for 20 min in order to remove the oxygen content prior to the heat treatment. Thirdly, the solution was heated on a hotplate at 160 ℃ for 60 min under argon-

bubbling. It is noted that once the temperature on the hotplate reached at 160 ℃, 0.5 g of ascorbic acid ($C_6H_8O_6$) served as a reducing agent and was added moderately. The color of this solution immediately turned red, indicating the formation of copper seeds. When more ascorbic acid was added, the color of this solution turned coffee brown. In order to obtain monometallic Cu NPs, the brown precipitate was washed with acetone for several times, and was centrifuged sequentially at 12,000 rpm for 30 min. In the end, those monometallic Cu NPs were then re-dispersed in ethanol for future use.

Similarly, 0.44 g of nickel (II) formate dihydrate [$Ni(HCO_2)_2 \cdot 2H_2O$] was dissolved in 30 ml of ethylene glycol (EG) with PVP pre-dissolved in a three-necked flask as well. The reagent Ni solution was heated on a hotplate at 140 ℃ for 120 min. Once the temperature on the hotplate reached 140 ℃, 0.1 g of sodium borohydride ($NaBH_4$), which served as a strong reducing agent, was added slowly. The solution immediately turned black, which indicates Ni ions were reduced into metallic Ni by $NaBH_4$ with some accompanying gaseous hydrogen. To obtain monometallic Ni NPs, the black precipitate was washed by acetone, and was centrifuged sequentially at 12,000 rpm for 30 min. Eventually those Ni NP were re-dispersed in ethanol for future use.

Regarding the synthesis of Cu-Ni bimetallic NPs, those Cu and Ni reagent solutions were pre-mixed at certain volumes to make the [Cu]/[Ni] atomic ratio about 1:1 in a Teflon vessel. This vessel containing the Cu-Ni mixture was transferred into a microwave reactor, and was rapidly heated at 180 ℃ for 30 min with a ramping rate of 20 ℃/min. The steady heating provided by the microwave radiation not only enhances the reaction kinetics but leads to uniform size and shape of nanoparticles as compared to conventional heating treatments [78, 79]. Once the heating treatment was finished, the Cu-Ni mixture solution was quenched in an ice bath immediately in order to control the uniformity of the bimetallic particle size. Within a rapid heat treatment assisted

by the microwave radiation, Cu-Ni bimetallic NPs were eventually formed and re-dispersed in the ethanol for the future mixing with our ZnO sol-gel with certain volume ratios.

The particle size distributions obtained from DLS is shown in the last diagram of **Figure 57.** This DLS result indicates that the size of Cu NPs is centered at 32 nm, and that of Ni NPs is centered at 18 nm. In addition, the size of Cu-Ni bimetallic NPs is around 25-36 nm with a wider standard deviation. This DLS result not only gives a preliminary clue regarding metallic NPs, and it also implies that the dimensions of metallic NPs were under control.

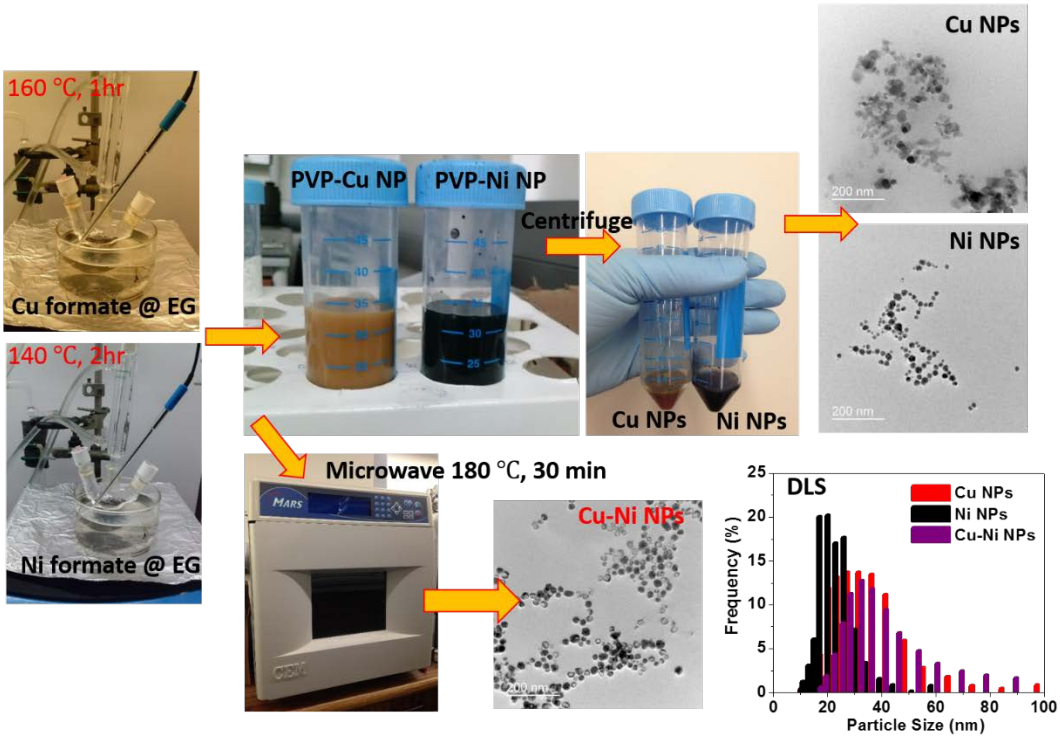

Figure 57. Cu NPs, Ni NPs, and Cu-Ni bimetallic NPs synthesized by the polyol method.

Our monometallic Cu and Ni NPs were first characterized by using a field-emission TEM (JEM-2100F, JEOL) at an accelerating voltage of 200 kV. The specimens for TEM measurements were prepared by dipping 5 µL of ethanoic colloids containing Cu NPs and Ni NPs onto the TEM grids that consist of a carbon coated thin film supported by a gold electroformed mesh (hole size

is 11 µm and wire width is 5.6 µm). Those TEM specimens were naturally dried at the room temperature in a fume hood for a day in order to vaporize the ethanoic solvent completely. According to TEM images shown in **Figure 58**, the size distributions revealed that the monometallic Cu and Ni sizes were 27± 5 nm, and 18± 4 nm respectively. The size of Cu-Ni bimetallic NPs was 30± 5 nm. This value was in an agreement with the DLS results shown in the bottom right of **Figure 57.** In addition, the size of Cu-Ni NPs is larger than that of Cu NP by 10 %, which suggests the possibility of Cu-Ni core-shell structure. The HRTEM images of metallic NPs in the insets of **Figure 58** revealed the morphology of Cu, Ni, and Cu-Ni NPs with a higher magnification. Those metallic NPs seem to be multiple-twinned polyhedrons with stacking faults.

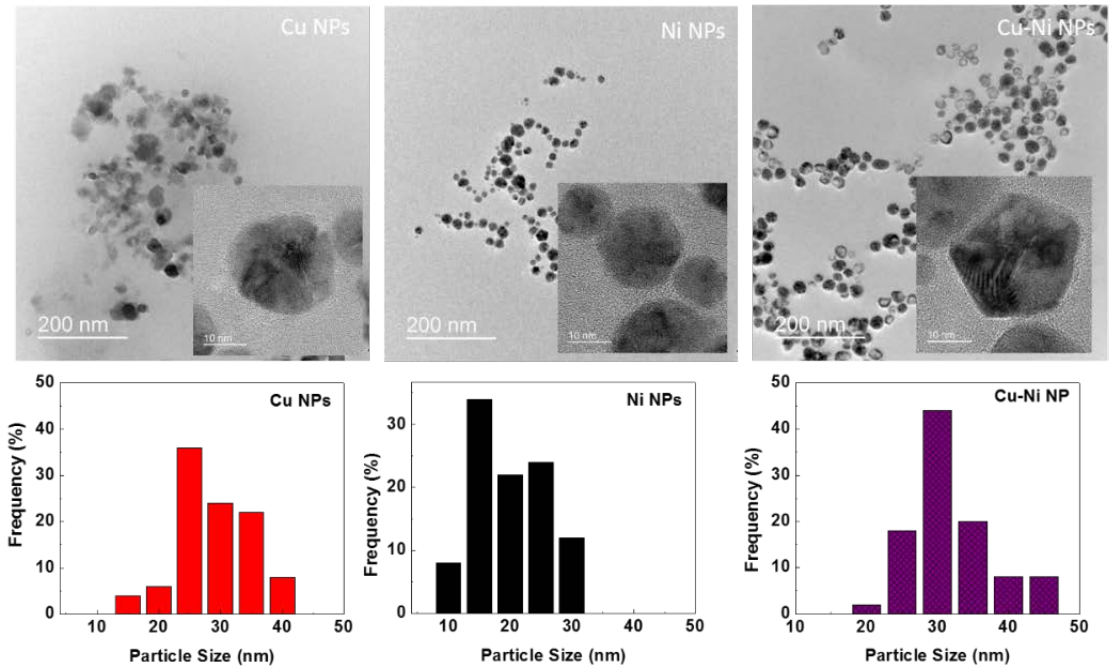

Figure 58. TEM image of Cu, Ni and Cu-Ni bimetallic NPs and their size distributions. The inlets are the HRTEM images of our metallic NPs

4.2.2 High-resolution Transmission Electron Microscopy

The particle wavelength can be calculated according to the de Broglie wavelength (**Eq.33):**

$$\lambda = \sqrt{\frac{150}{E\ (eV)}}\ (\text{Å}) \qquad \textbf{(Eq.33)}$$

where E is the operating voltage (100-400 keV) that is applied for the acceleration of electrons. For the sake of the high-voltage electron beam technique and digital imaging technology that have been improved, the resolution of TEM can be down to several angstroms, which is later so-called high-resolution Transmission electron Microscopy (HRTEM). HRTEM is a very powerful x-ray instrument that provides the information of not only the particle size and its morphology, but also the lattice arrangements at angstrom level from the fringe measurement. Therefore the crystal orientations and structural defects such as dislocations or stacking defects of nanoparticles can be investigated. When an energy-dispersive X-ray spectroscopy (EDS) with a diameter of electron beam less than 2 nm is accessorized with HRTEM analysis, a localized chemical composition analysis can be implemented. Moreover, the scanning TEM (STEM) technique is accomplished when the electron beam (beam size is about 0.5 nm) is scanning over a narrow area of the TEM specimen, second electrons and back-scattering electrons can be generated. The functionality of STEM is similar with SEM but provides a better image resolution. Accompanying EDS, the chemical mapping corresponding to the scanning area can be obtained, which provides researchers useful information about elemental distributions in nanostructured materials.

4.3 CHARACTERIZATION OF COPPER-NICKEL NANOPARTICLES

As-synthesized Cu, Ni, and Cu-Ni NPs were tentatively spin-coated on glass substrates, and were heated on the hotplate at 100 ℃ in order to vaporize the ethanoic solvent. The crystallinity of those metallic NPs were recorded by XRD (X'Pert, PaNalytical) with a Co-Kα radiation of λ=0.179 nm in regular θ- 2θ scans. The peaks located at 2θ =50.7° and 59.30° were assigned to the diffractions from face-centered cubic Cu (111) and (200) planes. In the Cu-Ni NP specimen, the relatively weak peak located at 2θ =51.9 next to the strong Cu (111) peak corresponded to the diffraction from Ni (111).

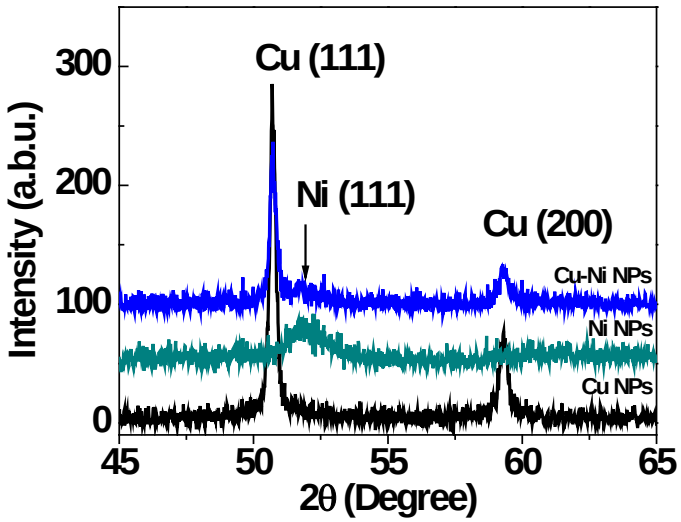

Figure 59. XRD pattern of Cu, Ni, Cu-Ni bimetallic NPs coated on glass substrates

Since there was no XRD peak shift or a phase change observed in Cu-Ni NP specimen as compared to XRD peaks of monometallic Cu or Ni NPs, it suggested that the Cu-Ni bimetallic NPs did not form into either a solid solution or an intermetallic compound. In fact, the Cu-Ni bimetallic NPs could belong to a core-shell structure. The formation of core-shell structure can be

explained by the redox-transmetalation reaction demonstrated by W. Lee and others [74]. The mechanism of ths redox-transmetalation is explained and the schematic is shown in **Figure 60**:

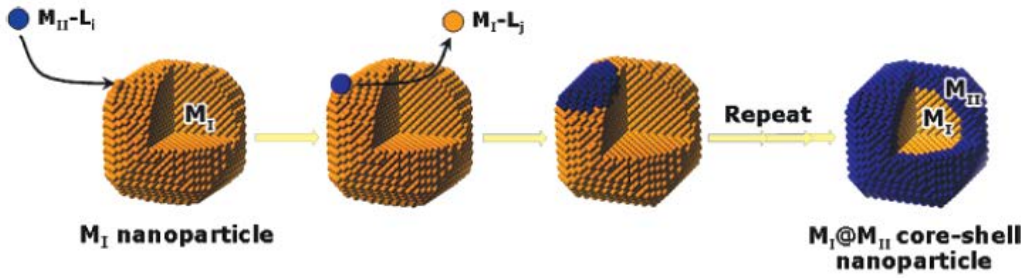

Figure 60. Schematic of core-shell structure via redox-transmetalation process.

where M is metal, and L stands for the ligand (PVP). Essentially, M_{II} ions (Ni) were reduced on the surface of M_I (Cu) seed crystals. In exchange, those neutral M_I atoms on the surface of their parent crystal were oxidized as ions releasing into the solution. By repeating this process, the M_{II}-shell layer can cover the entire M_I-core, and form the M_I@M_{II} core-shell structure. Since Cu and Ni have small lattice mismatch (similar lattice constants), a smooth Ni shell coated on the Cu core, and a relatively spherical core-shell NP could be expected.

Further investigation is needed in order to verify the real nanostructure of the Cu-Ni bimetallic NPs in details. Thus the high-resolution TEM (HRTEM) was empolyed. In **Figure 61b**, the Cu-Ni NPs appears to be five-twinned decahedrons that have five dinstinct facets in the topview. This nanostructure abundantly exists in metal nanocrystals since it has lowest free energy [69]. The fast fourier transform (FFT) of each Cu-Ni NP is shown in **Figure 61c.** Since the grain sizes of the NPs are at the nanoscale (~10 nm), the reciprocal-lattice points will be boardened by this shape effect. As a result, the FFT pattern obtained contains several concentric rings made of discrete spots. It is noted that the lattice constants of cubic fcc Cu and Ni are very close (0.361 nm for Cu and 0.352 nm for Ni), The d-spacing values converted from **Figure 61c** can be only

determined to be fcc {111} and fcc {200} of either Cu or Ni. One of five facets of a Cu-Ni NP was selected (the facet of the geometric model in the inset is marked in red) for the lattice fringe analysis revealed by higher magnification HRTEM image shown in **Figure 61d**. The d-spacing values are calculated as 0.20 nm and 0.18 nm based on ten lattice fringes, which coincides the distances of fcc {111} and fcc {200} planes normal to [111] and [200] directions with a lattice constant close to either Cu or Ni.

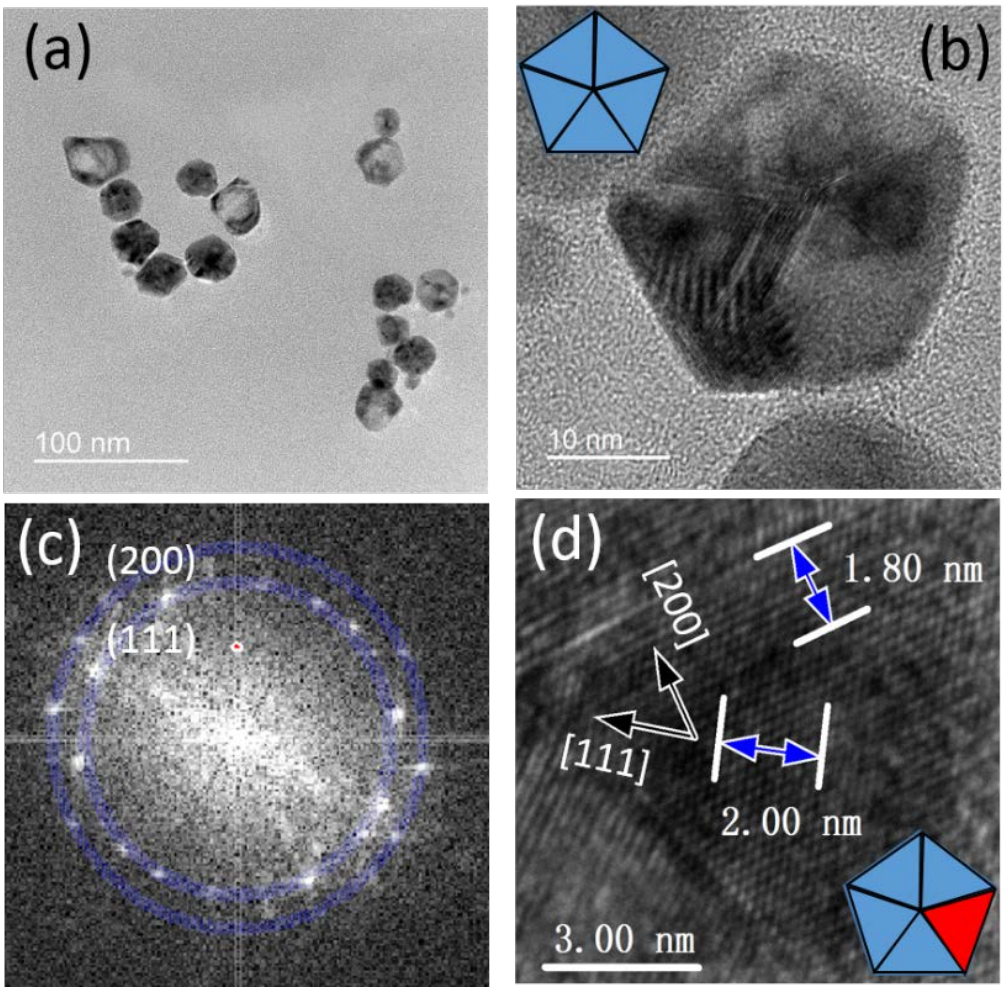

Figure 61. (a) TEM image of Cu-Ni NPs, (b) HRTEM image of a Cu-Ni NP, (c) FFT transform pattern, and (d) HRTEM image of Cu-Ni NP. The insets in (b) and (d) are five-twinned decahedrons.

Furthermore, the chemical quantitative measurements of the Cu-Ni NPs were implemented by scanning TEM (STEM) equipped with a high-angle annual dark-field (HAADF) detector and an energy dispersive X-ray spectroscopy (EDS). Quantitative analysis via TEM-EDS indicates the atomic ratio of Cu and Ni is 52:48, which is very close to 50:50 as we expected (**Figure 62a-b**). The annular dark-field imaging of theCu-Ni NPs shown in **Figure 62c** reveals a subtle Z-contrast of core-shell structure. In fact, this Z-contrast did not provide a sharp contrast in our bimetallic NPs since Cu and Ni have similar Z-values (atomic number of Cu is 29 and that of Ni is 28). Therefore the STEM-EDS chemical mapping was employed for a better interpretation. This chemical mapping provides the chemical distribution of elemental Cu and Ni containing in Cu-Ni bimetallic NPs. The distribution suggested the Cu-Ni core-shell structure is presented. Moreover, the Cu-core thickness is 20 nm, and the Ni-shell is about 10 nm. On the other side, the atomic ratio of [Cu]:[Ni] can be deduced from the Cu-Ni Core (20 nm)-shell (10 nm) model, if Cu-Ni NPs are perfectly spherical and the densities of Cu, Ni are 8.89 g/cm^3 and 8.91 g/cm^3 are given. The [Cu]:[Ni] is very close to 52:48, which is consistent with the abovementioned result obtained from TEM-EDS.

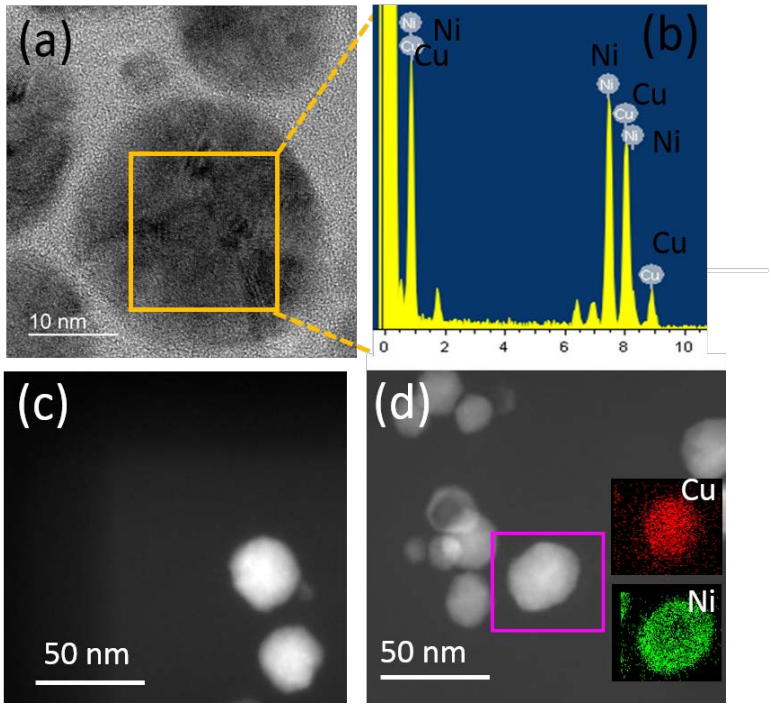

Figure 62. HRTEM/STEM-EDS analysis for Cu-Ni NPs. (a) HRTEM image. (b) EDS analysis for Cu-Ni NPs. (c) Dark-field Z-contrast image. (d) STEM-EDS mapping for a single Cu-Ni NP.

4.4 ZINC OXIDE: COPPER-NIKEL MIXTURE FILMS

In order to detect the chemical states of Cu and Ni as well as the Cu-Ni (50:50) contents in the four representative mixture films, the XPS analysis corrected by the internal reference of C 1s at 284.6 eV was performed shown in **Figure 63**. The photoemission peak of Zn $2p_{3/2}$ located at 1022 eV refers to the Zn-O bonding (Zn $2p_{3/2}$ peak in ZnO is 1021.7 eV). According to the XPS handbook [80], Cu^0 2p3 is located at 932.4 eV and its common oxides, Cu_2O and CuO, are located at 932.5 eV and 933.4 eV; Ni^0 $2p_{3/2}$ is located at 852.3 eV and its oxide (NiO) is located at 853.3 eV. In comparison, photoemission peaks of Cu $2p_{3/2}$ and Ni $2p_{3/2}$ of the ZnO: Cu-Ni NP films were unanimously centered at 932.67 eV and 853.1 eV, indicating that the chemical stage of the

elemental Cu remains pristine, and the Ni is slightly oxidized. This result coincides with our expectation that Ni tends to form a NiO_x passivation coating over the reduced Cu since the standard reduction potential of Cu is 0.34 V and that of Ni is -0.26 V. Since this passivation coating is very thin on the surface, it would provide a great chemical protection for the Cu core even though the mixture films were treated at 300 ℃ on a hotplate, rather than significantly impede the electrical conductivity of Cu-Ni NPs.

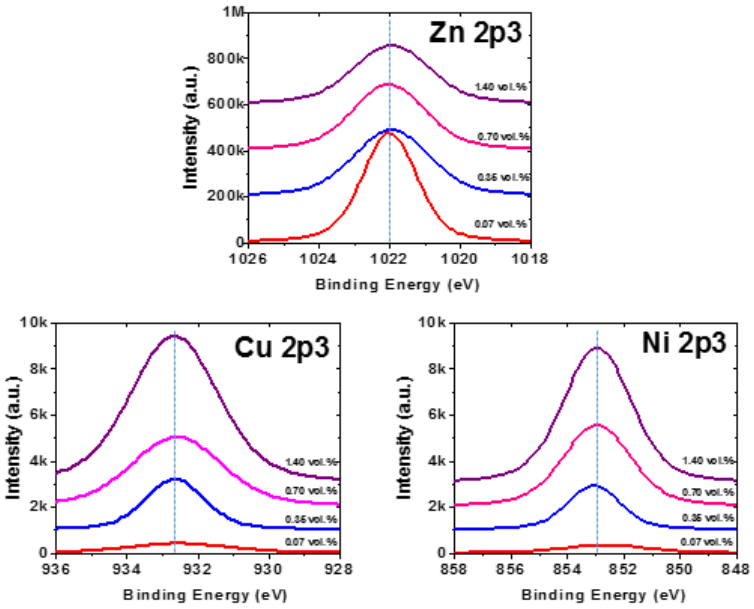

Figure 63. XPS Photoemissions of Zn $2p_{3/2}$, Cu $2p_{3/2}$, and Ni $2p_{3/2}$.

The XPS quantitative analysis for atomic ratio of [Cu]:[Ni] and Cu-Ni content (vol.%) with respect to the ZnO matrix was accomplished by calculating the areas under the fitted XPS curves. The results were summarized in **Table 9**. Each of the Cu-Ni bimetallic NPs exhibited the atomic ratio of [Cu]:[Ni] about 60:40, which was close to 50:50 observed from TEM-EDS. Moreover, the Cu-Ni contents (vol. %) in our four representative mixture films were converted from the atomic ratio of [Cu]:[Zn] detected from XPS. They were 0.10, 0.37, 0.80, and 1.31 vol. %. Those volume

contents are fairly close to 0.07, 0.35, 0.70, 1.40 vol. % that were purposefully targeted in order to have a future comparison with other TCO mixture films with equivalent amounts of metallic constituent.

Table 9. XPS Quantitative analysis for atomic (volume) ratios of [Cu]:[Ni].

Samples (Targeted vol. %)	Atomic ratio of [Cu]:[Ni]	Atomic ratio (%) of [Cu]/[Zn]	Converted Vol.% based on XPS
0.07	65:35	0.14	0.10
0.35	62:38	0.53	0.37
0.70	59:41	1.14	0.80
1.40	64:36	1.85	1.31

The sheet resistance of ZnO: Cu-Ni (50:50) mixture films were measured by the four-point probe method according to **Eq.11**. The result was tabulated in **Table 10** including the resistivity converted by the sheet resistance multiplied by the thickness of 200 nm. In this case, the sheet resistance of the ZnO: Cu-Ni (50:50) mixture film with 1.40 vol. % of Cu-Ni NPs was reduced by approximately two orders of magnitude from that of ZnO control sample. In contrast, the ZnO: Cu NP film (0.76 vol. %) did not have significant change from the control sample. This is because the Cu NPs without a proper passivation layer might be oxidized during the heat-treatment.

Table 10. Sheet resistance (resistivity) of ZnO: Cu-Ni NP (50:50) films.

Samples (vol. %)	Sheet Resistance (10^2 Ω/□)	Resistivity (Ω.cm)
ZnO	426	8.52×10^{-1}
ZnO: Cu NP	362	7.51×10^{-1}
0.07 (0.10)	37.3	7.46×10^{-2}
0.35 (0.37)	5.82	1.16×10^{-2}
0.70 (0.80)	2.74	5.48×10^{-3}
1.40 (1.30)	1.43	3.86×10^{-3}

At the same time, the optical transmittance of the ZnO: Cu-Ni NP films all exhibited above 88 % in visible wavelengths. This transmittance loss around 550 nm should be associated with the surface plasmon resonance (SPR) of Cu-Ni NPs. It is noteworthy that pure Cu normally has a relatively weak characteristic SPR absorption ranging from 550 nm to 600 nm as compared to those sharp SPR absorptions observed from strong plasmonic metals such as Au NP at 517-526 nm and Ag NP at 395-416 nm [81] [82]. Moreover, it has been reported that Ni is a non-plasmonic metal which has no characteristic SPR absorption observed due to the fact that most transition metals have a strong coupling between the plasmon transition and the d-d excitation. Thus, the plasmon energy is lost by excitation of the single electron in interband transitions [83]. More importantly, the Ni shell could further dampen the SPR absorption of its core-shell NPs [83-85]. This Ni damping effect significantly caused a broad SPR absorption toward longer wavelengths.

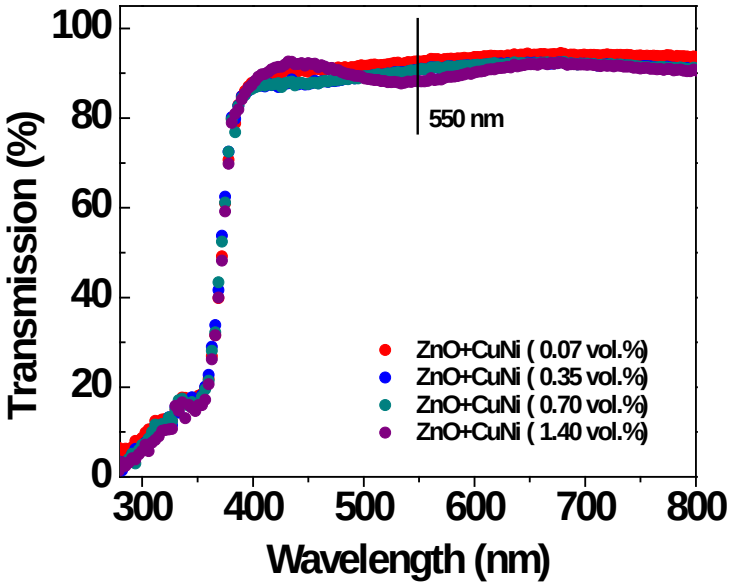

Figure 64. Transmittance of ZnO: Cu-Ni NP (50:50) films as function of wavelengths.

The optical transmittance at λ=550 nm (T_{550}) and the sheet resistance of the ZnO: Cu-Ni (50:50) NP mixture film (R_{sh}) in T_{550}-R_{sh} diagram are presented in **Figure 65.** This correlation is

strongly associated with the FOM of TCO films. ZnO: Cu-Ni (50:50) NP mixture films did not outperform other mixture films of our works. The sheet resistance fell short on our expectation because NiO formation could impede the electron donation from NPs. this could be solved if we can further lower down the annealing temperature. Regarding the optical transmittance, this T_{550}-R_{sh} plotting might play a bias over these ZnO: Cu-Ni NP mixture films since the characteristic SPR absorption of Cu was around 550-600 nm. Nevertheless it was still observed that a moderate transmittance loss from point 3 to point 4 (equivalent to 0.7 vol. % to 1.4 vol. %) as compared to that of ZnO: Ag NP or ZnO: Ag NP/NW films. This is because that the Ni shell might dampen the SPR absorption of Cu core, and this absorption peak was broadened and red-shifted. Therefore, it is expected that further improvement could be achieved when SPR absorption by different ratios of [Cu]/[Ni] can be tunable toward the near IR region (λ=700-1000 nm). Therefore, the curve in this T_{550} -R_{sh} diagram would remain in the upper-left corner where a well-qualified TCO composite film is located.

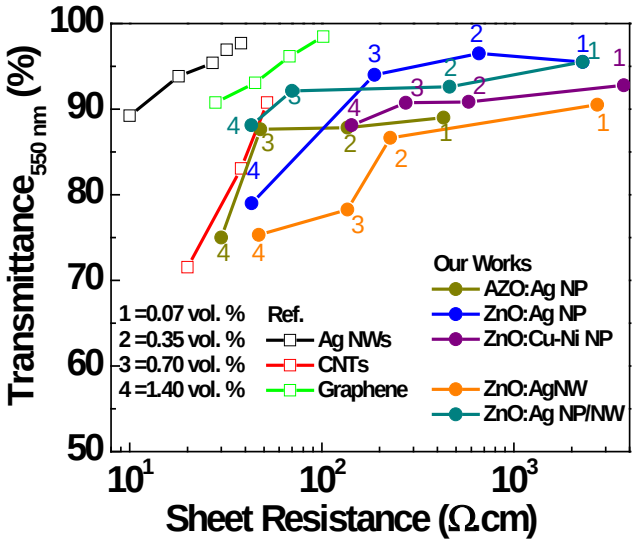

Figure 65. Transmittance (T_{550}) vs. sheet resistance of our works compared to the references.

5.0 CONCLUSION

First of all, electrical properties of Au NP-embedded ZnO films are examined. The Au NPs were converted from the evaporated Au nanolayer after annealing. In fact, we discovered an increase in the thickness of the initial Au mid-layer in the ZnO: Au NP mixture film only increases the density of Au NPs rather than the particle size. The electron concentration of Au NP embedded ZnO films dramatically increased due to the electron donation from Au NPs to the ZnO matrix. During the temperature range from 200-340 K, Au NP electrons across a certain energetic barrier were donated into ZnO matrix. This energetic barrier height was close to 188 meV according to the Arrhenius correlation. We believe the Schottky barrier at Au-ZnO interface is responsible for this energetic barrier height. Thus, we believe that the magnitude of this energetic barrier is associated with the work function difference between ZnO and Au NPs. This study offers a design rule for highly conductive TCO composite films that do not have the tradeoff between carrier concentration and carrier mobility since conducting electrons are not generated from conventional impurity-doping.

In line with our previous study, the mixture films comprised of Ag NPs embedded in AZO and ZnO matrix were prepared via one-pot wet-chemistry method since wet-chemistry method provides good controllability on the particle size and dispersion in oxide matrix. The presence of Ag NPs embedded was visually observed by the color contrast showing two different conducting domains while the c-AFM technique was applied. Moreover the Ag NPs in the mixture films

remained in the metallic state without oxidation revealed from XPS. Similarly electrons donated from Ag NPs need to thermally overcome the Schottky barrier at the Ag-AZO interface in order to transport in the AZO matrix. Given that the work function of Ag is 4.67 eV and that of AZO varies conditionally from 3.7 to 4.7 eV, electrons donated from Ag NPs exhibited negligible temperature dependence, which can refers to a small Schottky barrier (~13 meV) at the Ag-AZO interface in this case. In addition, the mixture films with the Ag content above 0.35 vol. % exhibited slightly higher electron mobility than that of the AZO control sample. We believe this is due to the fact that the donated electrons coordinate those positively-charged impurities. As a result, the magnitude of the charged impurity scattering can be reduced. Our sample with the best FOM was 2.72×10^{-3} Ω.cm (136 Ω/□) with T_{550}=87 % as 0.70 vol. % of Ag NPs was added. The Hall mobility of AZO: Ag NP mixture films remained around 20 cm^2/V.s.

To broaden the study above, ZnO films embedded with Ag NPs/NWs were fabricated. These composite films exhibited better FOMs as compared to FOMs of ZnO: Ag NP films. This is due to the percolated conducting network has established by the synergic effort of Ag NWs and Ag NPs. Conducting electrons in this case could be provided either from Ag NPs or Ag NWs, and transported more efficiently in the percolated path made of Ag NWs than in the ZnO matrix. Nevertheless, the ZnO matrix here not only provides a passivation against the oxidation of the Ag nanostructures, but it improves the junction-resistance and the adhesiveness with the substrate by filling the voids between NPs and NWs. In our case, the transition of this percolated conductivity in these ZnO: Ag NPs/NWs films was from 0.35 to 0.70 vol. %, and our best ZnO: Ag NP/NW sample exhibited the resistivity as 8.6×10^{-4} Ω.cm (R_{sh}=43 Ω/□) at T_{550}=88 %.

From the aspect of affordability and sustainability, ZnO films embedded earth-abundant Cu-Ni bimetallic NPs were fabricated via wet-chemistry method. The size of our Cu-Ni NPs was

about 30 nm. The morphology of Cu-Ni NPs seemed to be fivefold-twinned decahedrons in the structure of 20 nm Cu core- 10 nm Ni shell revealed by HRTEM images and STEM-EDS. Cu core was not oxidized since the Ni shell partially formed the passivation on the surface of Cu core. This evidence was revealed by XPS. The characteristic SPR absorption of Cu is around 550-600 nm in our case as compared to approximately 400 nm of our Ag NPs, a relatively low transmittance at λ=550 nm for these ZnO: Cu-Ni NP films was expected. Despite of that, a moderate transmittance loss in high Cu-Ni content (0.7 vol. % to 1.4 vol. %) due to the fact that Ni shell could dampen the SPR absorption of Cu core. As a result, the SPR absorption of Cu cores shifted toward longer wavelengths or became less intensified. On the other hand, the curve of such ZnO: Cu-Ni NP mixture films have chance to move toward the upper-left corner of the T_{550}-R_{sh} diagram where stands for highly qualified TCOs that possess a low resistivity but high optical transmittance if the plasmonic wavelength of Cu core is tuned away from the visible region by changing the [Cu]/[Ni] ratio.

6.0 FUTURE WORKS

6.1 COPPER NANOWIRE-EMBEDDED ZINC OXIDE

Ag nanowires (Ag NWs) has become a commercialized product that is formulated in the conductive ink due to its excellent conductivity for patterning the contact electrode of a modern optoelectronics. However, copper nanowires (Cu NWs), one of competitors for Ag NWs, is much earth-abundant and cost-effective. Thus Cu NWs soon have attracted researchers' great interests as an alternative material for conductive electrodes. In addition, it has been reported that Cu NWs with good uniformity synthesized by wet chemistry without using a restricted reducing chemical (H_2N_2) is available. H.-J. Yang, S.-Y He et al. presented a mechanism that Cu atoms deposit on {111}-facets of Cu seeds as {100}-facets were capped by the oleylamine (OLA) (**Figure 66**) [86].

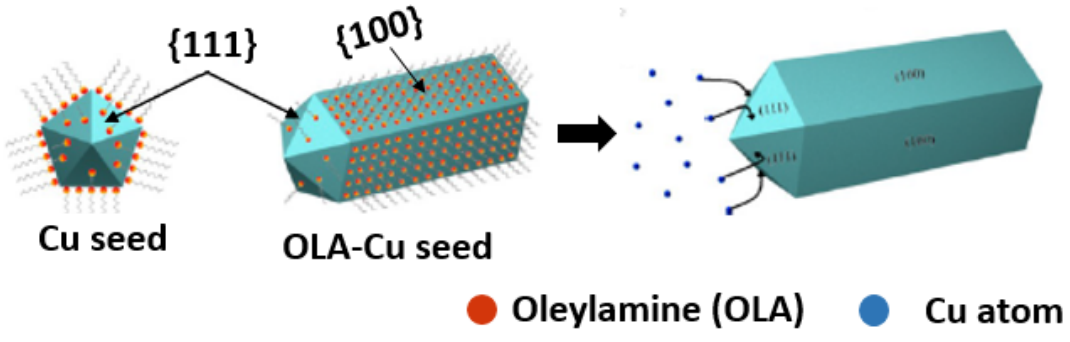

Figure 66. Schematic of Cu NW formation through the anisotropic growth.

Moreover, H. Guo, Y. Chen kinetically controlled the shape of Cu or Cu@Cu-Ni core-shell nanostructures from nanocubes (NCs) to nanowires (NWs) by one-pot chemical reduction process with or without addition of trioctylphosphine (TOP) ligand molecule [84]. In the condition without TOP, Cu ions are reduced quickly by Ni°. As a consequence, multi-twinned Cu crystal seeds, which are the building block of Cu NWs, are rapidly formed. Their Cu@Cu-Ni core-shell NCs and NWs are synthesized by the similar technique with some modification.

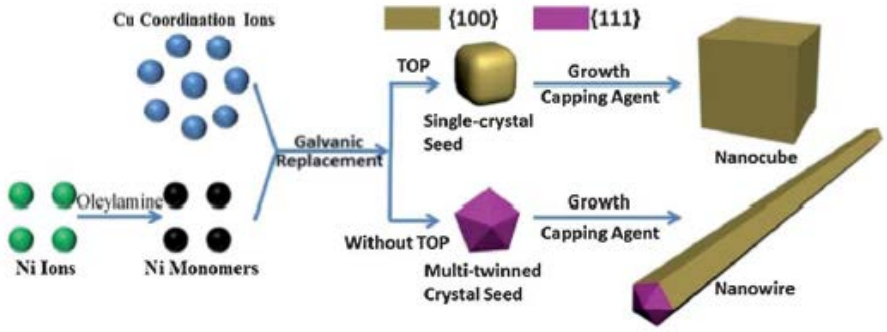

Figure 67. Schematic for the formation of Cu NCs and Cu NWs

Cu NWs have faced several difficulties that are similar with Ag NWs mentioned above in the section **3.5.3**, including the mechanical durability, thermal and chemical stability against oxidation. In order to resolve those problems, Cu NW-based composite materials are extensively investigated [87] [88]. A. Rathmell, M. Nguyen et al., developed oxidation-resistant Cu-Ni bimetallic NWs for transparent conducting electrodes [87]. The sheet resistance of Cu-Ni NWs remained constant after several cycles of the oxidation test. Also, Y. Ahn, Y. Jeong et al. fabricated Cu NW-graphene core-shell (Cu NW-G) nanostructures and the sheet resistance were about 53.8 Ω/□ at T_{550} =89.3 % [88]. Moreover, the resistance of Cu NW-G films only increased 9 % within 30 day, and 27 % after 120 hours in a humid environment (70 ℃/70 % RH). Compared to Cu NW films, the sheet resistance had an increase over 1800 times within 2 days, and 76 times in 30 min.

This dramatic difference is due to the graphene shell provided a passivation coating that oxygen and moisture cannot permeate. Similarly we foresee the prospect of Cu@Ni NW/NP embedded ZnO mixture films in terms of the electrode material for optoelectronic devices. Ni shell supposedly provides a much smoother passivation coating on the Cu core since the Ni and Cu have the same crystal structure (fcc) and the lattice mismatch is less than 2 %. In line with our previous studies, we further expected that conducting electrons can be provided from those Cu@Ni NPs, and collected by the network of Cu@Ni NWs effectively. The ZnO filling the void space between metal nanostructures can consequently provide a good adhesiveness with the substrate, improve the surface roughness and reduce the wire-wire junction resistance.

6.2 ZINC OXIDE FILM BY MODIFIED SOL-GEL METHOD

The conventional ZnO sol-gel presented in the previous section always require high-temperature annealing around 500 ℃ in order to have a complete hydrolysis and condensation reactions. However, most excitonic solar cells, especially OPVs, DSCs or QDSCs, could not withhold such a high-temperature since there are some temperature-sensitive organics involved. This drawback limits the applications of ZnO-based composite films. The combustion sol-gel precursor has been suggested to resolve this problem [64]. The combustion-derived reaction is highly exothermic, which is not necessary to obtain the thermal energy from the external source as compared to the conventional sol-gel process, which is an endothermic reaction [89]. The ZnO fabricated from the combustion sol-gel precursor can possibly reduce the annealing temperature. This improvement in the annealing temperature is appealing to fabricate conductive ZnO: metal nanostructured composite electrodes on solar cells with flexible substrate.

BIBLIOGRAPHY

[1] Y. Dou, R. G. Egdell, T. Walker, D. S. L. Law, and G. Beamson, Surface Science, 1998, vol. 398, pp. 241-258.

[2] USGS, "Mineral commodity summaries 2013," 2013.

[3] Z. L. Wang, Materials Science and Engineering R, 2009, vol. 64, pp. 33-71.

[4] T. S. Herng, A. Kumar, C. S. Ong, Y. P. Feng, Y. H. Lu, K. Y. Zeng, and J. Ding, Scientific Reports, 2012, vol. 2, p. 1.

[5] M. Ding, D. Zhao, B. Yao, B. Li, and Z. Zhang, Applied Physics Letters, 2011, vol. 98, p. 062102.

[6] K. Ellmer, A. Klein, and B. Rech, Transparent Conductive Zinc Oxide: Basics and Applications in Thin Film Solar Cells.: Springer, 2008.

[7] A. Janotti and C. G. V. d. Walle, Reports on Progress in Physics, 2009, vol. 72, p. 126501.

[8] J.-P. Lin and J.-M. Wu, Applied Physics Letters, 2008, vol. 92, p. 134103.

[9] T. Minami, MRS Bulletin, 2000, vol. 25, pp. 38-43.

[10] I. S. Kim, E.-K. Jeong, D. Y. Kim, M. Kumar, and S.-Y. Choi, Applied Surface Science, 2009, vol. 255, pp. 4011-4014.

[11] Y.-J. Lin, M.-S. Wang, C.-J. Liu, and H.-J. Huang, Applied Surface Science, 2010, vol. 256, pp. 7623-7627.

[12] Y. T. Shih, J. F. Chien, M. J. Chen, J. R. Yang, and M. Shiojiri, Journal of The Electrochemical Society, 2011, vol. 158 (5), pp. H516-H520.

[13] A. Tsukazaki, A. Ohtomo, T. Onuma, M. Ohtani, T. Makino, M. Sumiya, K. Ohtani, S. F. Chichibu, S. Fuke, Y. Segawa, H. Ohno, H. Koinuma, and M. Kawasaki, Nature Materials, 2004, vol. 4, pp. 42-46.

[14] D. C. Look and D. C. Reynolds, Applied Physics Letters, 2002, vol. 81, p. 1830.

[15] S. Calnan and A. N. Tiwari, Thin Solid Films, 2010, vol. 518, pp. 1839-1849.

[16] J. Y. W. Seto, Journal of Applied Physics, 1975, vol. 46, p. 5247.

[17] M. Batzill and U. Diebold, Progress in Surface Science, 2005, vol. 79, p. 2005.

[18] H.-C. Lee, Applied Surface Science, 2006, vol. 252, pp. 3428-3435.

[19] D. H. Zhang and H. L. Ma, Applied physics A, 1996, vol. 62, pp. 487-492.

[20] K. Nomura, H. Ohta, A. Takagi, T. Kamiya, M. Hirano, and H. Hosono, Nature, 2004, vol. 432, p. 488.

[21] S. Jeong, Y.-G. Ha, J. Moon, A. Fachetti, and T. J. Marks, Advanced Materials, 2010, vol. 22, pp. 1346-1350.

[22] A. Facchetti and T. J. Marks, Transparent Electronics: From Synthesis to Application: Wiley, 2010.

[23] K. Nomura, A. Takagi, T. Kamiya, H. Ohta, M. Hirano, and H. Hosono, Japanese Journal of Applied Physics, 2006, vol. 45, pp. 4303-4308.

[24] D.-H. Lee, Y.-J. Chang, G. S. Herman, and C.-H. Chang, Advanced Materials, 2007, vol. 19, pp. 843-847.

[25] G. H. Kim, H. S. Shin, B. D. Ahn, K. H. Kim, W. J. Park, and H. J. Kim, Journal of The Electrochemical Society, 2009, vol. 156, pp. H7-H9.

[26] E. Fortunato, P. Barquinha, and R. Martins, Advanced Materials, 2012, vol. 24, pp. 2945-2986.

[27] M. Grtäzel, Inorganic Chemistry, 2005, vol. 44, p. 6841.

[28] J.-K. Lee and M. Yang, Materials Science and Engineering B, 2011, vol. 176, p. 1142.

[29] J. Baxter, A. Walker, K. V. Ommering, and E. Aydil, Nanotechnology, 2006, vol. 17, p. 304.

[30] K. H. Kim, K. Utashiro, Z. Jin, Y. Abe, and M. Kawamura, International Journal of Electrochemical Science, 2013 vol. 8, p. 5183.

[31] M. A. Green, A. Ho-Baillie, and H. J. Snaith, Nature Photonics, 2014, vol. 8, p. 506.

[32] H.-S. Kim, C.-R. Lee, J.-H. Im, K.-B. Lee, T. Moehl, A. Marchioro, S.-J. Moon, R. Humphrey-Baker, J.-H. Yum, J. E. Moser, M. Grtäzel, and N.-G. Park, Scientific Reports, 2012, vol. 2, p. 1.

[33] D. Liu and T. L. Kelly, Nature Photonics, 2014, vol. 8, p. 133.

[34] D.-Y. Son, J.-H. Im, H.-S. Kim, and N.-G. Park, The Journal of Physical Chemistry C, 2014, vol. 118, p. 16567.

[35] T. Yamamoto, H. Song, and H. Makino, Pysica Status Solidi C, 2013, pp. 1-3.

[36] H. Liu, V. Avrutin, N. Izyumskaya, U. Ozgur, and H.Morkoc, Superlattices and Microstructures, 2010, vol. 48, pp. 458-484.

[37] B. G. Streetman and S. Banerjee, Solid State Electronic Devices, 5th ed.: Prentice Hall, 1999.

[38] D. J. Cohen and S. A. Barnett, Journal of Applied Physics, 2005, vol. 98, p. 053705.

[39] K. Ellmer and G. Vollweiler, Thin Solid Films, 2006, vol. 496, p. 104.

[40] I. A. Rauf, Journal of Materials Science Letters, 1993, p. 1902.

[41] S. Lee, S. Bang, J. Park, S. Park, Y. Ko, and H. Jeon, Physica Status Solidi A, 2012, vol. 209, pp. 698-701.

[42] K. Sivaramakrishnan and T. L. Alford, Applied Physics Letters, 2010, vol. 96, p. 201109.

[43] C. Corti and R. Holliday, Gold Science and Applications, 1st ed.: CRC Press, 2010.

[44] S. S. Alias and A. A. Mohamad, Synthesis of Zinc Oxide by Sol-Gel Method for Photoelectrochemical Cells: Springer, 2014.

[45] http://www.jeol.co.jp/en/science/.

[46] M. Bouroushian and T. Kosanovic, Crystal Structure Theory and Applications, 2012, vol. 1, pp. 35-39.

[47] H. Han, N. D. Theodore, and T. L. Alford, Journal of Applied Physics, 2008, vol. 103, p. 013708.

[48] D. Kim, S. Jeong, and J. Moon, Nanotechnology, 2006, vol. 17, p. 4019.

[49] H. S. Barud, C. Barrios, T. Regiani, R. F. C. Marques, M. Verelst, J. Dexpert-Ghys, Y. Messaddeq, and S. J. L. Ribeiro, Materials Science and Engineering C, 2008, vol. 28, pp. 515-518.

[50] N. E. Kotel'nikova, V. N. Demidov, G. Wegener, and E. Windeisen, Russion Journal of General Chemistry, 2003, vol. 73, pp. 427-433.

[51] W. K. Son, J. H. Youk, and W. H. Park, Carbonhydrate Polymers 2006, vol. 65, pp. 430-434.

[52] J. He, T. Kunitake, and A. Nakao, Chemistry of Materials, 2003, vol. 15, pp. 4401-4406.

[53] J. F. Watts and J. Wolstenholme, An Introduction to Surface Analysis by XPS and AES: Wiley, 2003.

[54] T. Mates, P. C. P. Bronsveld, A. Fejfar, B. Rezek, J. Kocka, J. K. Rath, and R. E. I. Schropp, Journal of Non-crystalline Solids, 2006, vol. 352, pp. 1011-1015.

[55] www.gwyddion.net.

[56] N. Wolf, M. Rydzek, D. Gerstenlauer, M. Arduini-Schuster, and J. Manara, Thin Solid Films, 2013, vol. 532, p. 60.

[57] T.-B. Hur, Y.-H. Hwang, and H.-K. Kim, Journal of Applied Physics, 2004, vol. 96,

[58] P.-S. Huang, D. H. Kim, and J.-K. Lee, Applied Physics Letters, 2014, vol. 104, p. 142102.

[59] T. M. Barnes, M. O. Reese, J. D. Bergeson, B. A. Larsen, J. L. Blackburn, M. C. Beard, J. Bult, and J. v. d. Lagemaat, Advanced Energy Materials, 2012, vol. 2, pp. 353-360.

[60] H. Wu, D. Kong, Z. Ruan, P.-C. Hsu, S. Wang, Z. Yu, T. J. Carney, L. Hu, S. Fan, and Y. Cui, Nature Nanotechnology, 2013, vol. 8, p. 421.

[61] J.-Y. Lee, S. T. Connor, Y. Cui, and P. Peumans, Nano letters, 2008, vol. 8, p. 689.

[62] D. Zhang, R. Wang, M. Wen, D. Weng, X. Cui, J. Sun, H. Li, and Y. Lu, Journal of the American Chemical Society, 2012, vol. 134, pp. 14283-14286.

[63] A. Kim, Y. Won, K. Woo, C.-H. Kim, and J. Moon, ACS Nano, 2013, vol. 7, pp. 1081-1091.

[64] A. Kim, Y. Won, K. Woo, S. Jeong, and J. Moon, Advanced Functional Materials, 2014, vol. 24, p. 2462.

[65] C.-W. Nan, Y. Shen, and J. Ma, Annual Review of Materials Research, 2010, pp. 131-150.

[66] A. B. V. K. Kumar, C. W. Bae, L. Piao, and S.-H. Kim, Material Research Bulletin, 2013, vol. 48, pp. 2944-2949.

[67] G. A. Gelves, B. Lin, U. Sundararaj, and J. A. Haber, Advanced Functional Materials, 2006, vol. 16, p. 2423.

[68] C. F. Guo and Z. Ren, Materials Today, 2015, vol. 18, p. 143.

[69] H. Mao, J. Feng, X. Ma, C. Wu, and X. Zhao, Journal of Nanoparticle Research, 2012, vol. 14, p. 887.

[70] M. Park, J. Im, M. Shin, Y. Min, J. Park, H. Cho, S. Park, M.-B. Shim, S. Jeon, D.-Y. Chung, J. Bae, J. Park, U. Jeong, and K. Kim, Nautre Nanotechnology, 2012, vol. 7, pp. 803-809.

[71] I. Kim, Y. Kim, K. Woo, E.-H. Ryu, K.-Y. Yon, G. Cao, and J. Moon, RSC Advances, 2013, vol. 3, p. 15169.

[72] P.-C. Hsu, H. Wu, T. J. Carney, M. T. Mcdowell, Y. Yang, E. C. Garnett, M. Li, L. Hu, and Y. Cui, ACS Nano, 2012, vol. 6, p. 5150.

[73] M. Tsuji, S. Hikino, R. Tanable, M. Matsunaga, and Y. Sano, CrystEngComm, 2010, vol. 12, pp. 3900-3908.

[74] M. Grouchko, A. Kamyshny, and S. Magdassi, Journal of Materials Chemistry, 2009, vol. 19, p. 3057.

[75] D. Deng, Y. Jin, Y. Cheng, and T. Qi, Applied Materials & Interfaces, 2013, vol. 5, p. 3839.

[76] N. Toshima and T. Yonezawa, New Journal of Chemistry, 1998, vol. 22, p. 1179.

[77] J.-J. Zhu, C.-X. Kan, J.-G. Wan, M. Han, and G.-H. Wang, Journal of Nanomaterials, 2011, vol. 2011, p. 982547.

[78] T. Yamauchi, Y. Tsukahara, T. Sakata, H. Mori, T. Yanagida, T. Kawai, and Y. Wada, Nanoscale, 2010, vol. 2, pp. 515-523.

[79] E. A. Anumol, P. Kundu, P. A. Deshpande, G. Madras, and N. Ravishankar, ACS Nano, 2011, vol. 5, p. 8049.

[80] C. D. Wagner, W. M. Riggs, L. E. Davis, J. F. Moulder, and G. E. Muilenberg, X-ray Photoelectron Spectroscopy: Perkin-Elmer Corp, 1979.

[81] T. M. D. Dang, T. T. T. Le, E. Fribourg-Blanc, and M. C. Dang, Advances in Natural Sciences: Nanoscale and Nanotechnology, 2011, vol. 2, p. 025004.

[82] J. C. Scaiano, K. G. Stamplecoskie, and G. L. Hallett-Tapley, Chemistry Communication, 2012, vol. 48, pp. 4798-4808.

[83] H. She, Y. Chen, X. Chen, K. Zhang, Z. Wang, and D.-L. Peng, Journal of Materials Chemistry, 2012, vol. 22, p. 2757.

[84] H. Guo, Y. Chen, H. Ping, J. Jin, and D.-L. Peng, Nanoscale, 2013, vol. 5, p. 2394.

[85] H. Guo, Y. Chen, X. Chen, R. Wen, Guang-Hui, and D.-L. Peng, Nanotechnology, 2011, vol. 22, p. 195604.

[86] H.-J. Yang, S.-Y. He, and H.-Y. Tuan, Langmuir, 2013, vol. 30, pp. 602-610.

[87] A. R. Rathmell, M. Nguyen, M. Chi, and B. J. Wiley, Nano letters, 2012, vol. 12, pp. 3193-3199.

[88] Y. Ahn, Y. Jeong, D. Lee, and Y. Lee, ACS Nano, 2015, vol. 9, pp. 3125-3133.

[89] M.-G. Kim, J. W. Hennek, H. S. Kim, M. G. Kanatzidis, A. Facchetti, and T. J. Marks, Journal of American Chemical Society, 2012, vol. 134, p. 11583.